

Spectroscopic Perspectives on
Ultrafast Coupling Phenomena
in Perovskite Oxides

DISSERTATION

Zur Erlangung des akademischen Grades

„Doctor rerum naturalium“

(Dr. rer. nat.)

in der Wissenschaftsdisziplin Experimentalphysik

eingereicht an der

Mathematisch-Naturwissenschaftlichen Fakultät

der Universität Potsdam

von

Lena Maerten

geboren am 06.07.1982 in Bremen

Gutachter Prof. Dr. Matias Bargheer
Prof. Dr. Ulrike Woggon
Prof. Dr. Thomas Dekorsy

eingereicht am: 6. Januar 2015

Tag der mündlichen Prüfung: 30. April 2015

Published online at the
Institutional Repository of the University of Potsdam:
URN urn:nbn:de:kobv:517-opus4-77623
<http://nbn-resolving.de/urn:nbn:de:kobv:517-opus4-77623>

*Basic research is like shooting an arrow into the air and,
where it lands, painting a target.*

H. B. Adkins

Abstract

In this thesis, I study ultrafast dynamics in perovskite oxides using time resolved broadband spectroscopy. I focus on the observation of coherent phonon propagation by time resolved Brillouin scattering: following the excitation of metal transducer films with a femtosecond infrared pump pulse, coherent phonon dynamics in the GHz frequency range are triggered. Their propagation is monitored using a delayed white light probe pulse. The technique is illustrated on various thin films and multilayered samples.

I apply the technique to investigate the linear and nonlinear acoustic response in bulk SrTiO_3 , which displays a ferroelastic phase transition from a cubic to a tetragonal structural phase at $T_a = 105$ K. In the linear regime, I observe a coupling of the observed acoustic phonon mode to the softening optic modes describing the phase transition. In the nonlinear regime, I find a giant slowing down of the sound velocity in the low temperature phase that is only observable for a strain amplitude exceeding the tetragonality of the material. It is attributed to a coupling of the high frequency phonons to ferroelastic domain walls in the material. I propose a new mechanism for the coupling of strain waves to the domain walls that is only effective for high amplitude strain.

A detailed study of the phonon attenuation across a wide temperature range shows that the phonon attenuation at low temperatures is influenced by the domain configuration, which is determined by interface strain. Preliminary measurements on magnetic-ferroelectric multilayers reveal that the excitation fluence needs to be carefully controlled when dynamics at phase transitions are studied.

Kurzdarstellung

In dieser Doktorarbeit untersuche ich ultraschnelle Dynamik in perovskitischen Oxiden mittels zeitaufgelöster optischer Spektroskopie. Der Schwerpunkt liegt dabei auf Phononendynamik, die mithilfe von zeitaufgelöster Brillouin-Streuung sichtbar gemacht wird: durch die Anregung einer metallischen Transducer-Schicht mit einem ultrakurzen Anregepuls wird eine kohärente Phononendynamik im GHz Frequenzbereich erzeugt. Die Ausbreitung der Schallpulse wird mit einem Weißlicht-Abfragepuls aufgezeichnet. Diese Methode wird am Beispiel verschiedener Dünnschicht- und Übergitterproben illustriert.

Die Methode und das gewonnene Verständnis wende ich an, um lineare und nichtlineare akustische Eigenschaften an einem SrTiO_3 -Kristall zu untersuchen. Dieser weist einen ferroelastischen Phasenübergang von kubischer zu tetragonaler Kristallstruktur bei $T_a = 105$ K auf. Im linearen Regime beobachte ich eine Kopplung der untersuchten akustischen Mode an eine weichwerdende optische Mode, welche den Phasenübergang charakterisiert. Im nichtlinearen Regime tritt eine gigantische Verlangsamung der Schallgeschwindigkeit unterhalb von T_a auf, wenn die induzierte Gitterverzerrung die Tetragonalität des Materials übersteigt. Dies kann auf eine Kopplung der hochfrequenten akustischen Mode an ferroelastische Domänenwände bei tiefen Temperaturen zurückgeführt werden. Ich entwickle einen neuen Mechanismus, der die Kopplung der Verzerrungswelle an die Domänenwände beschreibt.

Eine detaillierte Untersuchung der Phononendämpfung in SrTiO_3 über einen weiten Temperaturbereich zeigt, dass diese bei tiefen Temperaturen durch die Domänenkonfiguration beeinflusst ist. Die Domänenkonfiguration ist durch Verzerrungen an der Kristall-Transducer Grenzfläche bestimmt. Erste Untersuchungen an magnetisch-ferroelektrischen Übergittern zeigen, dass die Anregungsfluenz vorsichtig eingestellt werden muss, um die Dynamik an Phasenübergängen zu untersuchen.

Contents

1	Introduction	1
2	Background	5
2.1	Perovskite Oxides	5
2.2	SrTiO ₃	6
2.2.1	Ferroelastic Phase Transition	7
2.2.2	Formation of Domains in SrTiO ₃	8
2.2.3	Elastic Properties at the Transition	9
2.2.4	Effect of Doping - (Sr,Ba)TiO ₃	11
2.3	Observing Phonons	11
2.3.1	Light Scattering from Phonons	11
2.3.2	Time Resolved Light Scattering from Phonons	13
2.3.3	Generation of Coherent Phonons	15
2.3.4	Lattice Dynamics in a Linear Chain Model	19
2.3.5	Anharmonic Effects	20
2.3.6	Attenuation of Coherent Phonons	21
2.4	Thin Film and Multilayered Structures	24
2.4.1	Phonons in Multilayers	24
3	Experimental Concepts	27
3.1	Time Resolved Pump Probe Spectroscopy	27
3.1.1	Measurement Setup	27
3.1.2	Broadband Detection	29
3.1.3	Typical Measurements: Transient Reflectivity Changes	31
3.1.4	Wavelength Dependent Aspects	31
3.1.5	Implications of Detection Scheme – Resolution and Apparent Damp- ing of Coherent Phonons	32

3.1.6	Normalisation of Coherent Phonon Amplitude	34
3.2	High Fluence Excitation	34
3.2.1	Effects of Anharmonicity	34
3.2.2	Fluence Dependent Excitation of Coherent Phonons	35
4	Observation of Phonon Dynamics in Thin Film and Multilayered Samples	39
4.1	Reflectivity Transients	39
4.2	Calculated Dispersion Relations	41
4.3	Measured Dispersion Relations	42
4.4	Eigenmodes of the Superlattice	44
4.5	Temporal Evolution of the Spectrum	45
5	Coupling of Acoustic Phonons to Domain Walls in SrTiO₃	49
5.1	Temperature Dependence of the Sound Velocity	49
5.2	Nonlinear Effects I: Anharmonicity	51
5.3	Nonlinear Effects II: Coupling to Domain Walls	52
5.3.1	Suppression of Domain Formation	54
5.3.2	Fluence Dependence of the Coupling	57
5.3.3	Microscopic Picture of Ultrafast Strain Induced Domain Wall Motion	57
6	Attenuation of Phonons in SrTiO₃	61
6.1	Observed Damping by Time Resolved Brillouin Scattering	61
6.1.1	Single Pulse Excitation	61
6.1.2	Excitation with a Train of Pump Pulses	62
6.1.3	Results from the Literature	63
6.2	Frequency Resolved Brillouin Scattering	64
6.3	Interpretation of Measured Damping Rates	65
6.3.1	Damping at Room Temperature	67
6.3.2	Damping at the Phase Transition	68
6.3.3	Damping at Low Temperatures	71

7	Dynamics in Magnetic Multilayers	75
7.1	Fluence Dependent Demagnetisation in Manganites	75
7.1.1	Introduction to Manganites	76
7.1.2	Time Resolved Reflectivity Changes	78
7.1.3	Temperature Dependent Signatures in the Measurements	79
7.1.4	Estimated Changes of the Magnetisation	80
7.2	Slow Reflectivity Oscillations in Magnetic Multilayers	83
7.2.1	Spectroscopic Evidence for Ferromagnetic Phase in (La,Sr)MnO ₃ - (Ba,Sr)TiO ₃ Multilayer	83
7.2.2	Slow Reflectivity Oscillations Observed in Magnetic Multilayers	84
7.3	Temperature Dependent Sound Velocity of a Ferroic Heterostructure	86
7.3.1	Temperature dependent sound velocity	86
7.3.2	Time Resolved X-ray Diffraction Data	89
7.3.3	Comparison of Results	89
7.3.4	Interpretation of Results – Phase Transition in (Ba,Sr)TiO ₃	90
8	Summary and Outlook	93
	Bibliography	95
	List of Symbols	111
A	Appendix: Normalisation of Measured Phonon Amplitude	113
A.1	Wavevector Dependence and Proportionality between detected oscillation amplitude and strain	113
A.2	Time Dependence of the Phonon Amplitude	114
	List of Publications	115

1. Introduction

Atoms lose some of their individual characteristics when they merge into a solid. Their electronic, optic and magnetic properties combine into those of a collective system and features specific to solids arise like elasticity, electronic conduction and magnetism. Localised excitations rapidly delocalise and new wavelike excitations arise: lattice vibrations, electron plasma oscillations, magnetic spin waves etc. The study of the interaction of these elementary excitations in a solid is a wide and complex research field. An understanding of the fundamental interactions is key for the development of new functional electronic devices. The design and improvement of everyday equipment like laptops, DVD players and mobile phones crucially depends on the fundamental understanding of electron and light interactions in semiconductors. Advances in the understanding of lattice vibrations has lead to valuable technologies like ultrasound sonography, sound navigation and the improvement of thermally insulating materials. Applications like thermoelectric devices are developing fast [Mal13]. Further promising building blocks for the development of novel nanoelectronic devices are multiferroic materials displaying a strong coupling of the collective electronic, lattice and magnetic degrees of freedom. The ferroic phases display a long range order and are usually composed of domains, which display different orientations of the ferroic property. While the occurrence of domains is often suppressed and the domain walls between them are considered as defects, they may also be exploited [Par08] for functional devices. An understanding of the domain properties and their coupling to the degrees of freedom in a solid is crucial for fully exploiting the functionalities of multiferroic materials.

Important for the understanding of the fundamental interaction processes is the investigation of their dynamics. For this, a versatile technique with high time resolution is required and femtosecond pump probe spectroscopy is suitable. A particular subsystem of the solid is excited with an optical pump pulse triggering specific dynamics that are determined by the degrees of freedom present in the system, their interaction mechanisms and coupling time scales. In the probing process, the dynamics induced by the excitation pulse are monitored by a delayed probe pulse sensitive to particular properties of the solid. Very refined techniques have been developed, which are sensitive to specific properties of the solid: time resolved hard x-ray diffraction yields information about the movement of the atoms; time resolved photoemission spectroscopy gives insight into the temporal evolution of the band structure; Kerr spectroscopy is sensitive to the sample magnetisation. Spectroscopy in the visible range yields information about them all. This is a great advantage and a drawback of the technique: information about the electronic system, light scattering from coherent and incoherent phonons and scattering from magnons are obtained all at once and need to be carefully disentangled.

In this thesis, I observe ultrafast dynamics in different perovskite oxides using time resolved broadband reflectivity measurements in the visible spectral range. By

means of an ultrashort infrared light pulse, heat is deposited in the electronic system of metal layers and is rapidly transferred into the lattice. This leads to the fast buildup of stress and the generation of strain pulses, i.e. coherent phonon wavepackets. In the observation process, light is used as a tool to study the propagation of these coherently excited phonons by time resolved Brillouin scattering experiments. A white light continuum allows observing a broad spectrum of phonon modes simultaneously. In the measurements presented here, phonons in the hypersound frequency range of 50 - 80 GHz are investigated. Performing measurements on various thin film and multilayered samples, propagating and standing phonon wavepackets are excited and monitored using broadband detection.

In particular, phonon dynamics in the material SrTiO₃ are studied across a wide temperature range. The material displays a structural, so-called antiferrodistortive phase transition at the transition temperature $T_a = 105$ K. This is accompanied by the softening of an optic phonon mode, which induces a softening of the acoustic branch and leads to anomalies in the acoustic behaviour at the phase transition. Tuning the amplitude of excitation and thus the amplitude of the generated hypersound pulse, linear and nonlinear effects in the elastic response of the material are monitored. The amplitude dependent propagation velocity of the phonons yields information about the coupling of strain to a further excitation: a coupling of the high amplitude strain pulses to domain walls in the antiferrodistortive phase of SrTiO₃ is found. Furthermore, the attenuation of the coherent phonon modes is studied. The observed temperature dependent attenuation rate allows us to draw conclusions about dominant scattering processes in different temperature regimes. First measurements on ferroic multilayers are presented, paving the way for further research on this topic.

The thesis is organised as follows: in chapter 2, I give an introduction to the material class of perovskites with a particular focus on the material SrTiO₃ and its structural phase transition at $T_a = 105$ K. The principle of phonon light scattering is introduced and I explain, how coherent phonon wavepackets are excited and their propagation is modelled. In chapter 3, I introduce the basic concepts of the experimental method and explain the experimental setup. Specific aspects regarding the excitation and propagation of high amplitude wavepackets are discussed in this chapter. In chapter 4, I illustrate time resolved phonon light scattering by applying the concepts to a thin film and multilayered samples. Oscillating features in the transient reflectivity signal are presented and their physical origin is explained. Limitations of the optical technique and the temporal and spectral resolution are discussed. Chapters 5 and 6 focus on experiments related to the structural phase transition in SrTiO₃ at $T_a = 105$ K: in chapter 5, I display measurements of the sound velocity in SrTiO₃ as a function of temperature. In the linear coupling regime, I find an anomaly of the acoustic properties at the phase transition in agreement with the literature. For the nonlinear coupling, observed only for very high amplitude strain pulses, a giant softening appears that can be explained by the coupling of strain to domain walls. A microscopic model for this strain induced domain wall motion is proposed. In chapter 6, I focus on the attenuation of ultrasound phonons in the

vicinity of the phase transition. I discuss the damping of acoustic phonons above and below the phase transition of SrTiO_3 for various samples with different epitaxial strain conditions at the interface between transducer film and SrTiO_3 . Finally, in chapter 7, I show measurements on perovskite heterostructures composed of a magnetic and a ferroelectric material. I study, how the demagnetisation dynamics depend on the excitation fluence. Evidence for a magneto-acoustic coupling in the multilayers is found. The temperature dependence of the elastic properties suggests the occurrence of a phase transition in one of the ferroic heterostructures. The results are summarised in chapter 8 and an outline for future research on the basis of my findings is given.

2. Background

2.1 Perovskite Oxides

In this thesis we study the dynamics in oxides that crystallise in the perovskite structure. This crystal structure has the chemical composition ABO_3 and is illustrated in the left panel of figure 2.1. The sites A are occupied by cations of the rare earth or alkaline earth group and the B sites by transition metals [Dag08]. The fact that many different ions can be incorporated on sites A and B is reflected by the large variability of the tolerance factor introduced by Goldschmidt [Gol26], t_G with

$$t_G = \frac{r_A + r_O}{\sqrt{(r_A + r_B)}} , \quad (2.1)$$

where r_A , r_B , and r_O are the radii of the ions A , B and O . This factor is a measure of how much the structure differs from the ideal, cubic perovskite with $t_G=1$. The perovskite structure is found to be stable for a large range of t_G in the interval $0.78 < t_G \leq 1.05$ [Ran11]. The physics of most perovskite oxides is dominated by the overlap of the transition metal $3d$ -orbitals, and the oxygen $2p$ -orbitals. A small change of the orbitals may result in a transition from an insulating state to a metallic or even superconducting phase, may switch a paramagnet to a ferromagnet or antiferromagnet, or lead to a ferroelectric ground state at low temperatures. The various ferroic and structural phases differ in their degrees of freedom, which show a complex coupling behavior, as illustrated in the right panel of figure 2.1. Using different compositions or doping levels, many functional properties can be designed [Dag08] and incorporated in nanoelectronic devices. These materials can often be grown epitaxially and the flexibility of the perovskite structure allows the layering

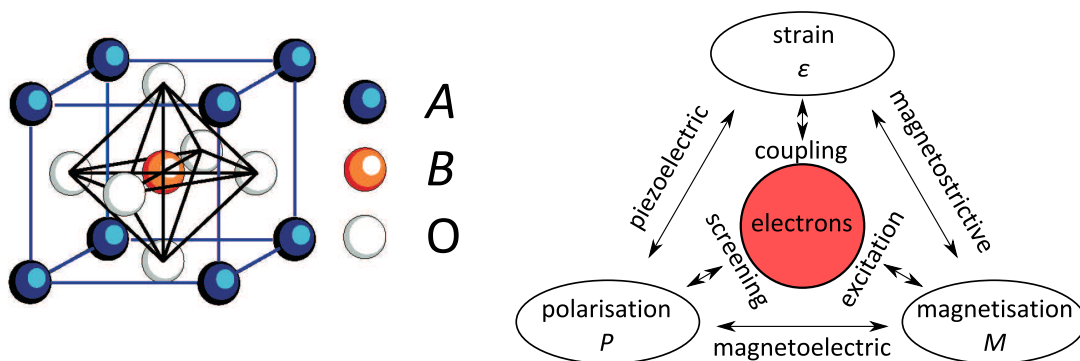


Figure 2.1: Left: Structure of a perovskite composed of atoms A, B and O (extracted from [Kle02]). Atom B is located at the centre of the cubic unit cell and is surrounded by an oxygen octahedron. Right: Illustration of the different degrees of freedom in a solid and their couplings.

Table 2.1: Collection of the most relevant ferroic and structural features of the samples employed in this thesis. FM: ferromagnet, T_a : ferroelastic phase transition temperature, T_C : Curie temperature for ferroelectric and ferromagnetic phase transitions.

material	features
SrTiO ₃	quantum paraelectric, structural transition, $T_a = 105$ K [Lyt64]
(La _{0.7} Sr _{0.3})MnO ₃	FM, $T_C = 370$ K, metal [Dag01]
SrRuO ₃	FM, $T_C = 160$ K, structural transition, magnetostriction [Kiy96]
(Ba _{0.7} Sr _{0.3})TiO ₃	ferroelectric, $T_C \approx 300$ K, structural phase transitions [Lem96]
Pb(Zr _{0.2} Ti _{0.8})O ₃	ferroelectric, $T_C = 750$ K [Izy07]

of different materials. Multilayers are grown to couple the degrees of freedom of one layer to properties of the other [Sch08]. The epitaxial strain, which originates from the lattice mismatch of the materials, is another tunable parameter [Cao11]. It influences the ferroic properties of the layers and thus alters their functionalities.

In this thesis, we discuss time resolved optical reflectivity measurements on thin films and multilayers composed of the materials SrTiO₃ (STO), La_{0.7}Sr_{0.3}MnO₃ (LSMO), Ba_{0.7}Sr_{0.3}TiO₃ (BST), SrRuO₃ (SRO) and Pb(Zr_{0.2}Ti_{0.8})O₃ (PZT). We particularly focus on the compound STO, which will be introduced in more detail in the next section. A summary of the most relevant properties of the selected samples is given in Table 2.1.

2.2 SrTiO₃

SrTiO₃ is a dielectric perovskite, which shows cubic structure at room temperature and a transition into a tetragonal phase at $T_a = 105$ K. It is widely used as a substrate material for the growth of perovskite thin films to create novel nanoelectronic phenomena and applications. It shows various structural phase transitions [Lyt64] and is considered a quantum paraelectric [Mül79]: the dielectric constant at high temperatures shows a Curie-Weiss behaviour with $T_C \approx 35$ K, however, approaching T_C the behaviour deviates from the Curie-Weiss law and the dielectric constant remains finite down to the lowest temperatures, because quantum fluctuations inhibit the ferroelectric phase transition. Koreeda *et al.* claim to have found the phenomenon of second sound, the wavelike propagation of heat, in STO [Kor07] and the existence of a new quantum state [Mül91] is highly debated. The various structural phase transitions and the domain pattern of STO have been subject to extensive research [Lyt64, Shi69, Chr98, Loe10, Car07, Sal11a, Sal11b, Sco12, Sal13b]. The elastic behaviour of STO has been studied since the 1960s [Bel63, Kai66, Nav69, Ber69] and has recently attracted attention due to the observation of a very high mobility of the domain walls in the tetragonal phase [Kit00, Sco12].

In this section, we focus on the structural phase transition at $T_a = 105$ K and discuss the influence of domain walls on the elastic properties of the material.

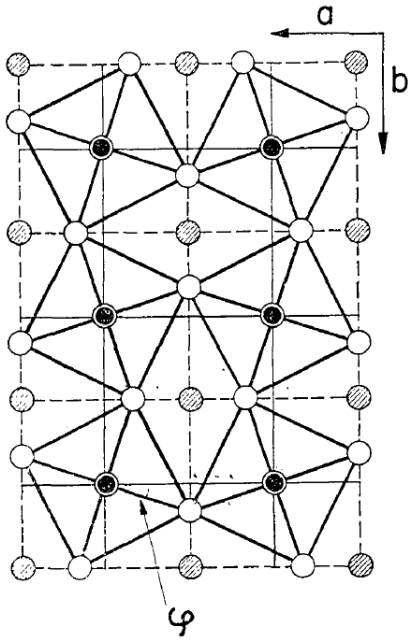


Figure 2.2: Twodimensional projection of the STO structure in the antiferrodistortive phase. The oxygen octahedra in adjacent unit cells rotate by the angle φ around the c -axis, perpendicular to the drawing plane [Uno67]. The octahedra in adjacent unit cells show an opposite sense of rotation, leading to a doubling of the unit cell.

2.2.1 Ferroelastic Phase Transition

At $T_a = 105$ K STO undergoes a structural phase transition from the cubic phase to a tetragonal low temperature phase [Lyt64, Shi69]. This phase is characterised by a rotation of the oxygen octahedra around one of the cubic axes that results in a slight relative tetragonal elongation along this axis, which is referred to as the c -axis. The octahedra in neighbouring unit cells rotate in opposite directions [Uno67] as shown in figure 2.2, which leads to a doubling of the unit cell. This phase is called antiferrodistortive, in analogy to ferromagnetic phase transitions: the c -axis displays a *distortion*, the rotation of the octahedra shows a long range order, hence the term '*ferro-*' appears, and the sense of the octahedra rotation is opposite in adjacent unit cells, justifying the prefix '*anti-*'.

The rotational motion of the oxygen octahedra is described by an optical phonon mode that slows down or, equivalently, softens towards the phase transition [Shi69, Koh06]. At the transition, the equilibrium angle of rotation becomes finite and increases with decreasing temperature. Consequently, the oxygen octahedra, which conserve their dimensions, occupy less space in the ab -plane and the structure experiences the above mentioned small tetragonal elongation along the c -axis to ensure a conservation of volume. Since the neighbouring unit cells display an opposite sense of rotation or, equivalently, an opposite phase, this mode is the mode of minimum wavelength and therefore maximum phonon wavevector at the edge of the Brillouin zone.¹ The rotational angle amounts to 2° [Uno67] at low temperatures and serves as the order parameter to describe the phase transition [Mül68, Pyt69]. The tetragonality is on the order of $c/a \approx 10^{-4}$ around 100 K [Lyt64, Kia96]. The phase transition is found to be predominantly of second order [Shi69, Slo70, Mül74, Car07].

¹This point in the Brillouin zone is called the R point [Koh06].

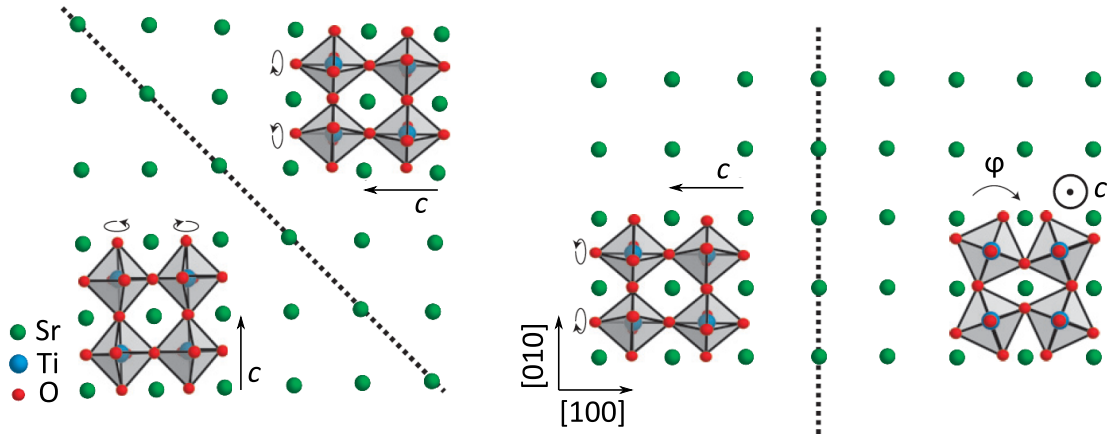


Figure 2.3: Illustration of the microscopic configuration at two different domain boundaries, taken from [Kal13].

2.2.2 Formation of Domains in SrTiO_3

Without structural constraints, external electric fields or pressure, there is no preferred orientation of the elongated c -axis in the antiferrodistortive phase of an STO crystal. The local orientation of the c -axis is determined by small defects and local strain fields and domains are formed with differently oriented c -axes. Parts of the crystal with different orientations of the c -axes are separated by domain walls. Figure 2.3 illustrates the microscopic configuration at two boundaries between differently oriented domains. Due to the slight elongation of the c -axis, a coupling between strain and domain orientation becomes evident: when uniaxial pressure is applied, the c -axis is preferentially oriented perpendicular to the direction of pressure and the formation of domains can be suppressed [Fos72, Kit00]. Since the orientation of the tetragonal axis sensitively depends on strain fields, the domain configuration is altered near the surface of the crystal [Sal11b] and is influenced by the presence of a surface layer and the hereby induced strain [Loe10]. Additionally, the transition temperature T_a shows a strong dependence on pressure: the tetragonal relaxation is facilitated by an externally applied uniaxial pressure and the transition temperature therefore increases significantly with externally applied pressure [Gue10].

In addition to these twin domains, a different sort of domains can be found: antiphase domains show equal c -axis but a disrupted sense of octahedra rotation at the domain boundary [Arz00]. These domains do not move under external pressure [Kit00] but give rise to an anomaly of the lattice parameter c below 40 K. A ferroelastic phase has been predicted within antiphase boundaries [Tag01]. In this thesis, the presence of antiphase domains in our samples will not be further discussed.

The presence of domains in STO gives rise to anomalies in the elastic and structural properties at the antiferrodistortive transition and has led to contradicting results in the literature [Car07]. When properties of STO below T_a are discussed, the presence of domains should always be considered.

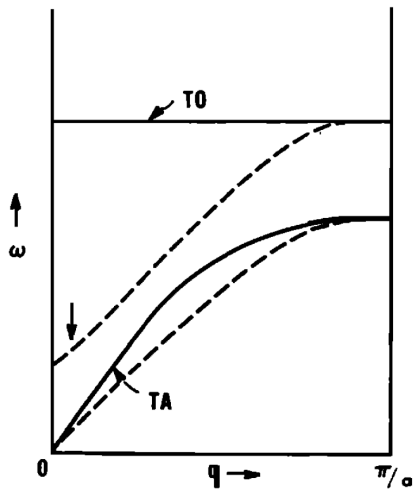


Figure 2.4: Illustration of the linear interaction between softening optic and acoustic phonon branches: the softening optical phonon pushes down on the acoustic branch. Taken from [Fle71].

2.2.3 Elastic Properties at the Transition

The coupling of acoustic phonons to the soft optic mode causes anomalies of the acoustic properties at the phase transition. Fleury [Fle71] differentiates between a linear interaction leading to a softening of the acoustic phonon branch, and higher order interactions that lead to phonon phonon scattering and, as a consequence, to an increased ultrasound attenuation at the phase transition.

The linear interaction can phenomenologically be visualised in the following way: the coupling of the optic and acoustic phonon branches leads to a mutual repulsion, which is a common phenomenon for coupled oscillators [Nov10]. The softening optic mode thus pushes down on the acoustic branch. This is illustrated for a zone centre transversal soft mode in figure 2.4.

A softening of this kind due to the coupling of the acoustic branch with an optical phonon that softens at the Brillouin zone edge has been experimentally verified for ultrasound phonons in the MHz range [Bel63, Kai66, Reh70a, Fos72] and has more recently also been measured for GHz, 'hypersound' phonons [Heh96, Yam02, Nag12]. Theoretical models for the description of this effect have been proposed based on a Landau free energy expansion [Slo70, Reh71, Fos72] or on a microscopic description using a model hamiltonian [Nav69, Pyt70].

In addition to the described phonon phonon coupling effects, a coupling of ultrasound phonons to domain walls has been observed [Fos72, Kit00, Sco12]. This coupling leads to an additional softening of the acoustic properties below the phase transition temperature, which can be understood in the following way: under transient compressive strain generated by the ultrasound pulse, a movement of a domain wall may lead to a transient enlargement of domains with the shorter axis along the direction of the strain, i.e. along the direction of sound propagation, and at the same time to a shrinking of domains with enlarged c -axis along this direction. Since the a -axis is smaller than the c -axis, the crystal thus contracts more than it would do without domain wall movement due to the reorientation of the c -axis in the effected unit cells. Therefore, the domain wall movement makes the crystal appear softer,

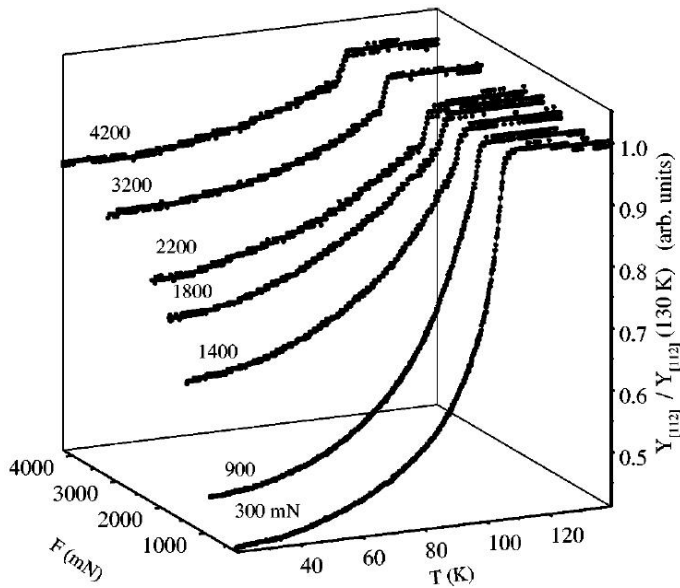


Figure 2.5: Temperature dependence of the relative Young's modulus for different external static stress parallel to the dynamic stress with frequency $f = 11$ Hz, taken from [Kit00]. Approaching the phase transition from above, a rapid drop followed by a gradual decrease of the relative Young's modulus is observed.

i.e. the sound velocity decreases. This effect has been termed superelastic behaviour in the literature [Kit00].

Figure 2.5 displays the temperature dependence of the Young's modulus for different externally applied stresses [Kit00], in which both softening effects, the coupling of the acoustic branch to the soft mode and the coupling to the domain walls are observable. The sound velocity is proportional to the square root of the corresponding elastic modulus. For longitudinal waves in an isotropic, cubic crystal it is given by $v = \sqrt{c_{11}/\rho}$ [Hun07], with the density of the material ρ and the respective element of the elastic stiffness tensor c_{11} that is in this case equivalent to Young's modulus. For the graph presented here, the temperature dependent modulus has been normalised to its value above the phase transition. Approaching the phase transition from above, there is a sudden decrease of the relative Young's modulus. This is best discernible for the highest static stress, given by the $F = 4200$ mN curve, since the formation of domains is largely suppressed here and the coupling to the soft mode dominates the behaviour. This step-like softening of the acoustic modes directly at the transition temperature T_a is superimposed by an even larger continuous softening below T_a , attributed to the coupling of phonons to domain walls between areas of differently oriented c -axes. In the figure, this gradual decrease of the modulus for decreasing temperatures can be best identified for the lowest static stress, the $F = 300$ mN curve. Reducing the formation of domains by external static stress, as discussed in section 2.2.2 above, gradually reduces this additional effect [Fos72, Kit00].

Carpenter has collected data that show a large variation of the elastic properties below T_a [Car07]. However, all data obtained by Brillouin scattering, i.e. experiments sensitive to GHz phonons, show only the small drop in sound velocity directly at T_a that is attributed to the coupling to the soft mode [Heh96, Yam02, Nag12]. In chapter 5 we will show that for very high amplitude strain waves, the coupling to domain walls is effective even in the GHz range.

The nonlinear interaction between the acoustic and optic branches leads to an increased dissipation at the phase transition: the ultrasound attenuation exhibits a singularity. This has been experimentally found for MHz phonons in the 1960s [Kai66, Nav69, Ber69, Reh70a, Fos72] and recently also for GHz [Nag12] phonons. Theoretical descriptions predict a criticality for the ultrasound attenuation α_{us} of the form $\alpha_{\text{us}} \propto 1/|T - T_a|^\eta$ at the phase transition, with a critical exponent η ranging from 1/3 to 3/2 [Nav69, Pyt70, Reh71].

2.2.4 Effect of Doping - (Sr,Ba)TiO₃

BaTiO₃ (BTO) is a material similar to STO, which does show a ferroelectric phase transition: below $T_C = 120$ °C [vHi50] the compound is ferroelectric and shows tetragonal crystal structure. The origin of the polarisation is the displacement of the central Ti cation within the unit cell. With increasing Sr content, the Curie temperature can be lowered [vHi50], which is desired for nanoelectric devices functioning at room temperature. Equivalently, the quantum paraelectric STO can be doped with Ba. A ferroelectric phase is found for a minimum Ba content of $x \approx 0.035$ [Lem96]. The Curie temperature increases with increasing Ba content. For our measurements we chose a Ba content of $x = 0.7$, leading to a Curie temperature of the compound of $T_C \approx 300$ K [Lem96]. In contrast to the widely used ferroelectric PZT, BST has no toxic constituents and is therefore much more attractive as building block in nanoelectronic devices.

2.3 Observing Phonons

Phonons are elementary vibrational excitations of the crystal lattice [Hun07]. One distinguishes acoustic and optical phonons. In acoustic modes, all atoms in one unit cell have the same phase, while in optic modes, the phase of each atom in one unit cell may be different. In the experiments presented here, we solely observe the propagation of coherently excited longitudinal acoustic phonons, but their behaviour is strongly influenced by the softening of an optic mode, as discussed in section 2.2.3 above. In this section, we introduce the mechanism of time domain Brillouin scattering and discuss further aspects that are relevant to our measurements, such as high fluence excitation, anharmonicity effects and the attenuation of phonons.

2.3.1 Light Scattering from Phonons

In our description of phonon light scattering processes, we treat phonons as quasi-particles with energy $\hbar\omega_q$ and momentum $\hbar q$. In the scattering process with light, phonons are either created or annihilated. When acoustic phonons are involved, the process is called Brillouin scattering. Figure 2.6 illustrates the momentum conservation for the creation of a phonon. The general equations of energy and momentum

conservation are

$$\omega' = \omega \pm \omega_q \quad (2.2)$$

$$\mathbf{k}' = \mathbf{k} \pm \mathbf{q} , \quad (2.3)$$

with frequencies ω and ω' and wavevectors k and k' of the incident and scattered photon and frequency ω_q and wavevector q of the scattering phonon. Here, $+$ denotes the annihilation and $-$ the creation of a phonon. Figure 2.6 illustrates this configuration for the creation of a phonon. Since the energy of phonons is generally

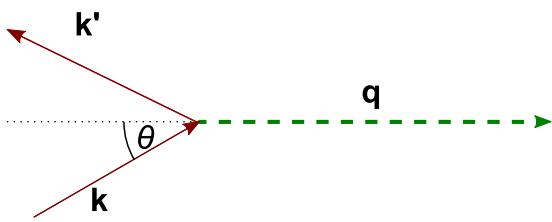


Figure 2.6: Momentum conservation for the creation of a phonon, where k and k' are photon wavevectors, q is the phonon wavevector and θ is the angle between incoming photon and phonon.

much smaller than the energy of optical light, the absolute value of the incident photon wavevector is approximately equal to the absolute value of the scattered photon wavevector: $k \approx k'$. The momentum component of the photons perpendicular to the phonon is unaltered. The parallel component $k \cos \theta$, where θ is the angle between incident photon and phonon, is changed by addition or subtraction of the energy and momentum of a phonon. Figure 2.7 illustrates energy and momentum conservation parallel to the scattering phonon: a photon with the very steep dispersion, indicated by the solid red line, scatters off a phonon with a dispersion as indicated by the dashed green lines. The shape of the phonon dispersion will be discussed in section 2.4 below. The phonon energy and momentum according to the phonon dispersion relation is added to the energy and momentum of the incoming photon. The relation between energy and momentum of the resulting, outgoing photon must again fulfill the dispersion relation of light. Therefore, for a given photon, there are principally two different solutions for the wavevector of the phonon involved, as indicated by the two intersection points in the figure, and thus two possible scattering regimes [Jus87]. In the first regime, the momentum of the scattering photon parallel to the travelling phonon is nearly unaltered, i.e. it is scattered in forward direction, and the transferred phonon momentum q is approximately zero:

$$q \approx 0 \quad (\text{forward scattering}) . \quad (2.4)$$

The signature of this scattering regime is its occurrence with approximately the same characteristic frequency for all photons independent of wavelength. The case $q \approx 0$ can be realised by acoustic phonons at the origin of the Brillouin zone, by backfolded acoustic modes, as will be discussed in section 2.4, or by optic modes. In the second regime, the momentum of the scattering photon parallel to the travelling phonon is

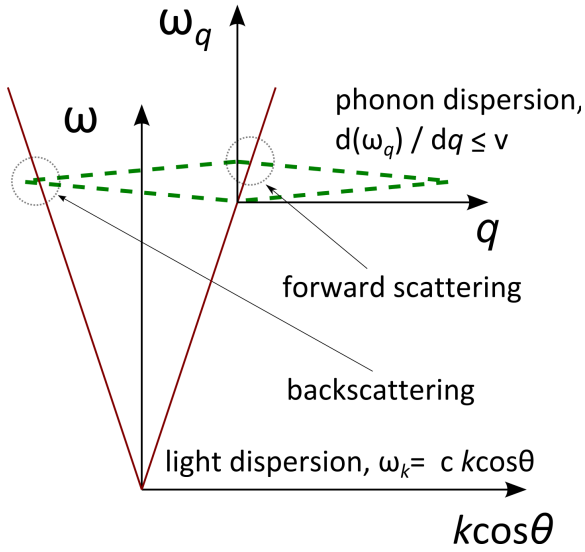


Figure 2.7: Illustration of energy and momentum conservation. A photon with given energy and momentum (solid red dispersion) can combine with a phonon (dashed green dispersion, the shape of the dispersion will be discussed later) to form a new photon with approximately the same energy and momentum (forward scattering condition) or reversed momentum (backscattering condition). The energies are not drawn to scale, the light dispersion is much steeper in reality.

reversed, i.e. it is scattered in backward direction. The wavevector of the scattering phonon is thus given by

$$q \approx 2k \cos \theta \quad (\text{backscattering}) , \quad (2.5)$$

where θ can in this case also be regarded as the internal angle of incidence of the incoming photon with respect to the surface normal. Figure 2.8 illustrates the momentum conservation for both scattering regimes as vector diagrams. The length of the photon wavevector is nearly unaltered, as depicted for each regime by the two red dashed circles with nearly equal radii. The momentum component perpendicular to the phonon remains unchanged, the component parallel to the phonon is either nearly unchanged or reversed.

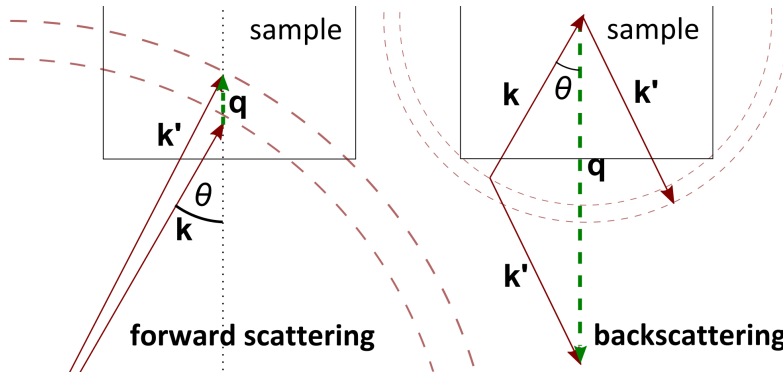


Figure 2.8: Illustration of momentum conservation and scattering geometry. The momenta are not drawn to scale: the changes in k and θ are much smaller in reality.

2.3.2 Time Resolved Light Scattering from Phonons

In the previous section, we focused on the momentum selection rules for phonon light scattering. According to equation 2.2, the energy of the scattering photon is altered by annihilation or creation of a phonon. The relative energy shift is on the

order of 10^{-4} for GHz acoustic phonons and can be resolved in the frequency domain. Spectrally narrow, continuous wave optical light is shone onto the sample and the energy shift of the detected scattered light is monitored.

We are using a different approach: we use spectrally broad, ultrashort light pulses and observe the oscillation frequency of the scattering phonon in a time resolved measurement. By means of an ultrashort light pulse, coherent acoustic phonon dynamics are triggered in the sample, which are afterwards monitored by a delayed probe pulse. Thereby, high amplitude phonon wavepackets can be generated and their propagation can be observed. The theoretical framework describing time resolved light scattering from coherently generated phonons has been developed by Thomsen and Grahn [Tho86]. The excitation mechanism will be discussed in section 2.3.3 below. For the experimental details of pump probe measurements we refer the reader to the next chapter.

Two effects modulate the light reflected from the sample with the frequency of the scattering phonons: firstly, the phonons present in the sample periodically modulate the optical properties of the different layers leading to a periodic modulation of the reflection from each interface. This is presumably the dominant effect in multilayered samples, where the optical properties are different for each individual layer.

Secondly, the light field that undergoes Brillouin scattering from a phonon interferes with a static² reference of the probe light reflected from the sample surface and interfaces. In this case, the relative phase of the interfering signals varies with the phase of the scattering phonon. Mathematically, the field amplitude of the static reference A_r and the time dependent field amplitude scattered off the phonons $A_p(t)e^{i\omega_q t}$ add up to yield the reflected intensity [Tho86]³

$$I(t) = |A_r + A_p(t)e^{i\omega_q t}|^2 = A_r^2 + 2A_r A_p(t) \cos(\omega_q t) + A_p(t)^2, \quad (2.6)$$

where only the second term shows a periodic time dependence. The weak reflection off the phonons is amplified by the strong reference signal. The phase of the oscillation is determined by the distance the lattice distortion has propagated into the sample and thus depends on the time delay of the pump and probe pulses [Tho86]. This latter effect allows the observation of phonons in the substrate, where there are no interfaces from which the reflection can periodically be modulated. Figure 2.9 illustrates the interference effect.

In forward scattering, the modulation frequency is simply given by the phonon frequency ν_q

$$\nu_q(q \approx 0), \quad (2.7)$$

where multiple frequencies as solutions for the equation are possible depending on the phonon dispersion relation. In the evaluation of the experiments, we mostly use the phonon frequency ν_q instead of its angular frequency ω_q , since this value is more easily conceivable. Both quantities are of course related via $\omega_q = 2\pi\nu_q$. For

²The reference signal may also display a time dependence. This will be discussed in section 3.1.6 and in appendix A.2.

³A more detailed derivation will be given in the appendix.

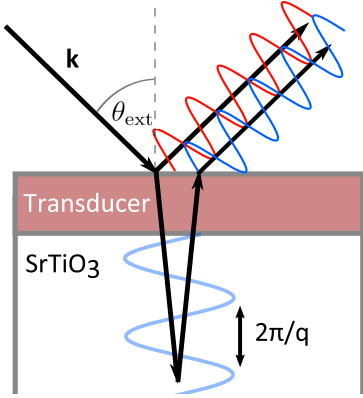


Figure 2.9: The light field scattering from the propagating strain interferes with the static reference from the sample surface yielding the oscillating signal in backscattering according to equation 2.8.

backscattering, equation 2.5 implies that the periodicity of constructive interference between reference light and scattered light is given by $\nu_q (q = 2k \cos \theta)$. For a linear phonon dispersion $2\pi\nu_q = v \cdot q$, with sound velocity v , follows from equation 2.5:

$$\nu_q (q = 2k \cos \theta) = \frac{v \cdot 2k \cos \theta}{2\pi} = \frac{2vn(\lambda) \cos \theta}{\lambda} \quad (2.8)$$

$$= \frac{2v \sqrt{n(\lambda)^2 - \sin^2 \theta_{\text{ext}}}}{\lambda} \quad (2.9)$$

with the vacuum probe wavelength λ and the refractive index $n(\lambda)$. In the second line we have introduced the experimentally adjustable external angle of incidence θ_{ext} using Snell's law.

In chapter 4 the concepts of forward and backscattering and the wavelength dependence of the phonon oscillation frequencies will be illustrated by time resolved reflectivity measurements on various multilayered samples.

2.3.3 Generation of Coherent Phonons

There is a vibrant debate in the community regarding the excitation mechanism of coherent phonons. Impulsive excitation via Raman scattering is claimed to be the dominant excitation technique [Bar99] in the low excitation regime. For high fluence excitation, the displacive excitation of coherent phonons [Zei92] is found to be dominant [Bar04]. In our case, the rapid thermal expansion of the materials immediately after optical excitation leads to the generation of coherent phonons [Boj12]: conduction electrons in the metal films absorb the optical pump light. The electrons rapidly thermalise [Che06] via electron electron scattering and the energy is subsequently coupled into the phonon system. This thermalisation process can be described by the so-called two temperature model [Ani74] and proceeds rapidly within about 200 femtoseconds in our materials [Kap99, Kor08, Boj12]. The subsequent thermal expansion governed by the Grüneisen parameter launches a strain pulse, which propagates through the sample and the substrate underneath. The generated strain profile determines the spectrum of modes that we excite. Below we discuss the concepts relevant for the excitation mechanism in our samples. Detailed modelling can be found in [Sch14b].

Electron Phonon Coupling – Two Temperature Model

In this model, the thermal equilibration of two heat baths is described by a set of differential equations, in this case:

$$C_e \frac{dT_e}{dt} = -G_{\text{el}}(T_e - T_l) + \Xi(t) \quad (2.10)$$

$$C_l \frac{dT_l}{dt} = G_{\text{el}}(T_e - T_l) \quad , \quad (2.11)$$

with the electronic and phononic heat capacities C_e and C_l , the electron-phonon coupling constant G_{el} and the induced energy density $\Xi(t)$. Heat transport out of the excited volume is neglected. If the temperature dependence of these thermodynamic quantities is neglected, the coupling time can be calculated, yielding [Ave02]

$$\tau_{\text{el}} = \frac{C_e C_l}{G_{\text{el}}(C_e + C_l)} \approx \frac{C_l}{G_{\text{el}}} \quad . \quad (2.12)$$

The approximation holds, when the heat capacity of the electrons is small compared to the heat capacity of the lattice, $C_e \ll C_l$. Since in our materials the electron phonon coupling is large [Kap99], the time constant for electron phonon coupling is on the order of a few hundred femtoseconds [Kor08]. The two temperature model can be utilised to describe the thermalisation of any two thermal subsystems. We will refer to this model in chapter 7, where the thermalisation between phonons and magnons is discussed.

Grüneisen Concept

Grüneisen developed a phenomenological model to describe the thermal expansion of solids. The model is based on the assumption that the relative change in phonon frequency linearly depends on the relative change in crystal volume

$$\frac{\delta\omega_{\mathbf{q},j}}{\omega_{\mathbf{q},j}} = -\gamma \frac{\delta V}{V} \quad , \quad (2.13)$$

where the Grüneisen parameter γ is independent of frequency, phonon wavevector and the phonon branch j . This is only a rough estimation, which can be improved by introducing individual Grüneisen parameters γ_j for each phonon branch. Using thermodynamic identities, the Grüneisen relation is calculated [Hun07]:

$$\alpha_{\text{th}} = \frac{\gamma C_V}{3B} \quad , \quad (2.14)$$

connecting the linear thermal expansion α_{th} of a crystal to its heat capacity per unit volume C_V and its bulk modulus B via the Grüneisen constant. This relation implies that the linear thermal expansion shows the same temperature dependence as the heat capacity. For the thermally induced expansion, we deduce

$\Delta V = V3\alpha_{\text{th}}\Delta T = 3\alpha_{\text{th}}E/C_V = \gamma E/B$, where E is the deposited energy in the system. The expansion is therefore mainly determined by the excitation energy, since B only weakly depends on temperature. In other words, in this model, the induced expansion ΔV is independent of the starting temperature. This is an important approximation for temperature dependent measurements, as discussed in chapters 5 to 7.

Excitation Profile

Following the induced temperature change, the heated material expands. In our samples, stress relaxation mainly occurs at interfaces. This is due to the fact that the probed area is usually small compared to the excited area such that in-plane relaxation is comparatively slow. At the interfaces, there is an asymmetry in stress between the layers. For the samples discussed in this thesis, absorbing metallic layers and transparent dielectric layers are alternately grown. Figure 2.10 illustrates the geometry of a typical multilayered sample. The metal layers will expand thereby

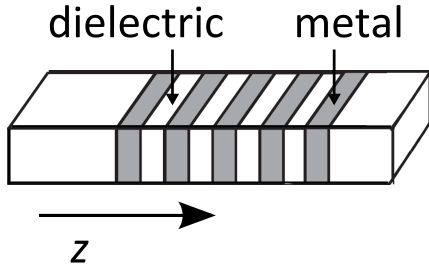


Figure 2.10: Typical structure of a multilayered sample. Absorbing metallic and transparent dielectric layers are alternately grown. The impulsively induced strain dynamics occurs in the growth direction of the layers, i.e. in the z -direction.

compressing the dielectric interlayers [Bar04, Her11]. At the interfaces, compressive strain fronts are launched, which propagate into the adjacent dielectric and further through the sample. Similarly, the inhomogeneous excitation of the layers leads to an inhomogeneous stress profile and thus to inhomogeneous strain within the layers. Reaching the surface, stress relaxation occurs and the compressive strain front is turned into an expansive strain front. At the interfaces of the perovskite layers, the reflection of the sound wave can be neglected due to the usually good acoustic impedance matching. When the strain front starting at the layer-substrate interface has travelled to the surface, has been reflected at the surface and travelled back through the sample into the substrate, the stress in the metal layers has relaxed. The metal layers have now expanded to a thickness given by their current temperature. After this time interval, given by $dt = 2d/v$, with sample thickness d and sound velocity v , there is no further coherent dynamics in the layers and the complete strain pulse has propagated into the substrate. Such a strain pulse can also be visualised as a phonon wavepacket. Figure 2.11 illustrates the shape of a strain pulse generated by a single metal transducer film [Boj12a, Sch14b]. In this simple picture, the finite penetration depth of the laser has been neglected. Depending of the shape of the transducer, its thickness, absorption length etc., a certain spectrum of phonons is excited. For the pulse displayed in figure 2.11 the spectrum is given by a $(\sin x/x)^2$ -function, with a maximum that is determined by the thickness d of

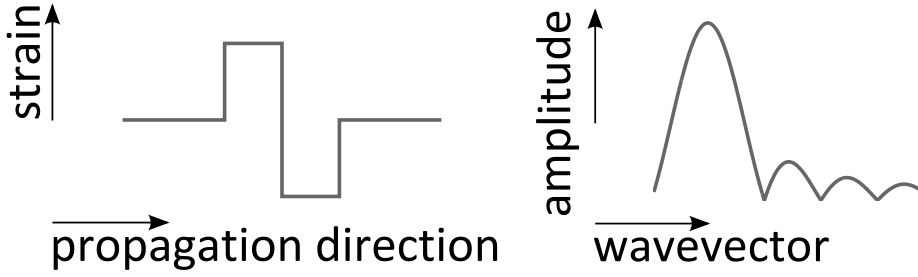


Figure 2.11: Left: Schematic of the strain profile generated by a single metal film (compare illustration in figure 2.9 for sample geometry). The finite penetration depth has been neglected. Right: Spectrum of a bipolar strain pulse as illustrated in the left panel

the layer, $q_{\max} = 0.74\pi/d$ [Boj13]. Long excitation pulses smooth out the excitation profile and suppress the generation of higher frequencies with $\nu > 1/\tau_{\text{pulse}}$ [Boj13].

Pulse Train Excitation

The spectrum of excited phonons is determined by the shape of the transducer film, as has been discussed above, and by the shape of the excitation pulse. When multiple metal layers with dielectric interlayers are excited, a train of strain pulses is produced, consisting of leading tensile and trailing compressive pulses. The resulting strain profile for a sample with 5 double layers is illustrated in figure 2.12.

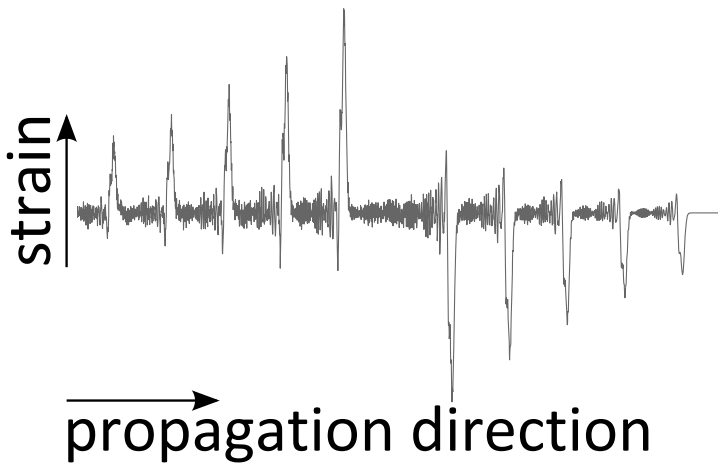


Figure 2.12: Strain profile generated by a superlattice consisting of five double layers (compare illustration of sample geometry in figure 2.10). The finite penetration depth has in this case been considered. Calculated in the linear chain model that will be introduced in the next section. See also Shayduk *et al.* [Sha13].

Multiple successive excitation pulses, on the other hand, result in a train of successive bipolar strain pulses. Multiple pulses with a periodic spacing lead to a narrowing of the excited spectrum. A constant pump pulse spacing of ΔT generates a strain wave with fundamental frequency $\nu = 1/\Delta T$ [Boj13]. Figure 2.13 displays a simulation for the excitation of a single transducer layer with one to eight subpicosecond excitation pulses. The integral pump fluence, i.e. the in total deposited energy is kept constant for all curves. Consequently, the modes that are generated in

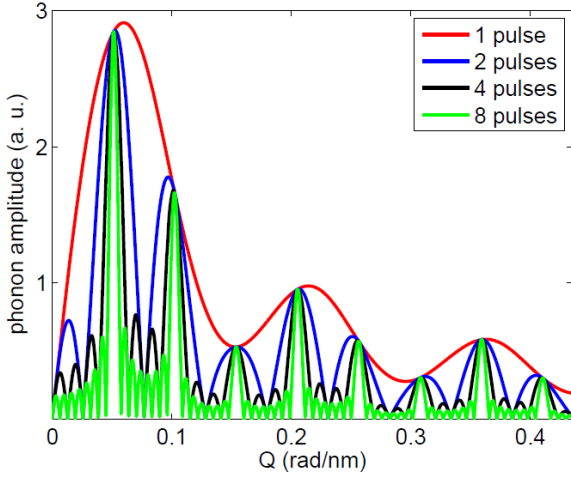


Figure 2.13: Simulated phonon amplitude for different phonon q -vectors after excitation by multiple successive subpicosecond pump pulses. The generated spectrum continually sharpens, as the number of pulses is increased. The deposited energy is kept constant for all simulated curves [Boj13].

phase with all 8 pulses interfere constructively and the phonon amplitude for these wavevectors sums up. Modes that are generated out of phase interfere destructively. Thus, the spectrum successively sharpens with the number of excitation pulses and a narrow excitation spectrum is formed.

2.3.4 Lattice Dynamics in a Linear Chain Model

Since the excitation spot is large compared to the propagation distance, the coherent dynamics in our time resolved experiments are generated mainly in the growth direction of the sample layers, the z -direction, compare illustration of sample geometry in figure 2.10. Therefore, the propagation can be modelled onedimensionally. We choose a discrete model [Bar04, Her11, Sch14a], in which the unit cells are represented by their masses m_i , which are connected by spring constants $k_i = m_i v_i^2 / c_i^2$. Here, k_i denotes the spring constant, v_i the sound velocity and c_i the lattice constant of the i th unit cell with $i = 1, 2, \dots, N$, and N being the total number of unit cells incorporated in the model. In this simple model, only longitudinal acoustic phonons are considered, optical phonons and transverse motion are neglected. The upper row of figure 2.14 gives an illustration of this model. The displacements are calculated by solving the system of N linear inhomogeneous differential equations

$$m_i \ddot{x}_i = -k_i(x_i - x_{i-1}) - k_{i+1}(x_i - x_{i+1}) + F_i(t) , \quad (2.15)$$

with the displacement of the i th mass $x_i(t) = z_i(t) - z_i^0$ and the additional force $F_i(t)$. The induced thermal stress is assumed to be instantaneous (compare discussion on electron phonon coupling above and fluence dependent study of the excitation in section 3.2.2 below) and remains constant after excitation, $\Delta(z, t) = \Delta(z)H(t)$ with the Heaviside step function $H(t)$. This force is visualised in the illustration by introducing spacer sticks between the unit cells of the absorbing layers and the springs at $t = 0$. Instantaneously, the springs are compressed and periodic dynamics are triggered. Stress relaxation occurs at the surface. In a finite sample, all coherent motion stops when the strain waves have reached the surfaces, leading eventually to

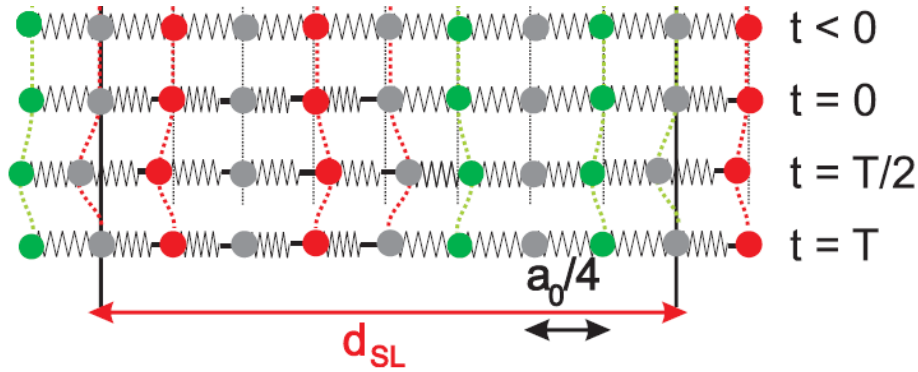


Figure 2.14: Illustration of the dynamics in a linear chain. At $t = 0$, spacer sticks, illustrated by short black horizontal lines, are introduced at the oscillator sites of the absorbing layer with length according to the excitation depth. The springs are instantaneously compressed. This triggers a periodic expansion and contraction of the layers [Bar04]. In this figure, T denotes the oscillation period of the superlattice, see section 2.4.1 on phonons in multilayers.

relaxed springs and an increased distance between the masses due to the induced heat. The induced heat is visualised by the spacer sticks in the figure, which remain when the stress has relaxed.

Solving the differential equations by diagonalisation of the force matrix [Her11], we obtain a solution in form of eigenvectors Ξ_i , which are the eigenmodes of the system, to the eigenvalues or eigenfrequencies ω_i . The time dependent displacements of each unit cell x_i , written as vector $\mathbf{X}(t)$, is given by the superposition of eigenmodes:

$$\mathbf{X}(t) = \sum_{j=1}^N \Xi_j \cdot A_j e^{i\omega_j t} . \quad (2.16)$$

This yields the lattice dynamics at all times.

The model can be extended to calculate the optical response. Specifying the complex index of refraction for each unit cell, the optical reflectivity can be calculated in a standard optical matrix formalism [Boj12].

2.3.5 Anharmonic Effects

In a linear model, where the coupling between the atoms is described by a harmonic potential, the imprinted strain profile does not change its shape since there is no coupling between the phonon modes. In order to account for phonon damping and other effects that involve phonon-phonon interaction such as phononic heat conduction and thermal expansion, higher order terms of the potential need to be considered. In our measurements we induce a very high strain level on the ‰ range in our samples, as will be discussed in chapter 5. Under such high strain conditions, the sound velocity and sound attenuation of the material are considerably affected.

Figure 2.15 depicts a purely harmonic interatomic potential, shown as dashed

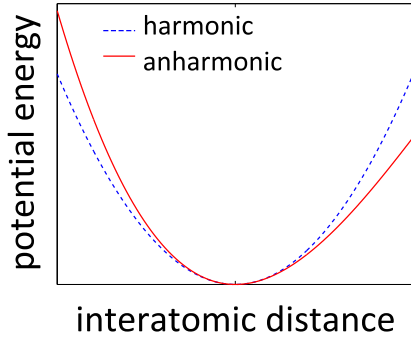


Figure 2.15: Illustration of a harmonic (dashed blue line) and an anharmonic (solid red line) interatomic potential.

blue curve, in comparison with a potential with a third order contribution, shown as solid red curve. One can immediately deduce that in the anharmonic case for a large oscillation amplitude the centre of mass is shifted towards positive displacements. In other words, for increasing temperatures, the atoms, which oscillate around their equilibrium displacement, are continually shifted towards larger displacements, i.e. the crystal expands. The sound velocity, which scales with the square root of the second derivative of the potential with respect to strain (compare equations of motion for a spring pendulum), is constant for a purely quadratic potential and linearly dependent on the displacement for a potential with third order contribution. This means that for a potential of the type depicted in figure 2.15, compressive waves propagate faster than tensile waves. For the wavepacket in figure 2.11 follows that the leading edge travels faster than the trailing edge. Additionally, due to the phonon phonon coupling, higher harmonics are generated, leading to a steepening of the pulse fronts [Mus02, Boj12a]. The anharmonicity can be incorporated in the linear chain model, which leads to a very good agreement between simulation and experiment [Boj12a]. Macroscopically, the anharmonicity reflects in the finite thermal expansion and the Grüneisen parameter of a solid.

2.3.6 Attenuation of Coherent Phonons

Definition of Terms and Conversion of Units

The attenuation of ultrasound α_{us} is defined as the reciprocal propagation length after which the amplitude of a propagating ultrasound oscillation has decayed to its $1/e$ value [Mar71]. The decay rate Γ is defined as $\Gamma = \alpha_{\text{us}}v$ with the sound velocity v of the corresponding phonon branch. The decay time τ of an ultrasound phonon oscillation is then given by $\tau = 1/\Gamma$. Quantities relating to the ultrasound attenuation are thus expressed per unit distance, per unit time or by their reciprocals in distance or time. In conventional ultrasound measurements, the attenuation of the sound intensity instead of the sound amplitude is measured, which is typically expressed in dB/cm. This can be converted according to $1 \text{ dB/cm} \hat{=} 20 \log_{10}(e) 1/\text{cm} = 8.68 1/\text{cm}$.

These properties of ultrasound phonons with certain wavevector q and frequency ν_q should not be confused with the average properties of phonons that contribute to the macroscopic thermal properties of the material. We refer to these 'average

thermal phonons' with overlined symbols to indicate the thermal average. The mean free path \bar{l} of thermal phonons is, in analogy to the kinetic theory of gases, related to the thermal conductivity κ of a solid according to

$$\kappa = C_V v_D \bar{l} / 3 = C_V v_D^2 \bar{\tau} / 3 , \quad (2.17)$$

with the heat capacity per unit volume C_V and the Debye velocity v_D that is introduced in the Debye model to calculate the phonon heat capacity and is given by $v_D^3 = 3(v_l^{-3} + 2v_t^{-3})^{-1}$ [Hun07], where v_l and v_t are the longitudinal and the transverse sound velocities of the solid. The mean free path is expressed as $\bar{l} = v_D \bar{\tau}$, with the average decay time of thermal phonons $\bar{\tau}$. In contrast to this average that gives no specific information about the phonon modes that contribute to thermal conduction, Brillouin scattering gives direct access to the frequency and attenuation rate of specific phonon modes with polarisation and wavevector chosen in the experiment.

In time domain Brillouin scattering, the time dependent amplitude and phase of the propagating phonons is observed via the interference of the light scattered from the phonons with a static reference signal, as explained in section 2.3.2 and as derived by Thomsen *et al.* [Tho86]. The temporal behaviour of the detected signal thus reflects the dynamics of the sound amplitude and is directly described by the properties defined above. When time domain signals are compared to signals obtained in the frequency domain, a correct conversion of units needs to be performed. Converting the time dependent amplitude from equation 2.6 into frequency domain by a Fourier transformation, we obtain the complex spectral amplitude

$$\begin{aligned} A(\omega) &= \frac{1}{\sqrt{2\pi}} \int_{-\infty}^{\infty} a_0 \Theta(t) e^{-t/\tau} \cos(\omega_q t) e^{-i\omega t} dt \\ &= \frac{a_0}{\sqrt{8\pi}} \left[\frac{1}{i(\omega - \omega_q) + 1/\tau} + \frac{1}{i(\omega + \omega_q) + 1/\tau} \right] \\ &\approx \frac{a_0}{\sqrt{8\pi}} \left[\frac{1}{i(\omega - \omega_q) + 1/\tau} \right] , \end{aligned} \quad (2.18)$$

where the approximation holds close to the resonance frequency. In frequency domain Brillouin scattering, however, the intensity of light scattered off the phonons is monitored. Similarly, in x-ray diffraction experiments the scattered intensity, which is proportional to the spectral phonon amplitude squared, is observed [Sha13]. The spectral intensity is given by

$$I(\omega) = |A(\omega)|^2 \propto \frac{1}{(\omega - \omega_q)^2 + (1/\tau)^2} , \quad (2.19)$$

with $1/\tau = \Delta\omega_{\text{HWHM}}$, the half width at half maximum of the thus obtained Lorentzian lineshape. When the intensity is measured as a function of frequency ν instead of angular frequency ω , a coordinate transform has to be performed and the half width at half maximum in the frequency domain corresponds to $\Delta\nu_{\text{HWHM}} = \Delta\omega_{\text{HWHM}}/2\pi = 1/2\pi\tau$ [Dem10].

There may be various processes that contribute to the ultrasound attenuation: scattering from thermal phonons, scattering from defects, surface or interface scattering or scattering from domain walls. When these processes are independent, the damping rates add up [Car61]:

$$\tau_{\text{tot}}^{-1} = \tau_{\text{ph}}^{-1} + \tau_{\text{D}}^{-1} + \tau_{\text{DW}}^{-1} + \dots, \quad (2.20)$$

with total decay time τ_{tot} , decay time due to phonon phonon scattering τ_{ph} , scattering from defects τ_{D} , scattering from domain walls τ_{DW} etc.

Interaction of Sound Waves with Thermal Phonons

There have been two different approaches to the modelling of ultrasonic attenuation due to phonon phonon scattering. Landau and Rumer developed a microscopic theory, in which the ultrasound phonons are regarded as a beam of low energy phonons scattering with a bath of thermal phonons [Lan37]. In the simplest calculation, only three phonon processes are considered. Selection rules have to be fulfilled that guarantee energy and momentum conservation. With decreasing decay time of thermal phonons, the energy and momentum uncertainties of the phonons increase. The energy uncertainty is connected with the average lifetime of the thermal phonons via the uncertainty relation $\Delta E \approx \hbar/\bar{\tau}$. When the energy uncertainty becomes comparable to the energy of the ultrasound phonon, it becomes difficult to apply the selection rules in the calculations. The theory is thus useful for $\hbar\omega_q \gg \hbar/\bar{\tau}$, yielding the condition $\omega_q\bar{\tau} \gg 1$, for the angular frequency ω_q of ultrasound phonons. The Landau Rumer approach thus proves useful for high ultrasound frequencies and low temperatures, where collisions are scarce.

In the other approach developed by Akhiezer [Akh39] and extended by Woodruff and Ehrenreich [Woo61], the sound wave is treated macroscopically: the strain arising from the sound waves acts as a driving force on the system of thermal phonons, leading to a nonthermal occupation of phonon modes. The system returns to equilibrium by subsequent collision processes. The damping rate according to the Akhiezer formalism for $\omega_q\bar{\tau} \ll 1$, where the average mean free path of the thermal phonons is small compared to the wavelength of the sound wave, can be expressed as [Woo61]

$$\Gamma = \frac{\gamma^2 C_V T \bar{\tau} \omega_q^2}{3\rho v^2} = \frac{3\alpha_{\text{th}}^2 B T \bar{\tau} \omega_q^2}{C_V}, \quad (2.21)$$

with Grüneisen parameter $\gamma = 3\alpha B/C_V$ as introduced in the discussion of coherent phonon generation in section 2.3.3 above, linear thermal expansion α_{th} , bulk modulus B , temperature T , mean thermal phonon decay time $\bar{\tau}$, density ρ , ultrasound phonon angular frequency ω_q and heat capacity per unit volume C_V . A counterintuitive implication of this relation is that in this phonon phonon scattering regime ultrasound phonons live longer, when the lifetime of thermal phonons is reduced, for example by defect scattering. This has been observed by several groups [Böm60, Kel67] and has also been studied in detail theoretically [Mar68].

In the intermediate regime, for $\omega\bar{\tau} \approx 1$, the Akhiezer formalism also yields a prediction for the ultrasound attenuation. The mechanism then yields a frequency independent contribution to the attenuation [Böm60, Dal09, Maz13].

2.4 Thin Film and Multilayered Structures

There are various reasons for the use of multilayered structures. The most obvious is firstly the possibility of coupling the functionalities of different layers to build functional devices (see introduction of perovskites in section 2.1). Secondly, multilayers are used to tailor the optical and acoustic properties of a sample. In this way, phonon [Huy06] and photon [Huy08, LK11] cavities can be fabricated and the generation and detection mechanisms can thus be enhanced [LK07]. Using a multilayer transducer for the excitation of coherent phonons, the excitation profile can be shaped [Bar98, Huy08, PW09, Her12a, Boj13, Sha13] and suitable superlattices for detection can be designed [Tri07, PW09, PW12]. Thirdly, a motivation for the use of multilayers is that a fast lattice response is generated for thin individual films: the timescale of an induced structural motion is given by d/v for a sample thickness d and sound velocity v . Some signals, however, are enhanced for thicker layers. Thus, the stacking of multiple thin films and interlayers yields an equally fast response as for a thin film, but a signal strength as in a thicker sample. This has for example been successfully applied for the development of an ultrafast Bragg switch for the shortening of x-ray pulses [Her10].

The theoretical framework for time resolved phonon light scattering developed by Thomsen *et al.* [Tho86] has been extended to multilayer samples by Matsuda and Wright [Mat02].

2.4.1 Phonons in Multilayers

Due to the periodicity in a crystalline structure, the dynamic properties of phonons and other quasiparticles are described in reciprocal space, i.e. within the first Brillouin zone. In a superlattice, where different materials are stacked periodically, an artificial, larger periodicity is introduced, which reduces the size of the Brillouin zone. This backfolding of phonons has first been studied by Colvard *et al.* [Col80] using Raman scattering techniques and later also using time resolved methods [Yam94, Bar98, Miz99, Bar99]. The backfolding is schematically illustrated in figure 2.16, where the Brillouin zone that originally extended to $q = \pi/a_0$ with the lattice constant a_0 is now reduced to $q = \pi/d_{\text{SL}}$ with the superlattice period d_{SL} . Phonons with a wavevector larger than π/d_{SL} are 'backfolded' into the smaller so-called mini-Brillouin zone. The acoustic dispersion of an infinite superlattice can

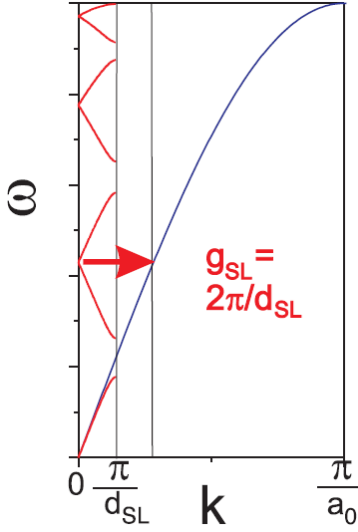


Figure 2.16: Schematic of the acoustic phonon dispersion in a superlattice [Bar04]: the acoustic branch is backfolded at the artificial boundary of the mini-Brillouin zone at $q = \pi/d_{\text{SL}}$.

analytically be calculated using the formula [Ryt56]

$$\cos(qd_{\text{SL}}) = \cos \left[2\pi\nu \left(\frac{d_1}{v_1} + \frac{d_2}{v_2} \right) \right] - \frac{1}{2} \left(\frac{|\rho_1 v_1 - \rho_2 v_2|}{(\rho_1 v_1 \rho_2 v_2)^{1/2}} \right)^2 \cdot \sin \left(\frac{2\pi\nu d_1}{v_1} \right) \sin \left(\frac{2\pi\nu d_2}{v_2} \right), \quad (2.22)$$

where d_1 and d_2 are the thicknesses of the individual layers with superlattice periodicity $d_{\text{SL}} = d_1 + d_2$, v_1 and v_2 are the sound velocities and ρ_1 and ρ_2 the densities of material 1 and 2. Since the cosine is a periodic function, its value does not change when multiples of 2π are added to the argument. We find $\cos(qd_{\text{SL}}) = \cos(qd_{\text{SL}} \pm n2\pi) = \cos((q \pm nG)d_{\text{SL}})$, meaning that the periodicity is given by the reciprocal lattice vector G with $G = 2\pi/d_{\text{SL}}$. Furthermore, the function is symmetric with respect to $q = 0$. Thus, in a simple picture, the size of the Brillouin zone that originally extended to π/a_0 , is reduced to π/d_{SL} when the larger periodicity d_{SL} is introduced. Points in the Brillouin zone beyond $q = \pi/d_{\text{SL}}$ can be displaced by multiples of the reciprocal lattice vector $G = 2\pi/d_{\text{SL}}$ in order to fit into the mini-Brillouin zone. Graphically this means that the acoustic phonon branch is backfolded into the mini-zone. Additionally, a gap in the dispersion curve opens at the edge of the mini-zone, scaling with the acoustic mismatch of the materials, as specified by the second term in equation 2.22 [Jus86]. When the acoustic mismatch is small, the energy gap at the edge of the Brillouin zone can be neglected and equation 2.22 simplifies to

$$\cos(qd_{\text{SL}}) = \cos \left[2\pi\nu \left(\frac{d_1}{v_1} + \frac{d_2}{v_2} \right) \right] = \cos(\omega d_{\text{SL}}/v_{\text{SL}}) \quad (2.23)$$

with the average sound velocity in the superlattice v_{SL} , given by

$$v_{\text{SL}} = \frac{v_1 v_2}{d_1 v_2/d_{\text{SL}} + d_2 v_1/d_{\text{SL}}}. \quad (2.24)$$

These dispersion relations only hold for infinitely large superlattices. In a finite superlattice, the curves are broadened due to the finite lifetime of the superlattice modes.

When coherent phonon dynamics are excited in a superlattice, due to the spatial periodicity the phonon wavevector $q = G$ is preferentially generated. For the frequency of this superlattice oscillations we thus find $\omega_{\text{SL}} = v_{\text{SL}}G$ or equivalently for the period t_{SL} of superlattice oscillations $t_{\text{SL}} = d_{\text{SL}}/v$.

The concept of phonons in superlattices is applied and further discussed in chapter 4.

3. Experimental Concepts

3.1 Time Resolved Pump Probe Spectroscopy

Typical periodic lattice oscillations for the multilayers investigated in this thesis are on the timescale of a few picoseconds. Electron phonon coupling in our materials happens on the hundred femtosecond timescale. In order to observe dynamics on such a short timescale, we need an excitation impulse that is short enough to trigger the coherent motion and a probing process with sufficiently short exposure time. Both prerequisites are met by a stroboscopic optical technique: an ultrashort light pulse, referred to as *pump pulse*, generates dynamics in the sample. A second pulse, the *probe pulse*, which has a certain temporal delay with respect to the excitation pulse, is used to monitor the changes of the sample response at this particular temporal delay. Changing the delay by varying the relative distance travelled by the pulses, a whole range of temporal delays can be sampled. Thus, the temporal evolution of the properties of interest can be measured. The temporal resolution of the measurement is determined by the temporal width of the pump and probe pulses. An important prerequisite for this subsequent scanning of the temporal range is the reproducibility of the induced dynamics.

Self-modelocked laser systems in the picosecond pulse duration were discovered in the 1980s [Mou86] and were further improved to obtain pulse widths in the 10 fs range for optical frequencies [Sti95]. Even shorter timescales in the attosecond range can be obtained by generating higher harmonics of the laser pulse [Pau01]. Subpicosecond resolution is obtained not only in the visible frequency range but for a very broad spectral range with terahertz [Bea02] to x-ray pulses [Ser02]. In the probe process, the optical properties of the material can be evaluated, photoemission spectroscopy gives information about the electronic states of the system [Sto04] and x-ray diffraction directly monitors the lattice motion [Ris97]. Techniques, in which changes of the polarisation of the probe are detected, give information about the magnetic state of the system [Bea96]. Locally resolved techniques have been developed, which combine temporal resolution with high spatial resolution [Kor14b]. Experiments are performed at lab-based tabletop setups or at large facilities such as synchrotrons or free electron lasers.

In this section, we introduce the experimental setup used throughout this thesis and discuss the relevant excitation and detection mechanisms in our samples. We focus on time resolved optical reflectivity measurements and on the observation of phonon dynamics with time resolved Brillouin scattering.

3.1.1 Measurement Setup

In Figure 3.1 we give an illustration of the different components employed in our experiments. A commercially available amplified titanium sapphire laser system

generates pulses of about 140 fs pulse duration with 795 nm central wavelength at a repetition rate of 5 kHz. These are each split into a strong pump pulse to excite dynamics in the sample and a weak probe pulse with which the induced dynamics are monitored. The probe pulse contains approximately 1% of the total energy. It is important to keep the probe energy low, such that the changes in the sample induced by the probe pulse can be neglected. In order to generate a variable temporal delay between pump and probe pulses, the pump is directed across a delay stage. The delay between pump and probe pulses is varied by moving the stage and hence increasing or decreasing the path length of the pump pulse with respect to the probe pulse. To give an example, an additional delay of 100 ps for the probe pulse with respect to the pump pulse is generated by decreasing the path length of the pump pulse by 3 cm. This is achieved by moving the stage by 1.5 cm. In order to measure several probe wavelengths simultaneously, a white light continuum is generated by focussing the probe into a sapphire or yttrium aluminum garnet crystal [Bra09], as further discussed below. The light reflected from the sample is detected in a fibre optic spectrometer. The sample is mounted in a closed cycle cryostat to allow for

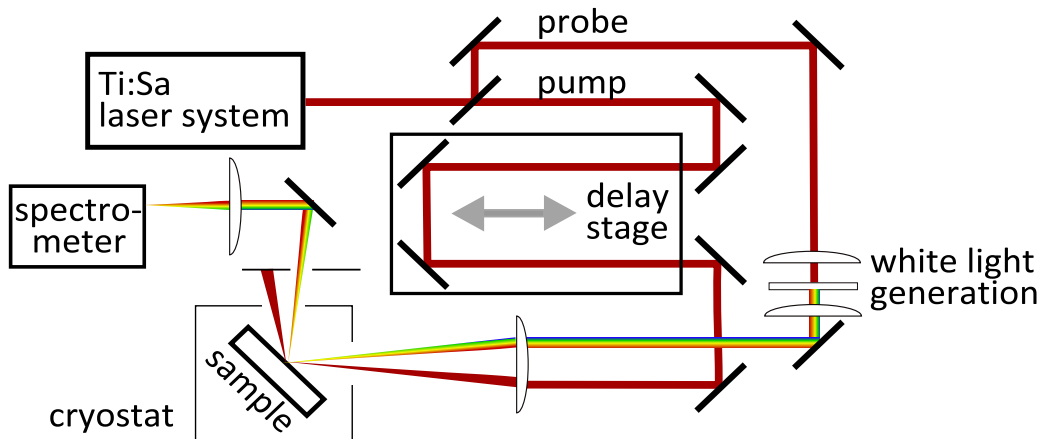


Figure 3.1: Schematic of the experimental setup employed for the measurements presented in this thesis.

temperature dependent measurements. In order to minimise the vibrations originating from the expander of the cryogenic unit, the unit containing the sample holder is mechanically decoupled. The chamber between both units is flooded with helium, which acts as a heat exchange gas and allows to reach temperatures of approximately 20 K at the sample holder. A temperature sensor is mounted to the sample holder close to the sample. The temperature is controlled using a second temperature sensor close to the built-in heater. It is important to note that the absolute temperature has not been calibrated and may vary slightly for each measurement, depending on the placement of the temperature sensor and the excitation fluence.

The absorbing layers in our samples (i.e. LSMO and SRO) are excited with a fluence of about 1 – 50 mJ/cm². The spot sizes of pump and probe pulses are determined by a CCD camera. The probe diameter typically amounts to 60 μm , the pump diameter is usually set at least 3 times larger. Since both pulses pass the same

focus lens, a telescope in both beam paths allows regulating the dimension of the focus for each beam separately. This way, a minimum spot size of the probe and a larger spot size of the pump on the sample can be adjusted. The pump fluence is calculated by the incident pulse energy and pump spot size, taking also the angle of incidence into account. The incident pulse energy can be adjusted by rotating the polarisation of the pump beam with a waveplate before it passes through a linear polariser. The losses due to the cryostat window have to be taken into account for a correct determination of the pump fluence.

In principle, the q -range observable with visible light in backscattering, as introduced in section 2.3.1, can be tuned via the incident angle. However, for simple reflection geometry, the maximum internal angle obtained for a typical refractive index of approximately $n = 2.4$ is 24° , according to Snell's law. This leads to a deviation of $\cos\theta$ in equation 2.5 from the maximum value obtained for normal incidence of $\cos\theta = 1$ of about 10 %. Larger internal angles, needed for varying the observable bandwidth more substantially, can be obtained by placing a glass prism onto the sample surface, thus making use of the so-called Kretschmann geometry [Kre71]. Polariser and waveplates can be placed in the beam paths to set the incident polarisation of each pulse.

We evaluate the normalised change in optical reflectivity in order to minimise the impact of slow intensity fluctuations in the probe pulse

$$\frac{\Delta R(t)}{R_0} = \frac{R(t) - R_0}{R_0}, \quad (3.1)$$

where $R(t)$ is the time dependent detected intensity reflected from the pumped sample and R_0 is the detected intensity reflected of the unpumped sample.

The integration time of the spectrometer is typically set to about 2 ms, thus averaging approximately 10 pulses for each recorded data point. A chopper set to a frequency of 125 Hz periodically blocks the pump beam such that every 8 ms pumped and unpumped reflectivity spectra are recorded. Zero time delay is either determined by frequency resolved optical gating, as will be discussed below, or else by the steepest slope in the rising edge of the recorded reflectivity signal, which originates in the heating of the electronic system in the metal layers.

3.1.2 Broadband Detection

For probing with a broad light spectrum, a white light continuum is generated. The small fraction of the laser beam that has been split off for probing is focussed into an optically nonlinear transparent medium. For a certain intensity level, self-focussing of the beam sets in and the high energy density results in the generation of a white light filament [Bro99]. The ongoing processes are complicated and not well understood, however, a stable continuum can be generated and used for optical spectroscopy. The generated spectrum depends on the bandgap of the material used for the generation process. Sapphire is frequently used for the generation of white light. For more light in the near infrared, we also use an yttrium aluminum garnet crystal [Bra09].

Frequency Resolved Optical Gating (FROG)

Since all wavelengths experience a different dispersion in the generating material and subsequent optical elements, such as lenses and polarisers, they arrive at different times at the sample, the white light pulse is 'chirped'. The arrival time for each wavelength can be determined by frequency resolved optical gating [Tre93]: the p -polarised white light beam, to which we will here refer as signal pulse, is focussed into a glass plate. The transmitted light passes through an analysing polariser, which is adjusted such that the transmission is minimised, i.e. to transmit only s -polarised light. The pump pulse, acting as a gate pulse, is turned by a waveplate to a polarisation of about 45° to the incident white light and also focussed into the glass plate. When both pulses overlap, they interact due to the optical nonlinearity of the material. The third order susceptibility $\chi^{(3)}$ induces a fraction of s -polarised light in the signal that can now pass the analyser and is detected in the spectrometer. The gate pulse with a pulse length of about 140 fs cuts out the slice of wavelengths that is present at the particular time.

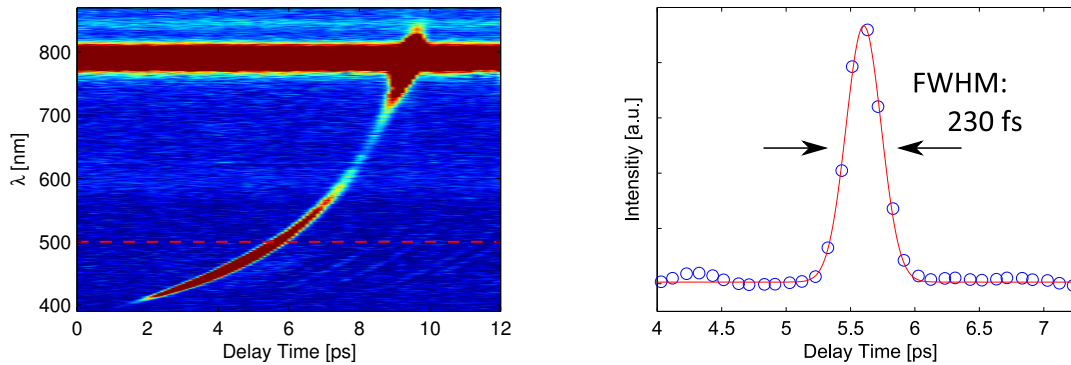


Figure 3.2: Left: FROG, measured time dependence of the arrival of different wavelengths in the white light pulse. Right: cut through the FROG measurement at $\lambda = 500$ nm and gaussian fit with a full width at half maximum of 230 fs yielding a temporal duration of the 500 nm component of approximately 200 fs, [Gol14b] assuming a pulselength of the non-optimised infrared gate pulse of 150 fs.

Figure 3.2 displays a typical FROG measurement for our setup. The white light pulse covers a wavelength range from just above 400 nm to approximately 840 nm. In this measurement, it extends over as much as eight picoseconds. The pulse length for each wavelength is estimated to amount to approximately 200 fs. The uncertainty in the determination of zero time delay is determined by the uncertainty of the fit and is usually much smaller than the width of the crosscorrelated pulse. In order to ensure the correct value for zero time delay in our measurements and the right temporal dynamics, the FROG measurement has to be taken into account in the evaluation of the time resolved data.

3.1.3 Typical Measurements: Transient Reflectivity Changes

In figure 3.3 we display a typical time resolved signal for an arbitrarily chosen probe wavelength. The normalised change in the optical reflectivity is zero before $t = 0$. At $t = 0$ the electronic system is rapidly heated. This leads to an instantaneous change in optical reflectivity that is positive in this measurement. Subsequently, the

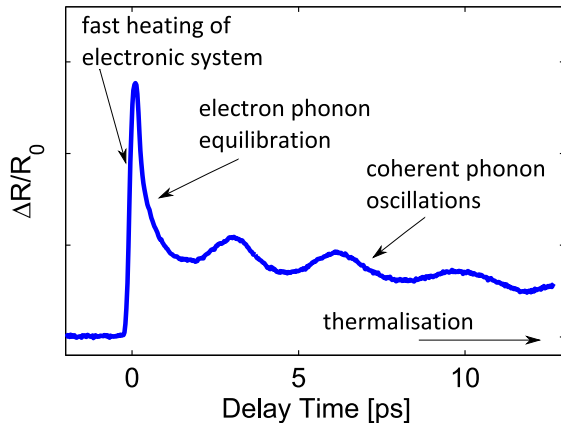


Figure 3.3: Typical time dependent reflectivity signal for an arbitrary probe wavelength. The measurement was taken on an SRO-STO superlattice, which will be discussed in section 3.2.2 below.

heat is coupled into the lattice leading to a relaxation of the response. In the figure, the reflectivity decreases on a timescale of about 200 fs. Simultaneously, the strain starts propagating through the sample and the oscillations due to scattering of the light from coherent phonons, as explained in section 2.3.2 above, build up. In the evaluation of our data, we cut off the instantaneous electronic response and evaluate the subsequent dynamics. When phonon oscillations are studied, we subtract the thermalisation background obtained by smoothing the measured data in order to obtain only the oscillations. The oscillation features will be discussed in more detail in the next chapter. On the nanosecond to microsecond timescale, thermalisation effects lead to a gradual decay of the induced reflectivity change back to the value before excitation. Thermalisation effects due to phonon magnon coupling will be discussed in chapter 7.

3.1.4 Wavelength Dependent Aspects

Wavelength Dependent Excitation

In the experiments discussed in this thesis, metal layers are excited and trigger the subsequent coherent and incoherent dynamics, see section 2.3.3 on coherent phonon generation. For this intraband excitation process, the excitation wavelength is irrelevant. In principle it is possible to coherently excite phonon modes also by impulsive Raman or infrared excitation. In the latter case, the excitation wavelength has to be tuned to the energy of the phonon mode to be excited [Rin07, För11].

Wavelength Dependent Probing

Wavelength selective probing is used for several reasons. The electronic configuration may be altered after excitation, which is best probed by certain characteristic wavelengths. In manganites, the formation of quasiparticles, the so-called polarons, is evidenced by the observation of the polaron peak in the near infrared and its temporal evolution yields information about the conduction process, compare section 7.1 on fluence dependent demagnetisation dynamics in manganites. In the case of selective excitation of certain phonon wavevectors, the probe process needs to be sensitive to these generated phonons and thus certain photon wavevectors for probing are desired.

3.1.5 Implications of Detection Scheme – Resolution and Apparent Damping of Coherent Phonons

The wavelength resolution of the spectrometer employed is about 0.6 nm. Differentiating the relation $E = hc/\lambda$ with respect to λ we find that the energy resolution ΔE given by $\Delta E = hc\Delta\lambda/\lambda^2$, with Planck's constant h and speed of light c , amounts to typically 2 meV. This corresponds to a frequency of 0.5 THz or an oscillation period of about 2 ps. Frequencies lower than this can only be resolved in the temporal domain, while higher frequencies can also be resolved spectrally, if the spectrum is appropriately narrowed [Gol14a]. The temporal resolution, on the other hand, is given by the pulse duration. The spectrum of an ultrashort pulse of high intensity can artificially be broadened by noncollinear parametric optical amplification leading to a pulse duration of about 30 femtoseconds, thus increasing the temporal resolution.

Various processes determine the decay time of an observed phonon oscillation. Firstly, the optical penetration depth determines the depth to which phonons or other quasiparticles can be optically detected. Secondly, the thickness of a layered sample determines how long the excited phonons are present in the layers and thus, how long a superlattice oscillation maximally lives, as discussed in section 2.4. Thirdly, for phonons observed in backscattering, multiple processes lead to an apparent decay.

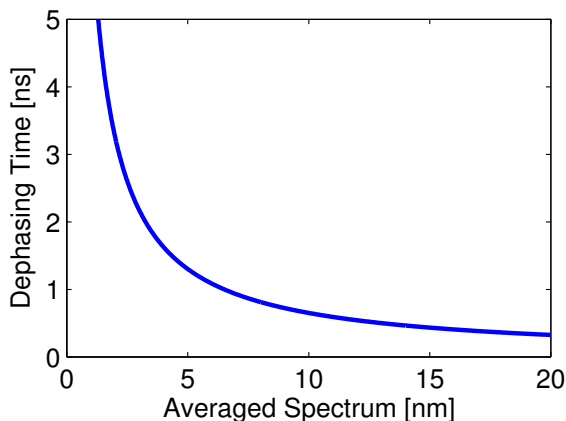


Figure 3.4: Calculated dephasing time Δt of the phonon signal observed in backscattering originating from the averaging over a certain spectral width. The averaging leads to a dephasing of the phonons detected and thus to an apparent damping of the signal. Period calculated for $\lambda = 500$ nm and normal incidence.

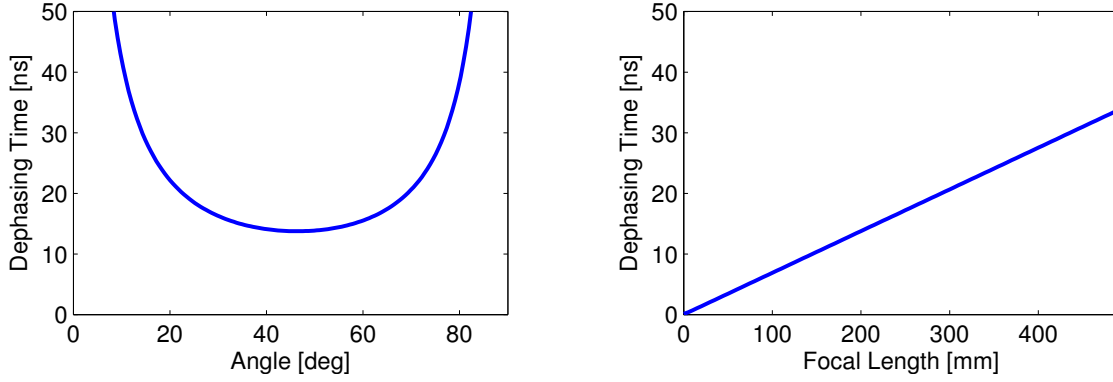


Figure 3.5: Dephasing time Δt due to the noncollinearity of the probe beam. Left: beating period as a function of incident angle for a focal length of 200 mm. Right: beating period as function of focal length for an external incident angle of 45° .

This apparent decay is imposed by the limited spectral resolution of the setup and originates in the wavelength dependence of the phonon oscillation period, leading to a dephasing of the oscillations. With the optical wavelength λ we are sensitive to phonons with frequency $\nu = 2vn\cos\theta/\lambda$, as given by equation 2.8. Differentiating with respect to λ , but ignoring the wavelength dependence of n in the derivation, we deduce $\Delta\nu = 2vn(\lambda)\cos\theta\Delta\lambda/\lambda^2$ or $\Delta t = \lambda^2/2vn(\lambda)\cos\theta\Delta\lambda$. The averaging of phonons with slightly different frequencies leads to a dephasing of the scattered signal given by the time interval Δt . Thus, the averaging over a certain spectral width may lead to an apparent faster decay of the phonons. In Figure 3.4 we plot the dephasing time Δt as a function of the averaged wavelength range. Finally, the noncollinearity angle, under which the phonons are observed, also leads to a dephasing of the oscillations. For a beam diameter on the lens of d_{lens} and a focal length of f , the maximum noncollinearity angle, $\Delta\theta_{\text{ext}}$, under which the photons hit the sample is according to linear optics given by $\Delta\theta_{\text{ext}} = \arctan(\frac{d_{\text{lens}}}{2f})$. Differentiating equation 2.9 with respect to θ_{ext} , we obtain $\Delta t = \lambda\sqrt{n^2 - \sin^2\theta_{\text{ext}}}/2v\sin\theta_{\text{ext}}\cos\theta_{\text{ext}}\Delta\theta_{\text{ext}}$.

Figure 3.5 displays the estimated damping time of the observed oscillations dependent on the incident angle and, for a given incident angle, dependent on the focal length of the lens. In this estimation, we describe the beam path according to linear optics. In reality, the gaussian pulse has a beam waist [Rul05], in which the beam is collinear. Therefore, the divergence at the sample can be expected to be smaller than estimated and the apparent damping due to the noncollinearity of the probe pulse should be even smaller in reality. In our setup we have observed phonon oscillations with a decay time of more than 5 ns in a DyScO₃ sample at an incident angle of $\theta_{\text{ext}} \approx 35^\circ$. The phonon oscillations discussed in this thesis exhibit a decay time of 1 ns or less. Therefore we have experimentally proven that the observed decay times are intrinsic and not limited by our experimental setup.

3.1.6 Normalisation of Coherent Phonon Amplitude

According to equation 2.6, the detected time dependent signal is given as $I_q(t) = A_r^2 + 2A_r A_q(t) \cos(\omega_q t) + A_q(t)^2$, where A_r is the static reference amplitude of the reflected light field and $A_q(t)$ is the time dependent light amplitude reflected from the phonons. However, in most experiments, the reflection from the sample surface, A_r , is not static but displays a time dependence due to thermalisation effects. This can be accounted for by introducing a normalisation according to

$$A_q(t) \cos(\omega_q t) \propto \frac{\left(\frac{\Delta R}{R_0}\right)_{\text{HP}}}{\sqrt{\left(\frac{\Delta R}{R_0}\right)_{\text{LP}} + 1}}, \quad (3.2)$$

where $\left(\frac{\Delta R}{R_0}\right)_{\text{HP}}$ and $\left(\frac{\Delta R}{R_0}\right)_{\text{LP}}$ are the signal intensities obtained by highpass and low-pass filtering, respectively: in the highpass filtering process, we obtain the time dependent oscillation around zero, in the lowpass filtering we obtain the slowly varying background that is subtracted from the data to obtain the highpass phonon signal. For a derivation of the relation see appendix A.2. When the relative gradual change in reflectivity is small in comparison to 1, this normalisation can be omitted. This is usually the case if the sample is probed from the front side, where typical relative changes in sample reflectivity amount to less than 0.2 in our fluence range. However, when the sample is probed from the backside and the reflection from the substrate to air interface is blocked, the relative change in reflectivity can become larger than 1 and the normalisation scheme becomes important for a correct determination of the phonon attenuation.

3.2 High Fluence Excitation

While the signal to noise level in our measurements is similar to measurements with non-amplified laser pulses at higher repetition rates, high fluence excitation allows us to observe nonlinear effects that are not accessible with lower excitation fluences. We observe a strain dependence of the sound velocity due to the anharmonicity of the atomic interaction potential and other nonlinear effects that will be discussed below.

3.2.1 Effects of Anharmonicity

As discussed in section 2.3.5, the anharmonicity of the interatomic potential leads to different sound velocities for the compressive and tensile components of the strain pulse. The wavepackets that we coherently excite are generally composed of a leading compressive and a trailing tensile strain front, as explained in section 2.3.3. For high excitation levels, the presence of different sound velocities leads to a beating of the phonon oscillation observed via backscattering. This can be expressed by the formula

$$\nu_{\text{beating}} = \Delta v 2n(\lambda) \cos(\beta) / \lambda . \quad (3.3)$$

In figure 3.6 we display high fluence data for three selected probe wavelengths at room temperature. A more detailed study of the anharmonicity effect on the sound velocity

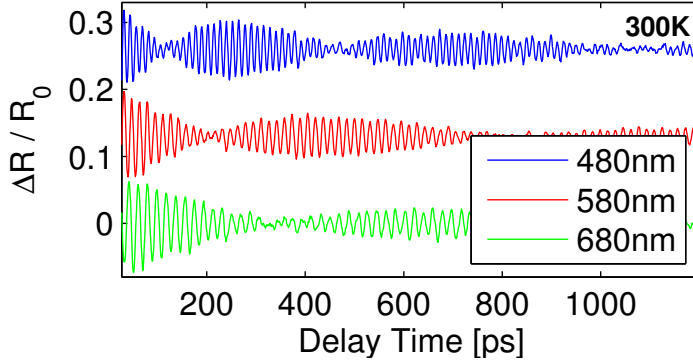


Figure 3.6: Transient reflectivity change at room temperature for high excitation fluences, plotted for different probe wavelengths. The curves are shifted vertically for clarity.

in STO and a comparison to linear chain model calculations can be found in [Boj12a]. The measurements were performed on an STO substrate with a 37 nm thick LSMO transducer. The raw data are cut shortly after the electron phonon equilibration and the slowly varying thermalisation background is subtracted. The remaining signal oscillates at the frequency given by equation 2.8. In addition, the signal oscillations are modulated by a slow, wavelength dependent beating, as described by equation 3.3. This beating is attributed to the difference Δv of the sound velocities present in the material [Mus02, Boj12a, Sha13]. In this case, for large amplitude strain in STO at room temperature, the sound velocity for compressive strain is larger than that for tensile strain. This interpretation is supported by calculations using an anharmonic linear chain model [Boj12a] and by time resolved x-ray diffraction experiments using acoustic pulse trains generated by a superlattice transducer [Sha13].

3.2.2 Fluence Dependent Excitation of Coherent Phonons

As mentioned before, we assume an instantaneous thermalisation of electrons and phonons and subsequent generation of coherent phonons in our model. This is a reasonable approximation for most of our measurements, however, it is not completely correct. Figure 3.7 displays optical reflectivity transients on a sample consisting of 10 double layers of 13 nm STO and 7.5 nm SRO. The measurements were taken at room temperature for different excitation fluences. A function of the form

$$f_{A,B,C,\varphi_0}(t) = A \cos(\omega_q t - \varphi_0) + Dt + C \quad (3.4)$$

was fitted to the data, with fit parameters A , C , D and φ_0 and oscillation frequency ω_q , which was either kept fixed for all fluences or adjusted freely for each fluence, making no difference for the obtained result. The phase shift with respect to a perfect cosine in femtoseconds, δt , is determined via $\omega_q \delta t - \varphi_0 = 0$, yielding $\delta t = \varphi_0 / \omega_q$. In the left panel of figure 3.8 we display δt extracted for different excitation fluences as

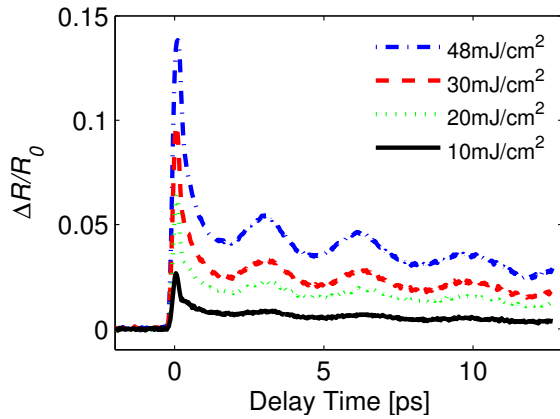


Figure 3.7: Transient reflectivity signal for the SRO/STO superlattice for four different excitation fluences.

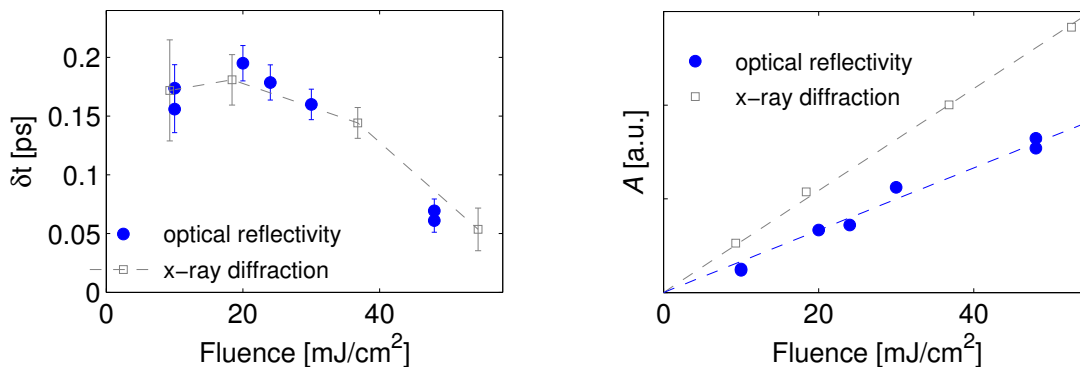


Figure 3.8: Left: fluence dependent delay of the oscillation onset for the optical data (open blue circles) and x-ray measurements (open grey squares). The error bars were determined by the deviation of results determined for the same fluence in different measurement series for the optical data and by the error of the fit for the x-ray data. Right: oscillation amplitude as a function of excitation fluence. Published in [Boj12].

full blue circles. Also shown is the temporal delay of the oscillation onset observed in x-ray diffraction experiments on the same sample as grey open squares. Since the exact phase of the oscillation observed optically depends on probe wavelength and is thus somewhat arbitrary [Boj12], the temporal shift for the optical data should be interpreted as relative shift only. For the x-ray experiments, however, the absolute phase of the oscillation can reliably be determined. The evaluated δt for the optical data has been offset in the figure to agree with the x-ray data. For high excitation fluence, the delay time determined via x-ray diffraction becomes negligible and the oscillation resembles an exact cosine. For lower excitation, the onset of the oscillation is delayed: for the lowest measured fluence, the oscillation sets in approximately 130 fs later than for the highest fluence, as observed by x-ray and optical measurements. The faster onset for high excitation can presumably be attributed to a contribution of the instantaneous electronic stress to the buildup of the coherent phonon oscillations that dominates for high excitation fluences: before the energy is coupled into the lattice, the hot electrons induce an expansion of the metal. For lower excitation, the

energy is first transferred into the lattice, before the oscillation generated by phonon mediated stress sets in. Therefore, the onset of the oscillation is delayed by the electron phonon coupling time for low excitation fluences [Boj12]. In the right panel of figure 3.8, we display the extracted fluence dependence of the oscillation amplitude, the fitparameter A , which shows a linear dependence on excitation fluence. The amplitude of the coherent phonon oscillations scales linearly with excitation fluence. Thus, independent of the microscopic generation process, the oscillation amplitude linearly depends on the energy deposited in the material.

4. Observation of Phonon Dynamics in Thin Film and Multilayered Samples

In this chapter, we illustrate the concepts introduced above. We use broadband time domain Brillouin scattering to observe coherently generated phonon modes in bulk and nanolayered samples. We discuss measurements of phonon dynamics in three different samples, as summarised in Table 4.1: (a) a 37 nm LSMO transducer film on an STO substrate, (b) an LSMO/BST superlattice with 15 double layers of 21 nm period and (c) an SRO/STO superlattice with 5 double layers of 140 nm period. The samples were prepared on STO substrates using pulsed laser deposition [Vre08a].

Table 4.1: Details of selected samples. Acronyms: interlayer (IL), amount of double layers (# DL), thin film (TF), superlattice (SL). The layer thicknesses were checked by static x-ray diffraction.

Nr.	type	metal	dielectric IL	# DL	substrate
(a)	TF	LSMO, 37 nm			STO (100)
(b)	SL	LSMO, 7.3 nm	BST, 13.7 nm	15	STO (100)
(c)	SL	SRO, 13 nm	STO, 127 nm	5	STO (100)

4.1 Reflectivity Transients

In figure 4.1 we show contourplots of the wavelength dependent transient optical reflectivity for the three different samples. The instantaneous electronic response and slow thermalisation effects have been subtracted. Sample (a) shows oscillations that are well described by equation 2.8. In this sample, the single LSMO layer expands and launches a bipolar strain pulse into the STO substrate underneath. Because of the good acoustic impedance matching between layer and substrate, the strain wave has completely entered the substrate when the strain front starting from the film-substrate interface has traveled to the sample surface, has been reflected and returned through the film into the substrate, as discussed in section 2.3.3. Thus, after about $dt = 2d_{\text{TF}}/v_{\text{LSMO}} \sim 12$ ps, where d_{TF} is the thickness of the film and v_{LSMO} is the sound velocity in the film, as listed in table 4.2, there are no further coherent dynamics in the metal film [Boj12a].

We have therefore cut off the first 12 ps from our data and only display the dynamics in the bulk STO underneath. For sample (b) in figure 4.1(b), we also observe these probe wavelength dependent oscillations according to equation 2.8. Here, we focus on the first 100 ps of the dynamics, in which the excited pulse train is still present in the superlattice. In this comparatively short time window (for

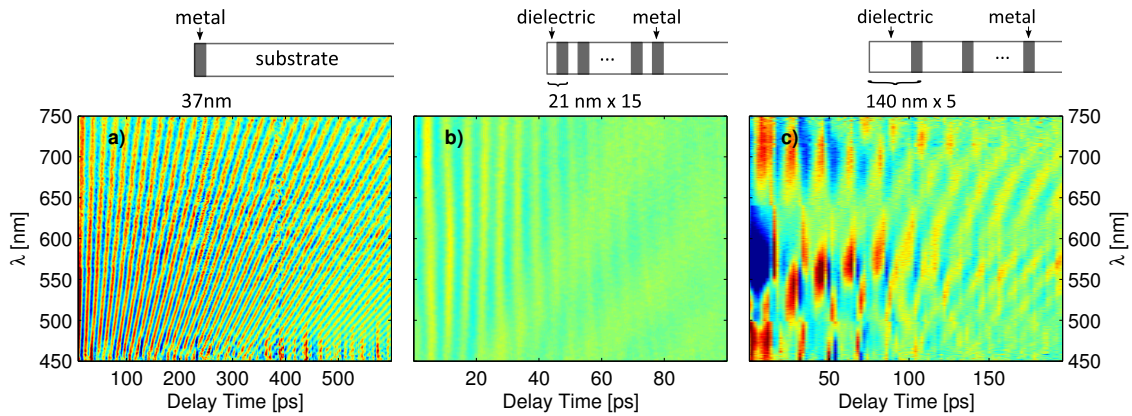


Figure 4.1: Broadband time resolved reflectivity data at room temperature for different samples. Colour code: $\Delta R/R_0$ [a.u.], slowly varying background subtracted. (a) Thin LSMO layer on bulk STO, (b) LSMO-BST superlattice with 21 nm period, (c) SRO-STO superlattice with 140 nm period. The time scales are different in each panel. The geometries of the samples are schematically shown above each graph. In all graphs, the wavelength dependent oscillation period of the travelling phonon, seen via phonon backscattering, is clearly visible. In (b) and (c) the standing SL phonon showing a wavelength independent oscillation frequency, as observed via forward scattering is also discernible. Note the different temporal windows shown in the graphs.

Table 4.2: Sound velocities applied in the calculations in [nm/ps], v_b and v_c denote the average sound velocities in the superlattices for samples (b) and (c) according to equation 2.24.

$v_{\text{STO, layer}}$	v_{LSMO}	v_{BST}	v_{SRO}	$v_{\text{STO, substrate}}$	v_b	v_c
7.8	6.5	5.1	6.3	8	5.5	7.6

comparison: in figure 4.1(a), 600 ps are displayed), these appear as slow oscillations with a period of 10-20 ps, depending on probe wavelength. In addition, we observe the wavelength independent, forward scattering signature, that has been conceptually introduced in section 2.3 of the standing superlattice oscillation with period $t_{\text{SL}} = d_{\text{SL}}/v_b \sim 3$ ps, using the appropriate spatial period $d_{\text{SL}} = 21$ nm and the average sound velocity in the superlattice of $v_b \approx 5.5$ nm/ps. For sample (c) forward- and backscattering signals have similar periods. The sample is designed such that the energy of the standing superlattice phonon approximately coincides with the energy of the longitudinal acoustic phonon in the centre of the frequency window, where Brillouin scattering is observable by visible light. Thus, the wavelength independent oscillation and the oscillation dependent on wavelength are superimposed, leading to the complicated pattern in figure 4.1(c).

In the superlattices discussed here, the dynamics in the layers are actually much shorter than $dt = 2d_{\text{SL}}/v_{\text{SL}}$. The reason is that the overall thickness of the absorbing

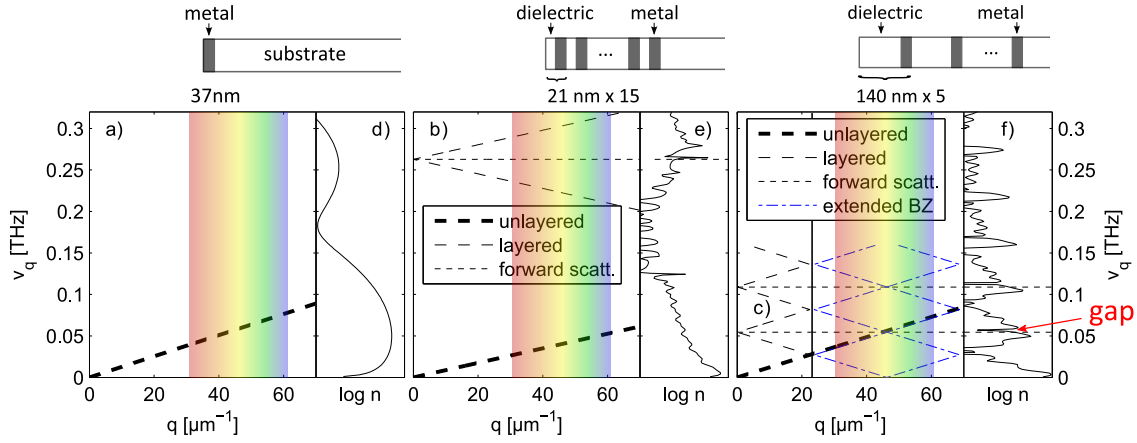


Figure 4.2: (a)-(c) Calculated dispersion relations for the three samples according to equation 2.22. (a) Single layer, simple acoustic dispersion (black thick dashed line). (b) Superlattice with small periodicity, the acoustic dispersion (black thick dashed line) is backfolded at Brillouin zone edge $\pi/d_{\text{SL}} = 140\mu\text{m}^{-1}$ (not shown), yielding the superlattice dispersion (black thin dashed line) with additional branches. The frequency of the $q \approx 0$ superlattice mode is indicated as thin dotted horizontal line (see main text). (c) Superlattice with periodicity of 140 nm. The acoustic dispersion (black thick dashed line) is backfolded at the Brillouin zone edge $\pi/d_{\text{SL}} = 23\mu\text{m}^{-1}$, yielding the SL-dispersion (black thin dashed line). The first zone scheme can be extended by adding a reciprocal lattice vector $G_{\text{SL}} = 2\pi/d_{\text{SL}}$ yielding the dispersion relation in the second Brillouin zone (blue dash-dotted line). The $q \approx 0$ superlattice mode again indicated as thin dotted horizontal line. The optically observable q -range in backscattering is indicated by the rainbow coloured region in each plot. (d)-(f) Corresponding occupation of the excited modes as calculated in the linear chain model (introduced in section 2.3.4).

layers is large compared to the penetration depth of the pump light in these materials. In sample (b), the thickness of the metal amounts to 110 nm. In LSMO the penetration depth for 795 nm light is 65 nm. This means that only about 20 % of the pump and probe light reach the lowest absorbing layer. It is therefore much more weakly excited than the top layer and contributes less to the detected signal. In sample (c) the metal layers are thinner, but at the same time the penetration depth is smaller and amounts to 44 nm in the metal. This means that only about 40 % of the pump and probe energies reach the lowest absorbing layer. Thus, most of the coherent dynamics in the superlattices have ceased, once the most dominant strain front starting at the surface has passed into the substrate. This happens after about 57 ps for sample (b) and after about 92 ps for sample (c).

4.2 Calculated Dispersion Relations

The dispersion curves of our samples calculated according to equation 2.22 and the parameters in Tables 4.1 and 4.2, are shown in Figure 4.2 (a)-(c). In (a) the linear acoustic dispersion of the acoustic phonon branch in bulk STO is displayed. The

q -range accessible in our experiment via backscattering is indicated by the rainbow coloured region. In sample (b) the stacking of LSMO and BST layers with period d_{SL} results in a reduction of the Brillouin zone and leads thus to the backfolding of all phonon branches, as here shown for the observed longitudinal acoustic phonon branch. The frequency of the $q \approx 0$ superlattice phonon is visible for all probe wavelengths via forwardscattering and is therefore indicated as thin dashed horizontal line¹ although the q -value on the axis only holds for phonons observed in backscattering. Figure 4.2(c) shows the dispersion curve of the even larger superlattice (140 nm period) with yet smaller Brillouin zone. In this case, the q -range accessible by our probe technique via backscattering lies outside of the first Brillouin zone and we show an extended zone scheme, indicated as blue dash-dotted line, where multiples of the reciprocal lattice vector G_{SL} are added to each point in the mini-Brillouin zone. Again, the $q \approx 0$ phonon observable for all probe wavelengths is indicated as thin dashed line. In this superlattice, nearly the whole q -range of the mini-Brillouin zone lies in the visible spectrum if a reciprocal lattice vector is added to each point. This is possible if the detectable phonon bandwidth $\Delta q = q_{\text{min}} - q_{\text{max}}$ amounts to at least the maximum wavevector in the Brillouin zone π/d_{SL} , q_{min} and q_{max} being the minimum and maximum detectable phonon wavevector in backscattering. If one octave is covered in probe bandwidth as approximately in our case: $q_{\text{max}} \approx 2q_{\text{min}}$, it follows that $\Delta q \approx q_{\text{min}}$. Thus, the whole q -range of the Brillouin zone can in principle be covered with one octave if $q_{\text{min}} > \pi/d_{\text{SL}}$.

The occupation of each mode, i.e. the number of phonons in each mode, can be calculated analytically using a linear chain model [Sch14a, Her11]. We again chose the layer parameters according to Tables 4.1 and 4.2 and built a substrate composed of 5000 unit cells underneath. We assume an instantaneous heating and subsequent rapid expansion of the absorbing metal layers, as explained in section 2.3.3. Since no anharmonic effects are included in the calculations, the obtained results scale linearly with the excitation fluence. The results for the samples are shown in Figure 4.2 (d)-(f). In (d), a broad spectrum of modes is excited around $q \approx \pi/d_{\text{TF}}$, with film thickness d_{TF} [Boj13], as explained in section 2.3.3 on coherent phonon generation. In the superlattices, panels (e) and (f), modes around $q = G_{\text{SL}}$ are dominantly excited, which are backfolded to $q = 0$, as explained in section 2.4.1 on phonons in multilayers.

4.3 Measured Dispersion Relations

In the following, we compare the calculations with our measurements. Figure 4.3 (a)-

¹The maximum detected phonon frequency in our experiments is $\nu \approx 0.25$ THz via forward scattering (compare figure 4.2 (b)), higher orders are too weakly excited to be detected. If the phonon dispersion is assumed to be flat at the intersection (compare illustration of energy and momentum conservation in figure 2.7 (a)), the change in photon wavevector, and therefore q of the detected phonon, amounts to $0.006 \mu\text{m}^{-1}$ and is by far too small to be displayed in the graph. This underlines that $q \approx 0$ is indeed a reasonable approximation for forward scattering in these experiments.

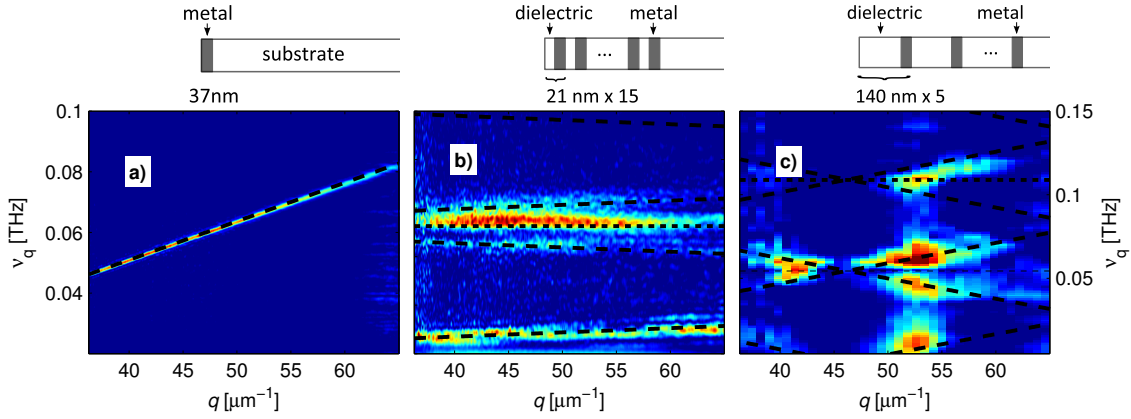


Figure 4.3: Fourier transform of data in Figure 4.1 for the three different samples. wavelength axis has been converted to phonon wavevector for backscattering, calculations are overlaid. Colour code: Fourier amplitude [a.u.].

(c) shows temporal Fourier transforms of the original data from figure 4.1 performed for each wavelength as contourplots.² The wavelength axis has been converted to display the phonon wavevector $q = 4\pi n(\lambda) \cos(\theta)/\lambda$ for backscattering and the axes were interchanged to display the phonon frequency as a function of wavevector. The results of the calculations are overlaid. In (a), we find the linear acoustic dispersion of bulk STO. In figure 4.3 (b) we observe the linear dispersion of the acoustic branch, traces of the first and second backfolded branches and the wavelength independent signature of the $q \approx 0$ superlattice oscillation via forward scattering. The occupation number shown in figure 4.2 (e) reveals, why the wavelength independent oscillations dominate the signal: in this sample, the backfolded phonon modes observed via backscattering are only weakly excited. Figure 4.3 (c) shows the diamond shape dispersion curve according to the extended zone scheme (compare Figure 4.2 (c)). Here, the forward scattering signal is nearly invisible. In the vicinity of $q = nG_{\text{SL}}$ many modes are populated, as shown in figure 4.2 (f). These can be observed by the white light probe in backscattering and dominate the signal. For intermediate wavevectors, $q \approx \frac{2n+1}{2}$, there is a minimum in the occupation, indicated in figure 4.2 by the red arrow. The location of this minimum depends on the phase between the leading compressive and the trailing tensile part of the propagating strain profile, which has been illustrated in figure 2.12, leading to destructive interference for a certain frequency.

The differences between theory and experiment, e.g. the intensity just below and above the first backfolded zone centre mode for sample (c), might be due to sample inhomogeneities particularly at the sample surface or anharmonic effects that lead to changes in the spectrum of excited modes [Boj13]. Additionally, the relative intensities of the frequencies in the Fourier transforms depend on the length of the time window chosen for the transform and the high pass filtering that was performed

²A quantitative wavevector dependent comparison between experimental results and calculations cannot easily be performed for the superlattices, as explained in appendix A.1.

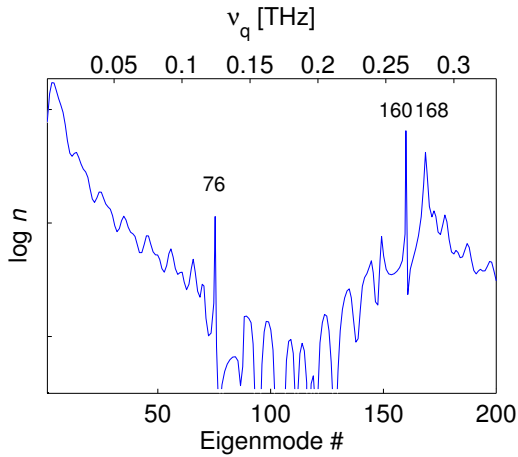


Figure 4.4: Occupation of modes for sample (b) as a function of mode eigenfrequency (top axis, in THz) and assigned number (bottom axis) given by the calculation. The peaks are at mode number 76, 160 and 168.

in order to extract the oscillations. The width of the individual peaks may lead to an interference of forward and backscattered light, which might be the reason for the asymmetry of the forward scattered peak for sample (b). Furthermore, the intensity detected for each q -vector also depends on the optical properties of the samples, how these change with strain and thus on the sample structure.

4.4 Eigenmodes of the Superlattice

In this and the following section, we mainly discuss features for sample (b), but most observations can be generalised and hold for other superlattices as well. We focus on sample (b), since some of the findings will be relevant for further measurements on this sample, which will be discussed in chapter 7.

For a given sample geometry and number of unit cells, N , incorporated in the linear chain model, we obtain N eigenmodes of the system. In figure 4.4 we again display the calculated occupation of eigenmodes for sample (b) from figure 4.2 (e) as a function of oscillation frequency (top axis) and additionally as a function of assigned eigenmode number (bottom axis), where the calculated eigenmode with lowest frequency is counted as 'one' and the eigenmode with highest frequency is counted as ' N '. Some modes are highly populated. The modes with highest phonon population, i.e. the peaks in the graph correspond to eigenmodes 76, 160 and 168. In figure 4.5, we plot the modes that are highly excited as solid lines and those that are more weakly excited as dashed lines. The vertical lines indicate the interfaces between the LSMO and BST layers and between LSMO and substrate STO. Mode 76 is the eigenmode with a spatial period of half the superlattice period, i.e. every second layer of the same material shows an equal strain condition. Furthermore, the mode displays a decay of the strain amplitude from surface to substrate. Mode 160 and 168 have the same period as the superlattice. Mode 160 displays a decay in strain amplitude from surface to substrate while mode 168 displays a node at the surface and the interface to the substrate.

The superposition of eigenmodes leads to the spatial profile of the excitation as

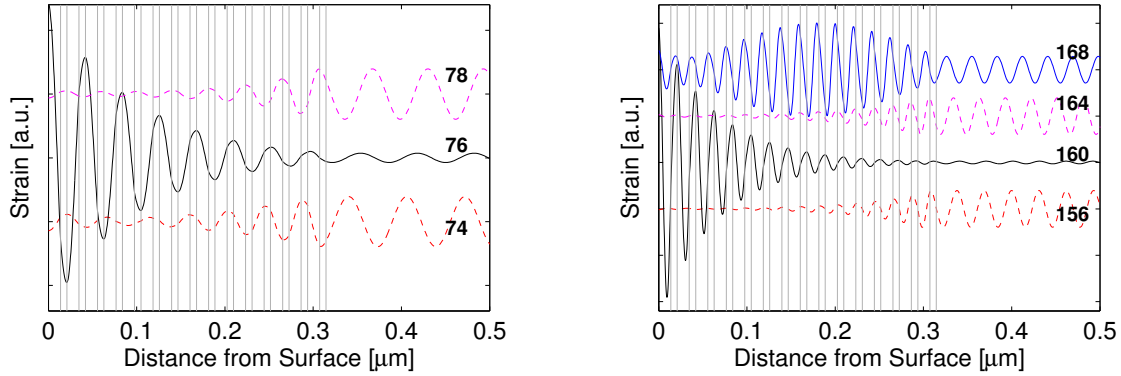


Figure 4.5: Eigenmodes of sample (b). The solid lines represent modes that are highly excited, the dashed lines represent modes that are only little excited. The vertical grey lines indicate the interfaces between metal and dielectric. The metal is the thinner layer in the superlattice. Left: modes 74, 76 and 78 from figure 4.4 (from bottom to top). Right: modes 156, 160, 164 and 168 (from bottom to top).

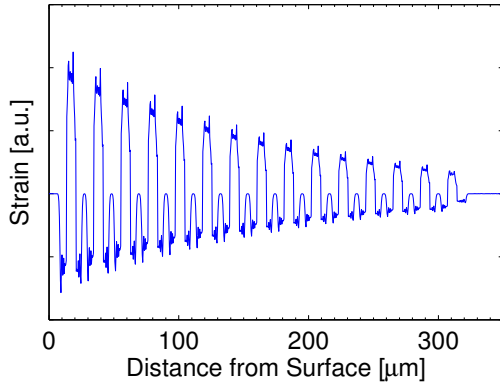


Figure 4.6: Strain profile 1 ps after excitation calculated from the eigenmodes of the system.

displayed in figure 4.6 for a time delay of 1 ps: the metal layers are highly strained but the strain already starts propagating into the dielectric interlayers and the substrate. For all delays, the corresponding strain profile in layer and substrate can be calculated from the eigenmodes. In the harmonic model, the modes themselves and their occupation stay constant for all times, only their relative phases vary with time. Constructive and destructive interference of the modes leads to the propagation of the phonon wavepacket (see also [Sha13, Sch14b]).

4.5 Temporal Evolution of the Spectrum

When the phonon wavepacket has passed the superlattice and propagates into the substrate, the previously backfolded branches of the phonon dispersion unfold [Tri08, Sha13] and the acoustic dispersion in bulk STO is retrieved. This is shown in figure 4.7 for sample (b), the thin LSMO/STO superlattice. In the left graph, the Fourier transform of the first 57 ps is shown as a contourplot. Within 57 ps, the strain front starting at the surface of the sample has mostly traversed the superlattice and has

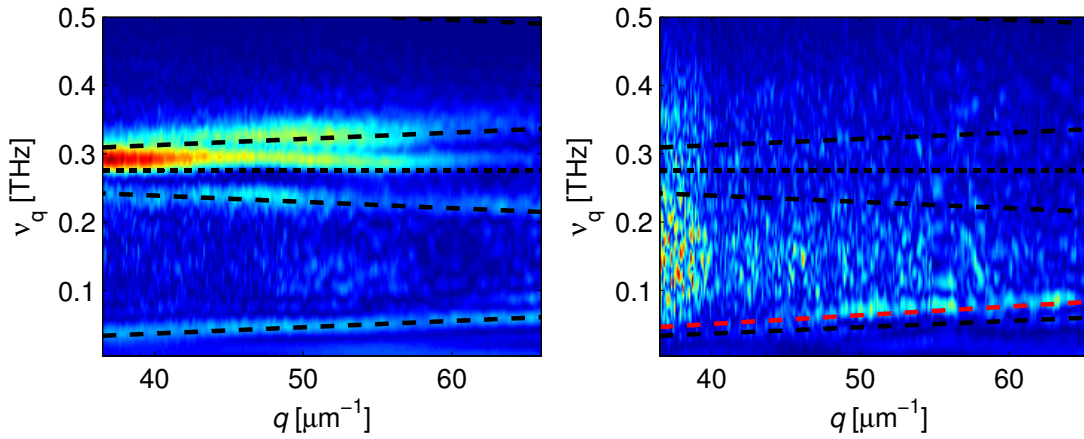


Figure 4.7: Left: Fourier transform of the first 57 ps of the time resolved reflectivity data measured at 50 K. Right: Fourier transform of the temporal window from 55 to 112 ps. A notable change in slope of the acoustic branch is detected. The sound velocity in the superlattice is about 5% larger than at room temperature, as will be discussed in section 7. Colour code: Fourier amplitude [a.u.].

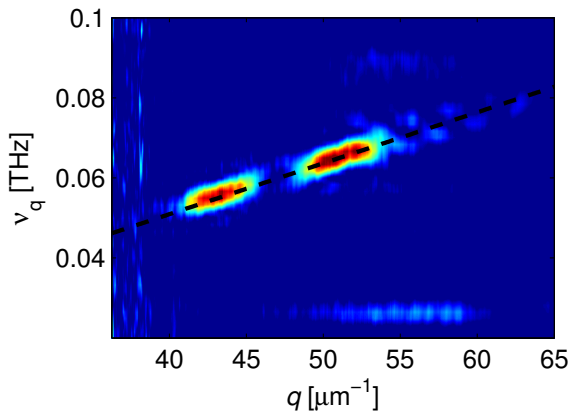


Figure 4.8: Fourier transform of the time resolved reflectivity data of the first 450 ps from sample (c), where the first 150 ps have been cut out (temporal trace not shown), calculated dispersion overlaid. Colour code: Fourier amplitude [a.u.].

propagated into the substrate. As discussed above, the strain front starting at the metal-substrate interface is small: only about 20 % of the excitation fluence reaches the bottom layer of the superlattice since the excitation depth of LSMO for 795 nm light amounts to 65 nm. Thus, after about 57 ps the coherent dynamics have mostly propagated into the substrate. In the right graph, the Fourier transform of a temporal window with the same length of 57 ps but starting at a delay of 55 ps is displayed. For this time interval, the backfolded branches have vanished and the dispersion of acoustic phonons in bulk STO is obtained. The theoretical curve is represented by the red dashed line in the right graph. The dispersion in STO is notably steeper than the lowest branch of the superlattice dispersion, shown as black dashed line, due to the higher sound velocity in STO, as listed in table 4.2.

Similarly, in figure 4.8, we display the Fourier transform of the measured first 450 ps for sample (c), i.e. the the SRO/STO superlattice with large periodicity, where the first 150 picoseconds with dynamics still present in the superlattice have

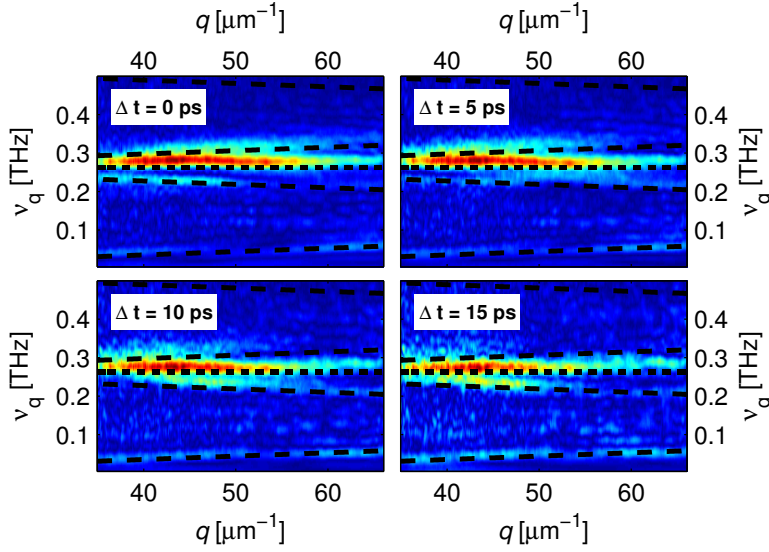


Figure 4.9: Fourier transformed time windows with 57 ps length, each shifted by 5 ps with respect to the previous. The measurements were taken at room temperature. The relative intensities of the occupied modes change with time. Colour code: Fourier amplitude [a.u.].

been cut out. In this sample, sound traverses the superlattice within about 90 ps. The light reaching the lowest absorbing layer amounts to about 40 % of the intensity at the top layer, as calculated using the optical penetration depth of SRO of 45 nm for 795 nm light. The dynamics in the first 180 picoseconds and their Fourier transform have already been displayed in figures 4.1 and 4.3 above. The amplitude is now modulated in agreement with the simulations shown in figure 4.2 (f): there is no intensity below 0.05 THz, a minimum around 0.06 THz and no intensity above 0.07 THz. In comparison to the calculations, the occupation is shifted to slightly higher frequencies due to the anharmonic coupling: for the leading compressive part (compare illustration of strain profile in figure 2.12), each of the five components travels with slightly different velocity. The distance between the five components decreases, such that the fundamental frequency is shifted towards higher frequencies. The same effect happens for the trailing tensile part of the wavepacket. Additionally, the slope of the acoustic branch is slightly increased in comparison to figure 4.3 (c) but this is not as clearly visible as for sample (b), since the superlattice consists mostly of STO rendering a sound velocity in the superlattice only slightly smaller than in the bulk, as listed in table 4.2.

For sample (b) we investigate the time dependence of the obtained spectrum in more detail. In figure 4.9 we show the Fourier transforms of 57 ps long temporal windows, each shifted by 5 ps with respect to the previous. The relative intensities of the upper and lower branches change substantially with time: the lower backfolded branch decreases in intensity and increases again for the last window displayed while the intensity of the upper backfolded branch continuously decreases. Additionally, in the two upper panels, there is a slight curvature of the forward scattering feature that decreases for later times.

This effect is more pronounced at low temperatures, as displayed in figure 4.10, now for 35 ps temporal windows and measurements taken at 50 K. For the first Fourier transform, the upper backfolded branch and the forward scattering feature

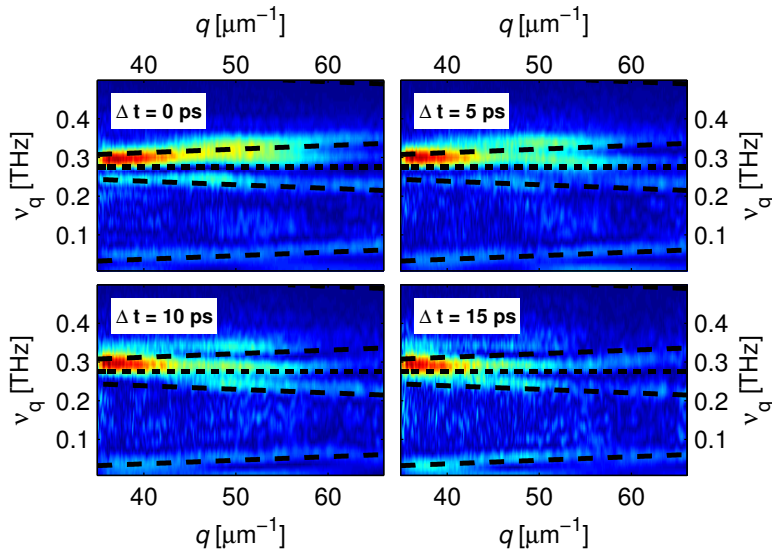


Figure 4.10: Fourier transforms of 35 ps time windows shifted by 5 ps. The relative intensity of the occupied modes changes with time. The measurements were performed at 50 K. Colour code: Fourier amplitude [a.u.].

cannot be distinguished. Since the transformed temporal window is very short, the obtained Fourier peaks are broad. This may lead to an interference of light at the detector that originates from separate physical processes, i.e. the interference of forward and backscattering signals. Thus, for the short time window, in which the coherent dynamics are present in the superlattice, the interpretation of the spectra is difficult. We will come back to this observation in chapter 7, where temperature dependent measurements are performed on this sample.

5. Coupling of Acoustic Phonons to Domain Walls in SrTiO₃

In this chapter, we discuss the elastic behaviour of STO studied by time domain Brillouin scattering. We start in the regime of linear response and extend our measurements into the regime of nonlinear sound propagation. The amplitude of the strain pulses has been calibrated using ultrafast x-ray diffraction [Boj12a, Sch12a, Sch14b]. When the hypersound strain amplitude exceeds $\sim 0.1\%$, we observe a giant reduction of the sound velocity below T_a , similar to the superelastic behaviour observed for low frequency strain that has been introduced in section 2.2.3. Our experiments suggest that this phenomenon occurs for GHz sound only when the strain amplitude is large enough to establish a new mechanism for coupling to the domain walls, which will be proposed below.

We mainly discuss experimental data obtained from a 37 nm thick LSMO transducer grown by pulsed laser deposition onto a single-crystalline (100)-STO substrate (CrysTec, Berlin, miscut angle of 0.1° [Vre08b]), to which we will refer as sample L37. Several similar samples have been measured in order to verify the conclusions, as will be discussed below. Table 5.1 summarises details of the samples studied and assigns individual labels to facilitate the discussion.

5.1 Temperature Dependence of the Sound Velocity

The elastic properties of STO show an anomalous behaviour at the antiferrodistortive phase transition at T_a , as already mentioned in section 2.2.3. In figure 5.1 we exemplarily show the time resolved optical reflectivity data measured in STO at $T = 130$ K with sample L37 for a probe wavelength of $\lambda = 528$ nm, after the smoothed background originating from the electronic response has been subtracted. The oscillations are observed via backscattering and display a wavelength dependent oscillation period according to formula 2.8. Sample L37 is identical to sample (a) in chapter 4 and wavelength dependent oscillations measured at room temperature

Table 5.1: Samples discussed in this and the following chapter. We use STO substrates with various transducer films of the materials LSMO and SRO. Labels are assigned to simplify the discussion.

label	transducer material	transducer thickness	substrate material
L37	LSMO	37 nm	STO (100)
L100	(La _{0.825} Sr _{0.175})MnO ₃	100 nm	STO (100)
L20	(SrMnO ₃) ₂ /(LaMnO ₃) ₄	20 nm	STO (100)
S15	SRO	15 nm	STO (100)
S70	SRO	70 nm	STO (100)

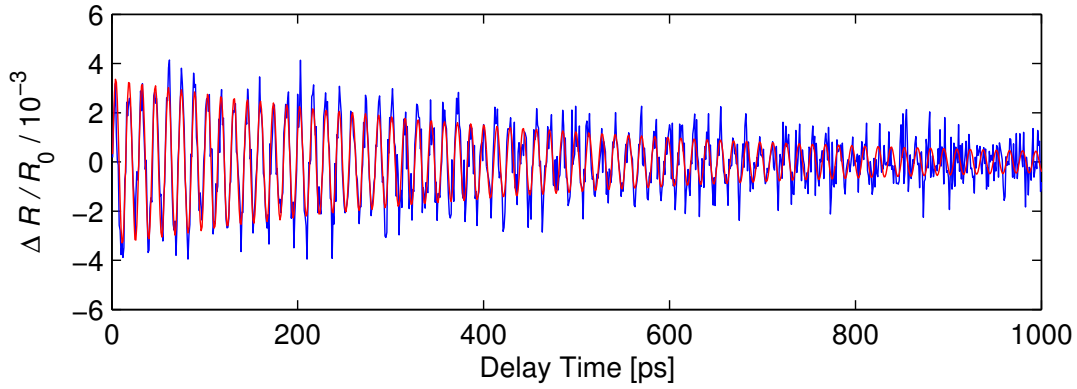


Figure 5.1: Time resolved reflectivity data for sample L37 measured $T = 130$ K and an excitation fluence of approximately 14 mJ/cm^2 shown as blue curve. The curve was measured for a central probe wavelength of $\lambda = 528 \text{ nm}$ corresponding to $q \approx 54,6 \mu\text{m}^{-1}$, averaged over 2.5 nm to obtain a smooth curve. A fit according to equation 5.1 is overlaid in red. The fit yields a phonon oscillation frequency $\omega_q = (2\pi/14.14) \text{ ps}^{-1}$ and damping time $\tau = 470 \text{ ps}$.

were shown in figure 4.1 (a). We have fitted a damped cosine function of the form

$$f_{A,\omega_q,\varphi_0,\tau,C}(t) = A \cos(\omega_q t + \varphi_0) e^{-t/\tau} + C \quad (5.1)$$

to the oscillations, using the oscillation amplitude A , angular phonon frequency ω_q , phase φ_0 , damping time τ and offset C as fit parameters. The obtained fit has been overlaid to the data in figure 5.1. The measurements were performed at different temperatures.

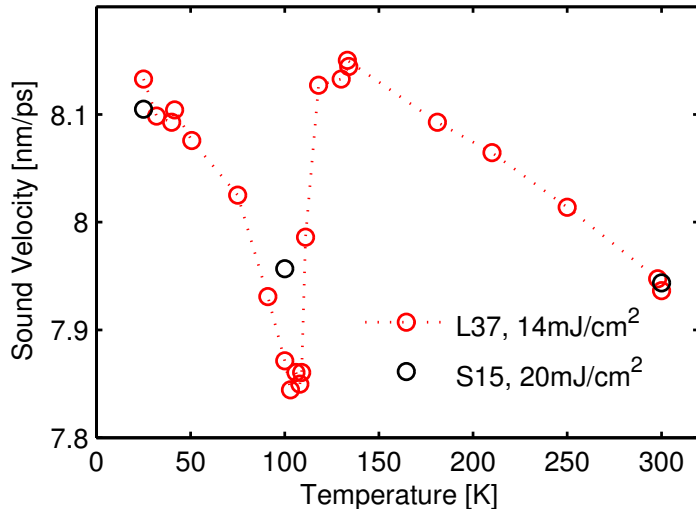


Figure 5.2: Obtained sound velocities in STO for two different transducer films. Red symbols: 37 nm LSMO transducer (sample L37), black: 15 nm SRO transducer (sample S15). For excitation fluence see legend.

In figure 5.2 we display the temperature dependence of the sound velocity as extracted from the fits and using equation 2.8. Results are shown for sample L37, indicated by the red open symbols, and for sample S15, indicated by the black open

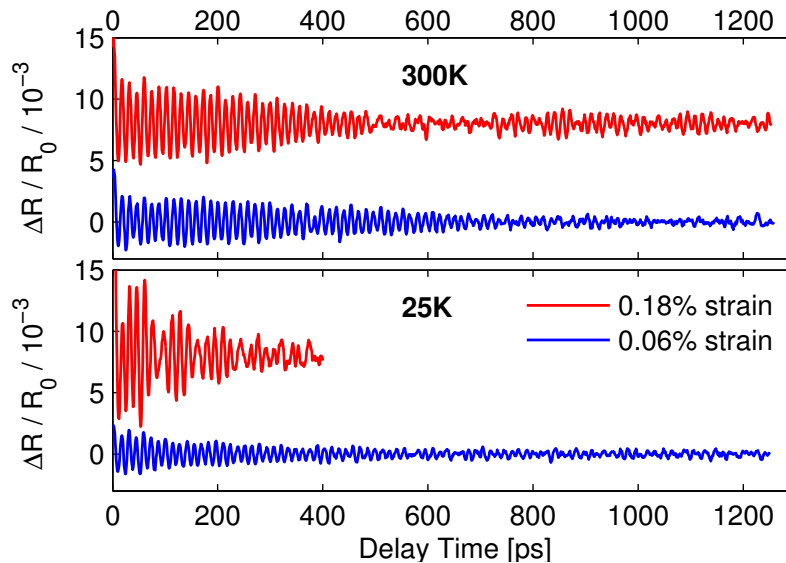


Figure 5.3: Time resolved reflectivity data for L37, measured at $T = 300$ K (upper panel) and at $T = 25$ K (lower panel) and two different strain amplitudes evaluated at $\lambda = 528$ nm ($q = 54.6\mu\text{m}^{-1}$, $\nu \approx 71$ GHz). The high strain level was obtained by an excitation fluence of approximately 45 mJ/cm², the low strain level with a fluence of approximately 15 mJ/cm². The curves are shifted vertically for clarity.

symbols. Approaching the phase transition temperature T_a from above, we note a sudden drop of the sound velocity that amounts to approximately 3%. This is in quantitative agreement with the literature [Nag12, Kai66] and originates from the coupling of the strain wave to the antiferrodistortive soft mode describing the transition [Bel63, Kai66, Fle71, Nav69, Pyt70, Reh70a, Fos72].

5.2 Nonlinear Effects I: Anharmonicity

The anharmonicity of the interatomic potential of STO leads for high strain amplitudes to the occurrence of two sound velocities, as discussed in section 3.2.1. These are observed in the optical reflectivity response as a beating of the phonon oscillation. In the upper panel of figure 5.3, we display time dependent optical reflectivity data of L37, measured at $T = 300$ K for two different excitation levels. The amplitude of the generated sound pulse in STO has been calibrated by measuring the maximum expansion of the LSMO film after 6 ps using ultrafast x-ray diffraction with 200 fs time resolution [Boj12a] and deducing the strain in the STO via the ratio of the sound velocities [Bel63, Ren07, Boj12a]. For low excitation levels (lower curve), the signal is modulated by the phonon frequency observed via backscattering, as given by equation 2.8. For high excitation level (upper curve), a beating frequency is observed that can be explained according to equation 3.3: due to the high amplitude of the strain wave, the anharmonicity of the interatomic potential can no longer be neglected: the leading compressive strain front of the bipolar strain pulse travels

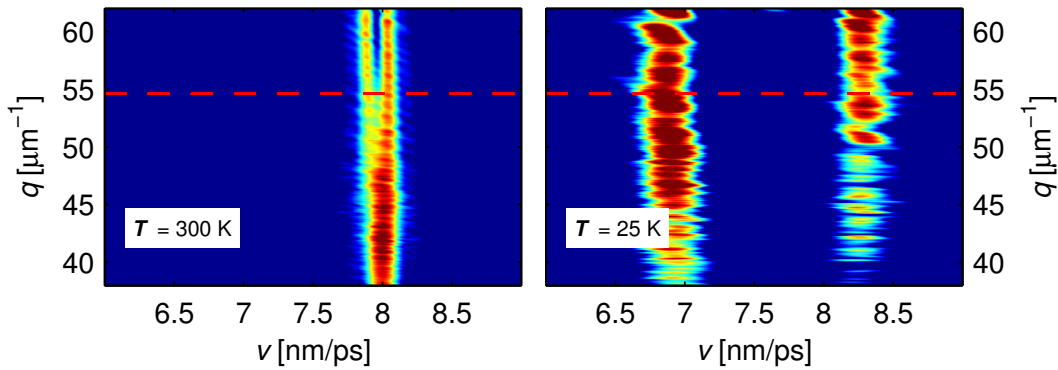


Figure 5.4: Calculated sound velocity for sample L37 for all measured phonon wavevectors at two different temperatures and 60 mJ/cm² excitation fluence. The plot has been obtained by Fourier-transforming the time dependent data and calculating the sound velocity from the oscillation frequency according to equation 2.8. The time dependent data was smoothed over 2 nm and 5 ps. The colourcode denotes the amplitude of the corresponding sound velocity [a.u.] as explained in the text. Further evaluation is performed for $q = 54.6 \mu\text{m}^{-1}$ indicated here as red dashed line.

faster than the trailing tensile strain front. Both sound velocities are detected in our experiment. A detailed analysis of this effect at room temperature can be found in [Boj12a].

5.3 Nonlinear Effects II: Coupling to Domain Walls

In the lower panel of figure 5.3, we show the same measurement as shown in the upper panel performed in the antiferrodistortive phase at $T = 25$ K. For small strain amplitudes, the temporal traces are similar to the ones recorded at room temperature. In the case of high excitation level, however, the beating frequency is much higher at low temperature. Additionally, the oscillations are damped out faster than at room temperature.

Instead of performing a fit with two damped cosine functions, we now perform a temporal Fourier transform for all wavelengths of the time dependent curves and compute the sound velocity from the determined frequencies according to equation 2.8. The small temperature dependence of the refractive index [Rös13] is hereby neglected. Thus obtained 'sound velocity distributions' are shown for two temperatures in figure 5.4 and reflect the fact that there is more than one sound velocity detected in the measurements. We find two peaks of the sound velocity distribution for most wavevectors. At room temperature we only observe one single peak for lower wavevectors for the following reason: the difference in sound velocities for the compressive and tensile strain fronts amounts to approximately 0.15 nm/ps. According to the linear phonon dispersion we can calculate a beating frequency of $\Delta\nu = \Delta v q / 2\pi \approx 0.9$ GHz for $q = 40 \mu\text{m}^{-1}$, yielding a beating period of about 1.1 ns for this wavelength. Within this interval the phonons are damped, compare the

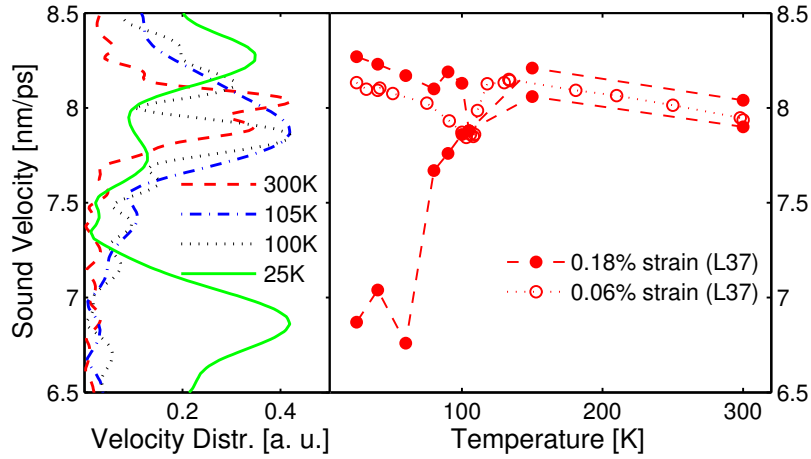


Figure 5.5: Left: sound velocity distribution extracted from the Fourier transform of the transient reflectivity data shown in figure 5.3, for 0.18 % strain amplitude in STO at selected temperatures generated by excitation of an LSMO transducer (sample L37). Right: extracted maxima from the sound velocity distribution as a function of temperature, for high and low strain amplitudes.

temporal trace shown in figure 5.1.

The left panel of figure 5.5 shows the sound velocity distribution for high excitation level at 4 different temperatures computed from the the signal at $\lambda = 528$ nm ($\nu \approx 70$ GHz, $q = 54.6 \mu\text{m}^{-1}$). Directly at the phase transition the phonon attenuation increases, leading to a broader Fourier peak. Therefore, at $T = 105$ K we solely observe one broad peak in the sound velocity distribution. The observed damping of the phonon modes will be discussed in detail in the next chapter. The right panel of figure 5.5 collects the maxima of the sound velocity distributions for high excitation level, shown as full red circles, as a function of temperature in comparison to the results for low excitation level, shown as open red circles, that have already been shown in figure 5.2. In the nonlinear regime and at temperatures above T_a , the observed splitting is symmetric, and can be explained by the anharmonicity of the interatomic potential, as discussed in the previous section. Below T_a , a giant reduction of the sound velocity is observed that exceeds the symmetric splitting and cannot be explained by anharmonicity alone [Hac10, Vis94]: third order anharmonicity can only account for changes in sound velocity that are linear in strain and thus leads to a splitting in sound velocity that is symmetric around zero strain [Boj12a]. In order to explain the asymmetry in the splitting as observed, a potential with a significant contribution of at least fourth order would be necessary. Theoretical calculations of the second and third order elastic constants show that the third order term exhibits an anomaly directly at the phase transition, similar to the second order term. There is, however, no evidence for a change between high and low temperature phases further away from the transition [Vis94]. Calculations studying the pressure dependence of the elastic constants [Hac10] only find a small change in the third order anharmonicity between the cubic and the tetragonal phases: the dependence

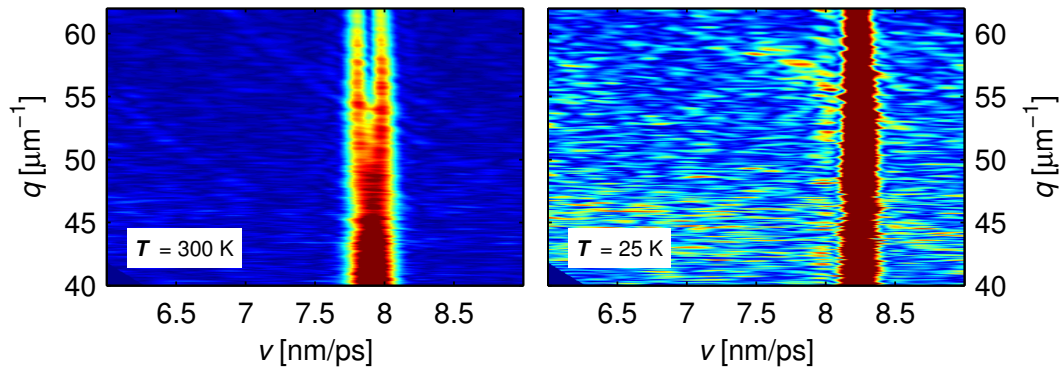


Figure 5.6: Calculated sound velocity for sample S15 for all measured phonon wavevectors measured at two different temperatures and an excitation fluence of 60 mJ/cm². The colourcode denotes the amplitude of the corresponding sound velocity as explained in the text. Colour code: velocity distribution [a.u.].

of the elastic constants on pressure is linear in both phases, i.e. there is no sign of a fourth order contribution. The difference in gradient between the phases, i.e. the difference in magnitude of the third order contribution between the phases, is small. These calculations show no evidence for an anisotropy of the higher order elastic constants that might explain the observed sound velocity splitting.

The reduction in sound velocity found here, is comparable to the superelastic softening of the elastic constants in STO, which has so far only been found for lower frequency phonons in the Hz to MHz regime and is attributed to the coupling of phonons to domain walls [Fos72, Kit00, Sco12, Sch11, Sch12b]. The effect was thought to be impossible for high frequencies [Sch11, Sch12b, Kit00]. It is accompanied by an increased damping, which is observed for the low temperature high strain data in figure 5.3. The scattering of the data at low T in figures 5.5 and 5.2 might be due to additional phase transitions discussed in the literature [Lyt64, Kit00, Sco12]. We will come back to this feature in the next chapter.

5.3.1 Suppression of Domain Formation

We support our interpretation that the giant softening for large amplitude GHz strain waves originates from the coupling to domain walls by repeating the experiments for similar samples with different epitaxial strain conditions: we used STO samples with 15 nm and 70 nm thick SRO transducer films (S15 and S70) and 20, 37 and 90 nm thick LSMO films (L20, L37, L100). While LSMO has a slightly smaller lattice constant in bulk of $a_{\text{LSMO}} = 3.876 \text{ \AA}$ [Mar96] than STO, with $a_{\text{STO}} = 3.905 \text{ \AA}$ [Eom92], SRO has slightly larger bulk lattice constant, $a_{\text{SRO}} = 3.93 \text{ \AA}$ [Eom92]. Hence, SRO transducers lead to tensile strain at the interface. This supports the alignment of the elongated c -axis parallel to the interface. It suppresses the formation of domains with the elongated tetragonal c -axis parallel to the direction of the strain pulse traveling perpendicular to the surface in a similar way as observed for static external stress [Fos72, Kit00, Cha70]. Estimating the size of this effect, we find that

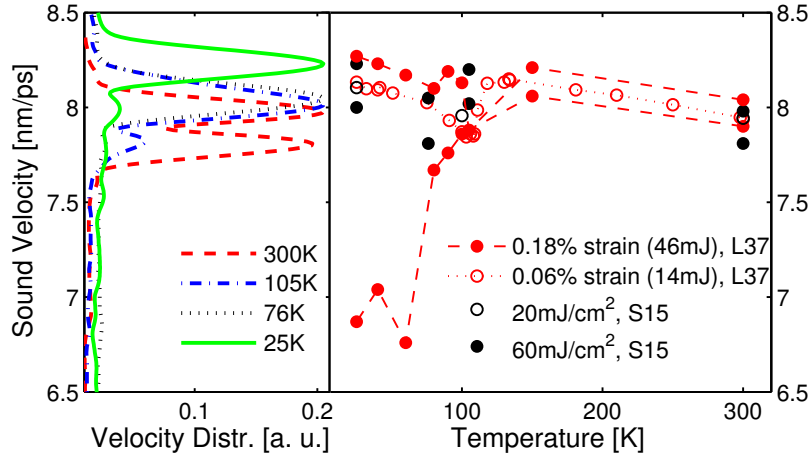


Figure 5.7: Left: sound velocity distribution for different temperatures for the sample S15 averaged for $q = 50 - 57 \mu\text{m}^{-1}$. Right: extracted sound velocities as in figure 5.5 with the values measured for S15 included as black circles. Open circles again denote low excitation and full circles denote high excitation level.

the lattice mismatch between SRO and STO amounts to $6 \cdot 10^{-3}$. A uniaxial pressure of 1 MPa, on the other hand, which reduces the superelastic effect by several tens of percent [Kit00], corresponds at room temperature [Bel63] to an induced strain of $3 \cdot 10^{-6}$ and is hence orders of magnitude smaller than the lattice mismatch in our experiment. Therefore, the strain at the interface is sufficient to expect an in-plane alignment of the c -axis.

In contrast, x-ray diffraction measurements on STO with a thin $\text{YBa}_2\text{Cu}_3\text{O}_7$ top layer suggest that a transducer with a smaller lattice constant, similar to LSMO, leads to mixed domains with the c -axis aligned either parallel or perpendicular to the surface within the first micrometers of the STO substrate [Loe10].

In figure 5.6 we present the extracted sound velocity distributions for two different temperatures measured for a sample with a 15 nm SRO transducer (sample S15) for high excitation level. The excitation fluence for these measurements was chosen such that the difference in detected sound velocities at room temperature is in agreement with the one obtained for high excitation level for sample L37. We thus expect that the difference in leading and trailing strain amplitude is the same as in the measurements for L37 and should therefore amount to approximately 0.18 %. At low temperature we observe a dominant peak around $v = 8.2 \text{ nm/ps}$ and a small contribution to the sound velocity just below $v = 8 \text{ nm/ps}$. We have no concise explanation, why the peak at lower sound velocity shows such low intensity (compare also simulations and measurements in [Boj12a]).

In the left panel of figure 5.7, we display the extracted sound velocity distribution for S15 obtained at high excitation level and four different temperatures for $q = 54, 6 \mu\text{m}^{-1}$. In the right panel we compare the extracted sound velocities for the four temperatures, shown as black full circles with the results for low excitation level, shown as black open circles, in comparison to the previous results for L37, shown

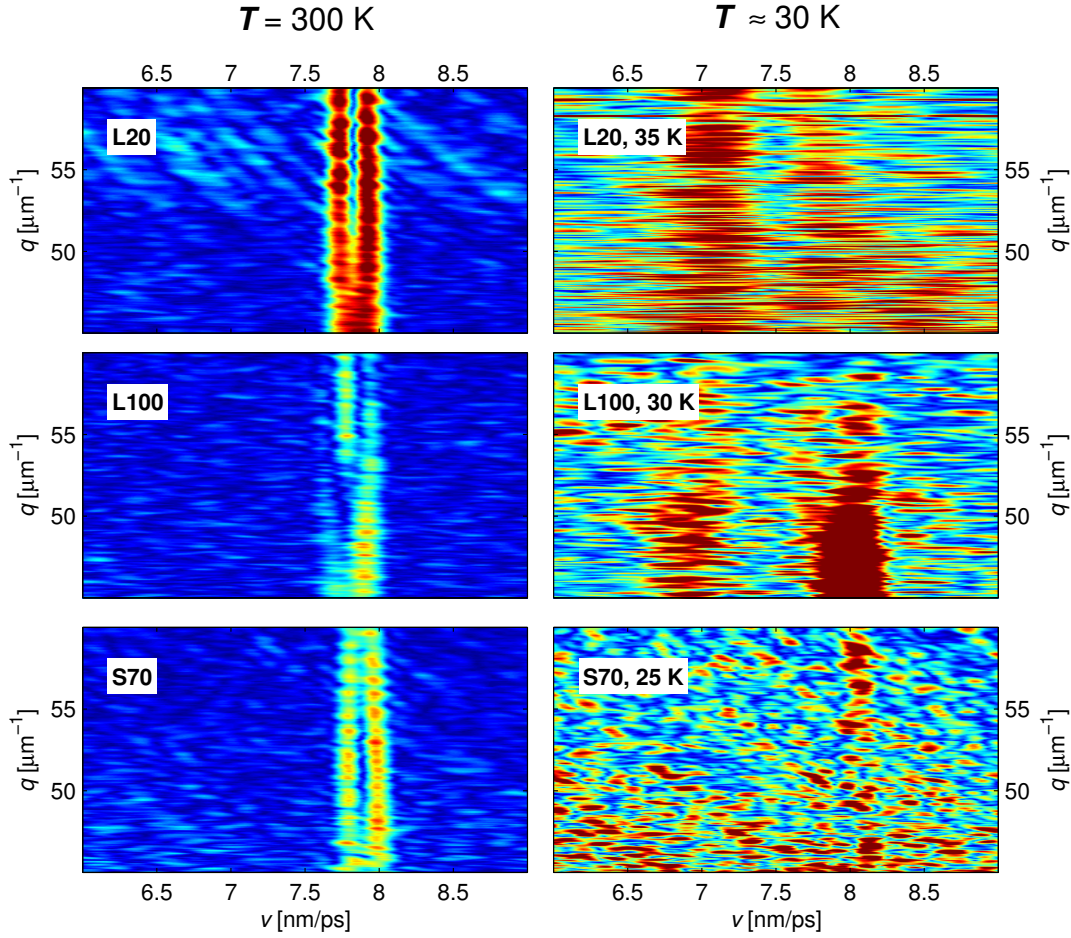


Figure 5.8: Extracted sound velocity for all measured wavevectors in the sample. Measurements were performed on samples L20, L100 and S70 with an excitation fluence of 55, 46 and 20 mJ/cm², respectively, and the strain should amount to approximately 0.18%. On the left side we display measurements for room temperature, on the right side for low temperature around $T = 30$ K. Colour code: velocity distribution [a.u.].

again as red circles. For large strain amplitudes the data obtained from S15 are in accord with the results for L37 only for temperatures above T_a . Below T_a , the sound velocity exhibits a small splitting with respect to the value observed for low excitation, similar to the one observed above T_a .

In figure 5.8 we present data recorded for the samples L20, L100 and S70 at room temperature and at approximately 30 K in the antiferrodistortive phase. Again, the excitation fluence was chosen such that the difference in detected sound velocities at 300 K was equal to the difference detected for L37. The general trend is confirmed: at low temperatures, there is a significant peak in the sound velocity distribution around 7 nm/ps for samples with LSMO transducers, while for the sample with the SRO transducer we do not observe this peak. The experiments with SRO transducers suggest that the alignment of the c -axis relative to the sample surface removes the

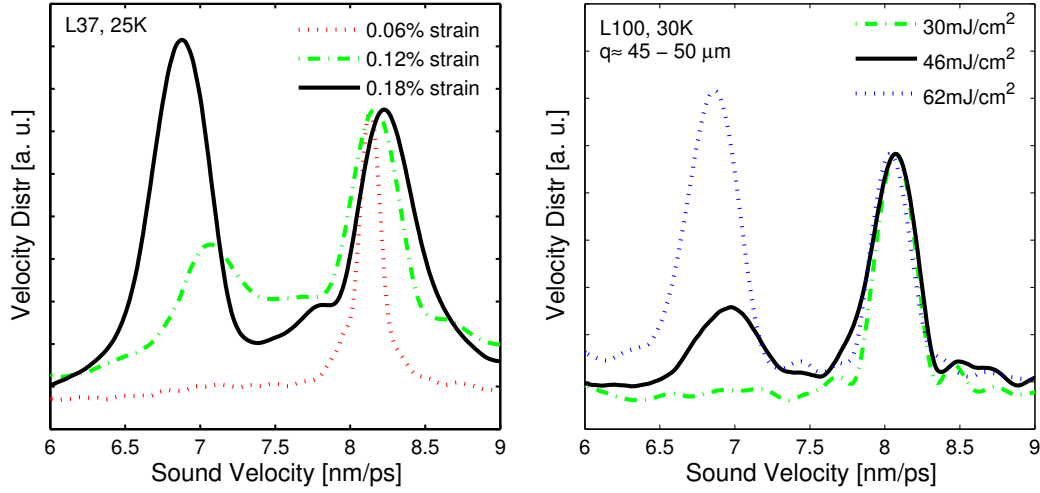


Figure 5.9: Fluence dependence of the coupling of strain to domain walls. Left: Measurements on sample L37 at 25 K. An average over all wavevectors was performed to obtain the plot. Right: Measurements on sample L100 at 30 K. Due to the high noise level in the measurements, compare figure 5.8, the evaluation has been performed only at $q \approx 45 - 50 \mu\text{m}$.

coupling of large amplitude GHz strain to the domain walls.

5.3.2 Fluence Dependence of the Coupling

In figure 5.9 we display the distribution of sound velocities extracted from the time domain Brillouin scattering experiments at low temperatures for three different excitation levels. The left panel displays data for sample L37 and the right panel data for sample L100 that is of much lower quality but shows the same trend: for L37, we observe that the peak at higher sound velocities shifts linearly with increasing strain towards higher values, as would be expected for an elastic potential with significant contribution of third order [Boj12a]. The peak at lower sound velocities does not show a continuous shift with increasing fluence as would be the effect of an anharmonic potential. It emerges only at high strain levels and its weight increases when the strain is increased. This observation is supported by the data for sample L100 in the right panel, although this data shows a lower signal to noise level. This effect cannot be explained by taking only an anharmonic lattice potential into account and supports our interpretation that the coupling to domain walls induces the observed giant softening of the GHz acoustic phonons for samples with LSMO transducer.

5.3.3 Microscopic Picture of Ultrafast Strain Induced Domain Wall Motion

In figure 5.10 a schematic representation of a domain wall in STO on the basis of recent literature [Hon13, Kal13] is shown. In the wall, dislocations as the one displayed in the centre of each panel, may appear. These are called 'kinks' in the

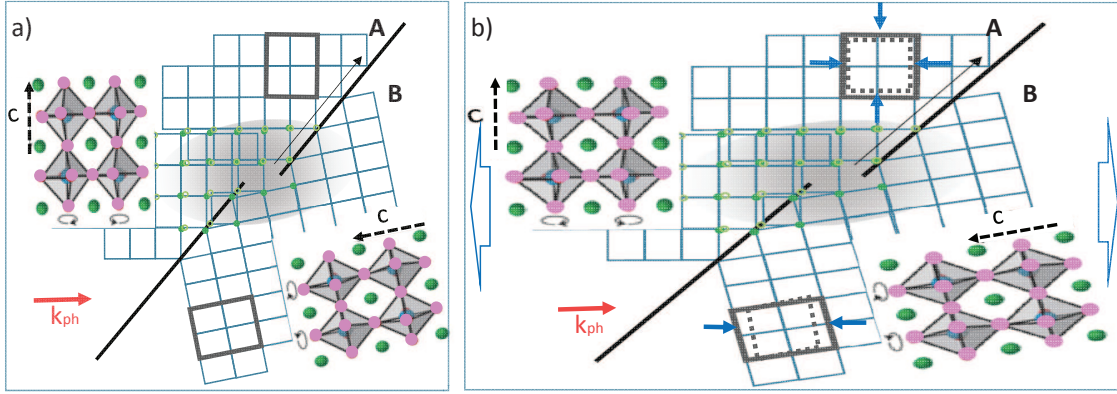


Figure 5.10: a) Schematic of the STO crystal in the tetragonal phase near a kink in a domain wall according to literature [Kal13, Hon13, Sal11a, Sal13b]. Tetragonal distortion and twinning angle are exaggerated. The gray shaded area highlights the strain field near the kink. (a) Black line: domain wall with kink. Grey rectangles: unit cell of tetragonal phase. Details of this unit cells are shown with oxygen octahedra as enlarged insets. For slow vertical expansion the kink would move along the black arrow. (b) Snapshot for ultrafast uniaxial expansive strain along \mathbf{k}_{ph} (red arrow) with amplitude exceeding the original tetragonal distortion. No contraction perpendicular to \mathbf{k}_{ph} can occur for this timescale. Blue arrows: compressive forces that counteract the external uniaxial expansion. For a detailed discussion see main text.

literature.

The gray shaded region visualises the strain field in the crystal in the vicinity of a kink in the domain wall as observed in simulations [Sal11a, Sal13b]. In the following we call the region, where the long c -axis is perpendicular to \mathbf{k}_{ph} , on the upper left side of the domain wall 'A'. The region on the lower right with the c -axis oriented along \mathbf{k}_{ph} is addressed as 'B'. For a slow and small expansion of the crystal the domain wall travels by moving the kink parallel to the wall along the thin black arrow [Sal11a, Kit00]. This increases the size of domains with the c -axis along \mathbf{k}_{ph} and decreases region A. In total, the crystal is expanded more along \mathbf{k}_{ph} than without domain wall motion. The crystal appears to be softer, i.e. it has a reduced sound velocity. This process requires a contraction of the crystal perpendicular to the applied stress by the Poisson effect and additionally due to the decreasing number of unit cells with the long c -axis perpendicular to the stress. For a homogeneous expansion over the diameter $d_L = 100\mu\text{m}$, given by the laser excited area, the in-plane contraction would take place on a timescale exceeding $\tau \approx d_L/v_s \approx 12\text{ ns}$, determined by the time it takes to relax the strain at the sound velocity v_s . This restricts the superelastic regime to the 80 MHz range on a $100\mu\text{m}$ length scale. For GHz phonons or picosecond strain pulses in the linear regime, domain wall motion is fully suppressed [Sch11, Sch12b], as is seen in the measurements for low strain amplitude in figures 5.5 and 5.7.

In the nonlinear regime, we propose the following mechanism: the transducer with thickness d generates strain waves with wavevector \mathbf{k}_{ph} perpendicular to the

sample surface. The fundamental wavelength $\lambda_{\text{ph}} = 2\pi/k_{\text{ph}} \leq 2d$ of the strain wave is limited by the thickness d or the optical penetration depth ξ of the exciting light in the transducer. The strain fronts are plane waves since for the spot size of the exciting laser light holds $d_L = 100 \mu\text{m} \gg d$. We first discuss the effect on domain wall motion induced by the expansive part of the bipolar strain pulse. Strain with an amplitude of 0.18 % much larger than the tetragonal distortion [Lyt64, Uno67] ($[c - a]/a = 5 \cdot 10^{-4}$) leads to expanded tetragonal unit cells in region A with the longer unit cell axis now parallel to \mathbf{k}_{ph} , as schematically shown by the solid grey rectangle in figure 5.10(b). The memory of the original c -axis orientation is rapidly lost since the thermal oxygen octahedra-tilt motion is fast compared to the duration of the passing strain pulse [Koh06]. These expanded unit cells in A want to contract in all three dimensions in order to recover their original volume, which is indicated by the dotted grey rectangle. Within the domains all stresses are balanced by adjacent unit cells. In region B the unit cells feel compressive stress (blue arrows) only along \mathbf{k}_{ph} . Thus, at the domain wall the stress perpendicular to \mathbf{k}_{ph} is unbalanced and leads to a motion of the domain wall and the connected strain fields such that region B increases. The reverse effect would be expected for the compressive part of the strain pulse. However, since space is required for the atoms at the domain boundary to rearrange, the coupling is mainly observed for tensile strain.

As follows from the discussion above, complex microscopic dynamics are involved. The moving domain walls do not separate domains in their equilibrium structure, but rather domains of the crystal with tetragonal non-equilibrium strain. The increased damping of the sound wave and the superelastic effect are intimately connected to propagation of non-equilibrium strain fields around kinks in the domain walls. The importance of lattice inhomogeneities for the propagation of strain waves is emphasised in related experiments: in ferroelectric $\text{Pb}(\text{Zr}_{0.2}\text{Ti}_{0.8})\text{O}_3$ we have observed by time resolved x-ray diffraction that the sign, amplitude and frequency of the strain pulses alter the interaction with domain boundaries and dislocations [Sch13a]. Similar dependences on the frequency and amplitude of the applied strains are reported for the velocity of ferroelastic [Har04] and ferroelectric [Lis09] domain wall motion.

The considerable additional softening at 70 GHz indicates that the domain walls propagate a substantial fraction of the domain size $D \approx 100 \text{ nm}$ [Chr98] within a half period τ of the sound wave. Therefore the domain wall velocity must be on the order of the sound velocity. Computer simulations on the terahertz timescale have indicated kink-propagation velocities exceeding the sound velocity [Sal13b]. Our 12% reduction in sound velocity for 70 GHz large amplitude strain compares to a 50% reduction of Young's modulus measured at 10 Hz [Kit00], i.e. we observe about half the softening effect.

6. Attenuation of Phonons in SrTiO₃

In this chapter we discuss the damping of coherently excited longitudinal acoustic phonons in STO determined at different temperatures. We present high amplitude single pulse excitation and lower amplitude pulse train excitation experiments, compare the results to the literature and to results obtained by a collaborating group using frequency domain Brillouin scattering. We discuss the attenuation mechanisms involved for the different temperature regimes with a particular focus on the attenuation at and below the phase transition. Table 6.1 gives an overview over the samples discussed and the experimental techniques applied.

6.1 Observed Damping by Time Resolved Brillouin Scattering

6.1.1 Single Pulse Excitation

In figure 6.1 we display the temperature dependent damping rate extracted from fits as shown in figure 5.1 in the previous chapter. Approaching the phase transition from above, the damping increases steeply by a factor of approximately five within 10 K of the phase transition. On the low temperature side of the transition, the

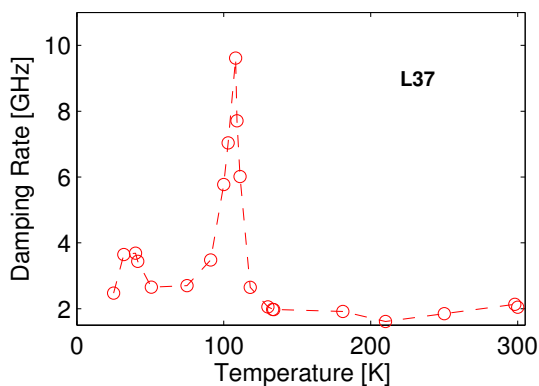


Figure 6.1: Temperature dependent damping rate $\Gamma = 1/\tau$ for the time resolved measurements performed for 14 mJ/cm² excitation fluence and single pulse excitation, evaluated for $\lambda = 528$ nm, $q = 54.6 \mu\text{m}^{-1}$ averaged over approximately $\Delta\lambda = 2.5$ nm. The averaging does not affect the evaluated attenuation rates, as estimated in section 3.1.5 above.

Table 6.1: Types of measurements performed and list of samples used in the measurements. The samples are labelled according to the transducer material and the thickness of the transducer layer following the labels assigned in table 5.1. For the pulse train excitation the integral fluence is set to 20 mJ/cm², yielding a fluence per pulse of 20/8 mJ/cm² = 2.5 mJ/cm².

measurement technique	samples used
single pulse, 14 mJ/cm ²	L37, S15
pulse train excitation, 20/8 mJ/cm ²	L37, S15
frequency domain	S15, bare STO (100)

damping falls off close towards the room temperature value within about 15 K. This decrease is more gentle than the rise. At low temperatures, around $T = 35$ K another small increase of the damping rate is observed.

6.1.2 Excitation with a Train of Pump Pulses

Since the anharmonicity of the interatomic potential enables the coupling of different phonon modes, as explained in section 2.3.5, high excitation levels lead to more coherent and incoherent scattering effects and thus to an increased damping of the excited mode. This was proven in measurements discussed in [Her12b]. In order to quantify the influence of the lattice anharmonicity, we performed measurements with a train of excitation pulses. This way, we obtain a high occupation of the selected mode while the amplitude of each strain pulse is very low. We expect that the damping rate at room temperature decreases in comparison to the single pulse measurements. The influence of the lattice anharmonicity at the phase transition and at lower temperatures is hereby also studied.

We use a train of eight equally spaced pump pulses, excited with an overall fluence comparable to the fluence in the single pulse measurements discussed above. The occupation of the selected mode is thus kept high and a good signal to noise ratio for this mode is obtained, as explained in section 2.3.3. The fluence per pulse was thus about an eighth of the fluence in the single pulse measurements, leading to smaller strain per pulse and a reduction of the effect caused by the anharmonicity of the coupling potential. Each pulse had a length of approximately 7 ps and the pulse spacing was around 15 ps. The length of the pulses leads to a suppression of higher frequencies and thus to a sine-like excitation. A small frequency window around $q = 52 \mu\text{m}^{-1}$ is highly populated while other excited modes interfere destructively, as discussed in section 2.3.3. The length of the excitation pulses suppresses the generation of higher harmonics. For these measurements, the sample was pumped and probed from the backside. This way, the attenuation of the probe light that twice traverses the transducer when probing from the front side, is avoided. The reflection originating from the backside to air interface was blocked, which minimises the constant background in the detector. The relative change in reflectivity thus obtained amounts to 100% or more and the time dependent normalisation of the phonon oscillation amplitude discussed in 3.1.6 is performed in order to obtain the correct time dependent amplitude of the oscillations.

In figure 6.2 we display the obtained damping rates in STO for a sample with LSMO transducer (L37) in the left panel and for a sample with SRO transducer (S15) in the right panel. The results were in this case obtained by calculating windowed Fourier transforms for short time intervals, integrating over the spectrum of the excited pulse and fitting a damped exponential to the obtained time dependent data points.

At the phase transition, the results resemble the ones shown in figure 6.1, displayed in the left panel as open red circles. At room temperature the damping rate for the single pulse measurement is higher than for the multipulse measurement, while below

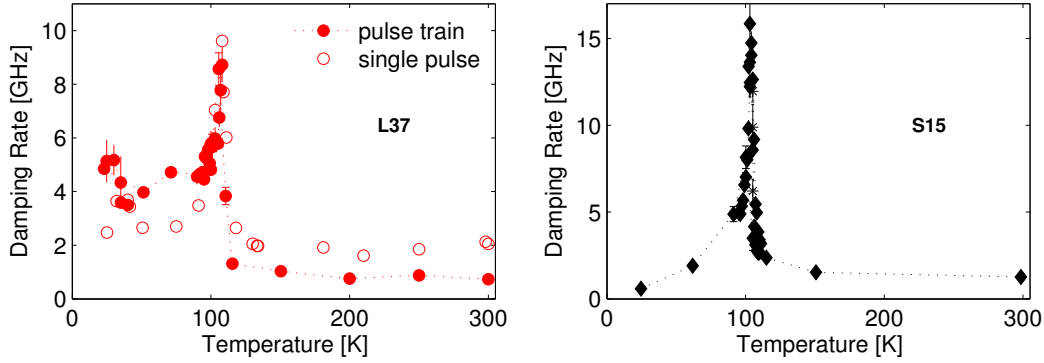


Figure 6.2: Temperature dependence of the evaluated damping in SrTiO_3 measured with multipulse excitation for $q \approx 52 \text{ nm}^{-1}$. Errorbars are given by the uncertainty of the fits. Integral excitation fluence $F_{\text{tot}} \approx 20 \text{ mJ/cm}^2$. Left: measurements performed on the sample with 37 nm LSMO transducer (L37), full red circles in comparison with results obtained by the single pulse measurements, open red circles. Right: measurements performed on a sample with 15 nm SRO transducer (S15).

the phase transition it is lower for the single pulse measurement. The maximum damping rate, which is observed directly at the phase transition, is higher for sample S15 than for sample S37. However, for the measurements on sample L37, there are less datapoints on the high temperature side, which makes the exact localisation of the phase transition temperature and thus the estimation of the maximum damping rate difficult.

6.1.3 Results from the Literature

Only recently, the first measurement of attenuation for longitudinal acoustic phonons in the GHz range was published by Nagakubo *et al.* [Nag12]. The results are displayed in figure 6.3 as full blue triangle. In these measurements, a 17 nm thick platinum film was deposited on the STO (100) surface as transducer. The measurements were performed with 800 nm pump light of approximately $16 \mu\text{J/cm}^2$ excitation fluence at 80 MHz repetition rate. The probing was performed at $\lambda = 400 \text{ nm}$ under normal incidence. These measurements were performed with a non-amplified femtosecond laser pulse. This means that the excitation fluence was about 3 orders of magnitude smaller than in our measurements, but the repetition rate was more than 4 orders of magnitude higher. Therefore, the signal to noise ratio was comparable to our experiment, but the effect of the anharmonic phonon phonon coupling is largely suppressed. The attenuation given in the article in $1/\text{cm}$ is multiplied by the approximate sound velocity in order to obtain the damping rate Γ , which is plotted in the figure. For a comparison with our data measured at $q = 52 \mu\text{m}^{-1}$, the results are scaled down by a factor of $(q/q_{\text{Lit}})^2 = (52/80)^2$, according to the Akhiezer model, which has been introduced in section 2.3.6, where $\Gamma(q) \propto q^2$. The validity of this theory is discussed in section 6.3 below. The scaled damping rates, which can now be compared to our measured values, are displayed in the figures as open blue trian-

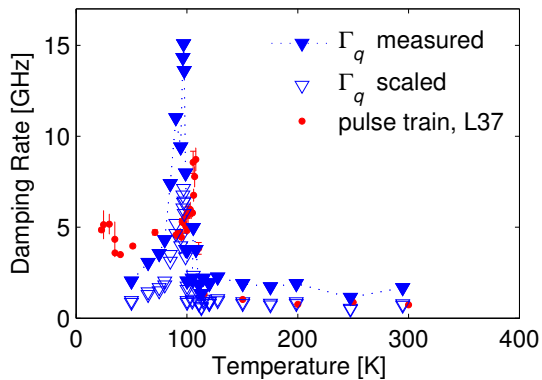


Figure 6.3: Temperature dependent damping rate $\Gamma = 1/\tau$ for the time resolved measurements performed for $16 \mu\text{J}/\text{cm}^2$ excitation fluence, evaluated for $\lambda = 400 \text{ nm}$, $q \approx 80 \mu\text{m}^{-1}$, shown as full triangles [Nag12]. The results were scaled with $(q/q_{\text{Lit}})^2$ for a direct comparison with our pulse train measurements on L37 from figure 6.2, shown as red circles.

gles. Also shown are the pulse train excitation results measured on sample L37 for comparison. At room temperature the measured damping rates agree, at and below the phase transition, our measurements yield a higher attenuation.

6.2 Frequency Resolved Brillouin Scattering

Our hypothesis that the damping rate of the highly excited coherent modes depends on excitation level, lead to the comparison of our data with results obtained in the frequency domain. We here display unpublished results from A. Koreeda measured by frequency resolved Brillouin scattering on sample S15 and on a bare STO sample [Kor14a]. In contrast to our experiments, where the decay rate of highly excited coherent modes is detected, these measurements yield the linewidth and thus the damping rate of thermally excited phonons.

A high resolution, offset-stabilised tandem Fabry-Pérot interferometer [Kor11] was used to resolve the small frequency shift in the scattered light. The resolution of the instrument given as instrumental half width was 0.27 GHz. Probe light of $\lambda = 532 \text{ nm}$ was detected under an angle of $180^\circ \pm 2^\circ$, yielding a wavevector of the observed phonons of $58 \mu\text{m}^{-1}$. In the evaluation a Fano function [Fan61] was fitted to the data to account for a slight asymmetry in the line shape:¹

$$f_{A,b,\nu_q,\Gamma,C}(\nu) = A \frac{(b + \frac{\nu - \nu_q}{\Gamma})^2}{1 + (\frac{\nu - \nu_q}{\Gamma})^2} + C, \quad (6.1)$$

with amplitude A , asymmetry parameter b that goes to zero for a symmetric curve, central frequency ν_q , width Γ and constant offset C . The Fano function was convoluted with the resolution function to account for the finite resolution of the setup. Γ corresponds to the half width at half maximum of a Lorentzian curve. Since this curve is fitted as a function of frequency, rather than angular frequency, the extracted value is multiplied by a factor of 2π to yield a result equivalent to the damping rate $1/\tau$ from the time resolved data, as derived in section 2.3.6. The results for sample

¹The asymmetry stems from an interference with the quasielastic central peak [Kor06], a phenomenon that we do not discuss here.

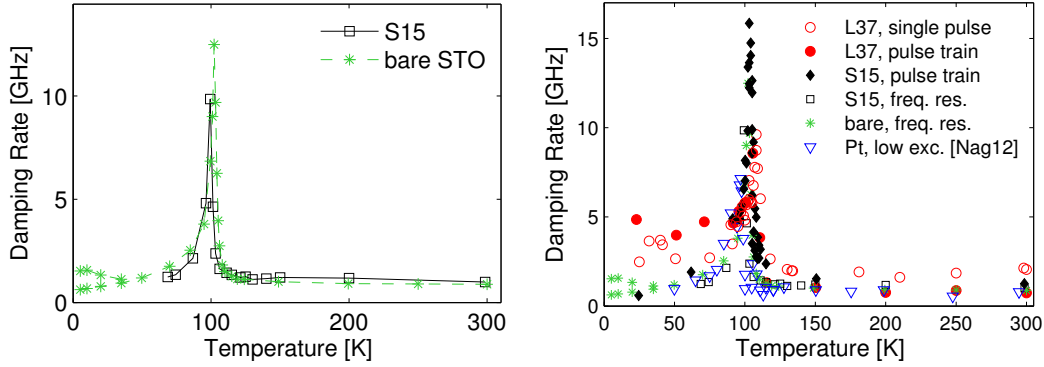


Figure 6.4: Left: temperature dependent damping rate $\Gamma = 1/\tau$ for frequency resolved measurements performed for $\lambda = 532$ nm, $q = 58\mu\text{m}^{-1}$ on sample S15 (open black squares), and on a bare STO sample (green asterisks). Right: comparison with time resolved measurements from figures 6.1, 6.2 and 6.3.

S15 are shown in the left panel of figure 6.4 as black open squares. Furthermore, we display frequency resolved measurements performed on a bare sample for comparison, shown as green asterisks in the left panel of figure 6.4. For both samples, the results are in good agreement. The bare sample was measured down to lower temperatures and a splitting of the Brillouin peak was observed around 40 K. These two peaks exhibit slightly different widths, leading to two different damping rates for each temperature in this low temperature region. In the right panel we compare the damping rates obtained for the frequency resolved data with the results obtained by time domain scattering and the results from the literature [Nag12].

The measured damping rates agree for sample S15, the platinum covered sample from the literature and the bare sample. However, below the phase transition the measurements on L37 show higher damping rates than found for all other samples. Directly at $T_a \approx 105$ K, the measured damping rates are different for each measurement. The highest attenuation is found for time resolved pulse train excitation on sample S15.

6.3 Interpretation of Measured Damping Rates

Above, we showed results for the ultrasonic attenuation of GHz phonons measured by time resolved as well as frequency resolved phonon light scattering. The obtained damping rates agree qualitatively: they display a steep increase of attenuation at the phase transition. This increase of attenuation is notably steeper above than below the phase transition. There are, however, differences in the results that depend on the transducer material, excitation fluence and measurement technique. The transducer material influences the domain configuration at the surface, as discussed in the previous chapter. High fluence, single pulse excitation yields a higher damping rate at room temperature than low fluence single pulse or pulse train excitation measurements. Finally, the measurement technique determines, whether the phonons

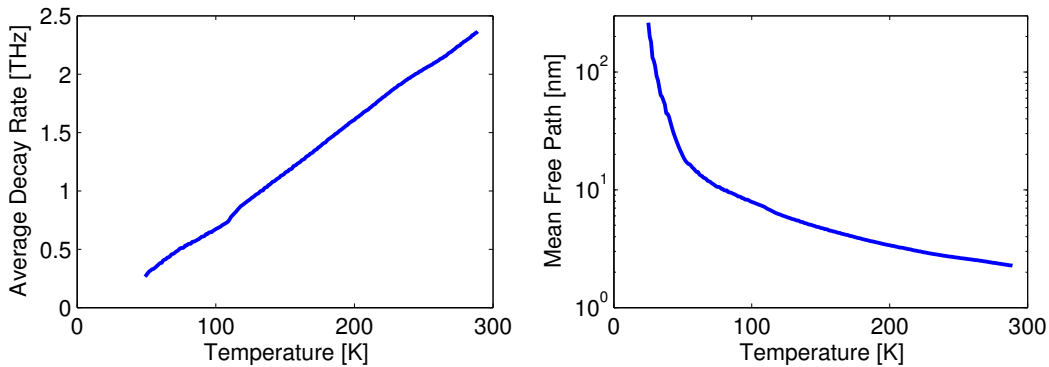


Figure 6.5: Decay rate $\bar{\tau}^{-1}$ of thermal phonons and mean free path \bar{l} estimated according to the relation $\kappa = \frac{1}{3}C_V v_D^2 \bar{\tau}$ and literature values as cited in the main text.

are observed in the bulk or close to the surface: for the time resolved measurements, phonons are generated by a transducer at the sample surface. In our measurements they are damped out within approximately 1 ns at room temperature and within about 100 ps at the phase transition. With the sound velocity of STO of $v \approx 8$ nm/ps (as measured in chapter 5), we estimate a propagation distance of less than 10 μm at room temperature and less than 1 μm at the phase transition. The frequency resolved technique, on the other hand, probes the thermal population of incoherent phonons. Since the absorption of optical light in bulk STO is negligible below the direct bandgap of 3.75 eV [vBe01], phonons across the whole depth of the sample contribute to the scattering signal. Thus, the comparison of the results obtained by these two techniques allows us to compare the different sound attenuation properties of the bulk and the surface of the samples.

For the discussion of the attenuation mechanisms relevant at the different temperature regimes, we first determine the relevant phonon phonon scattering regime. For the Akhiezer mechanism (introduced in section 2.3.6) to be valid, the condition $\omega_q \ll \bar{\tau}^{-1}$ needs to be fulfilled, where ω_q is the frequency of the observed phonon mode and $\bar{\tau}$ is the average lifetime of a thermal phonons. We estimate the parameters $\bar{\tau}$ and the mean free path \bar{l} from literature values. These are calculated from the macroscopic thermal properties of the material using $\kappa = \frac{1}{3}C_V v_D^2 \bar{\tau}$ (equation 2.17 in section 2.3.6 on sound attenuation). We use the thermal conductivity from Suemune [Sue65], the molar heat capacity measured by Durán *et al.* [Dur08], the unit cell volume according to Loetzsch *et al.* [Loe10] and the Debye velocity using values measured by Bell and Rupprecht [Bel63]. The estimated values are displayed in figure 6.5. We find an average decay rate of thermal phonons in STO of about $\bar{\tau}^{-1} \approx 2.5$ THz at room temperature. The macroscopic parameters vary smoothly across the phase transition and we find $\bar{\tau}^{-1} \approx 300$ GHz at 50 K. Below 50 K the values for C_V are not precise enough to yield a reliable estimation. Thus, for the phonons investigated in this work with frequencies of about 50 to 80 GHz, the Akhiezer formalism explained in section 2.21 describes the attenuation due to phonon phonon scattering across the whole temperature range.

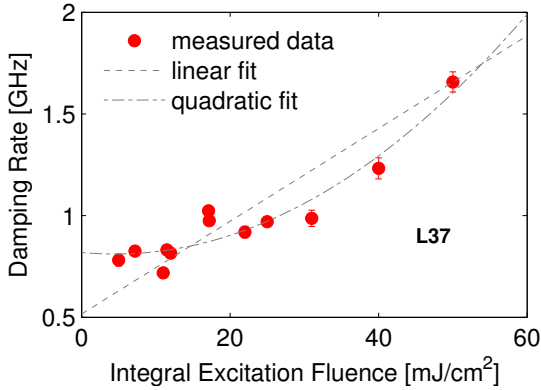


Figure 6.6: Fluence dependence of the extracted damping rate for pulse train excitation. From the linear and second order polynomial degression we find a zero fluence damping rate of approximately 0.82 GHz and 0.52 GHz, respectively, corresponding to decay times of 1.2 and 1.9 ns, respectively.

6.3.1 Damping at Room Temperature

For high temperatures the measurements performed with a train of exciting pump pulses exhibit a lower damping rate than found for the single pulse excitation measurements presented in figure 6.1. This is caused by the anharmonicity of the interatomic potential that plays an increasing role with increasing excitation level, as explained in section 2.3.5. This has been proven in a fluence dependent series of measurements, as shown in figure 6.6: decreasing the integrated excitation fluence in the pulse train excitation measurements, the damping rate decreases. The extrapolation to zero excitation fluence suggests a decay time τ between 1.2 and 1.9 ns, dependent on the fitting function.

According to the Akhiezer model, the damping rate is given by

$$\Gamma = \frac{\gamma^2 C_V T \bar{\tau} \omega_q^2}{3\rho v^2} = \frac{3\alpha_{\text{th}}^2 B T \bar{\tau} \omega_q^2}{C_V}, \quad (6.2)$$

and has been introduced in section 2.3.6. Using the values above and the linear thermal expansion α and bulk modulus B extracted from deLigny and Richet [deL96] and Fischer *et al.* [Fis93], respectively, the damping rate is estimated. In figure 6.7 we compare the results with the estimated theoretical curve, shown as grey dashed line, results for MHz phonons from the literature [Nav69] and time resolved measurements that have been performed using x-ray diffraction [Her12b, Sha13]. The experimental results agree nicely with the estimations across the whole wavevector range. Thus we conclude that the Akhiezer model is indeed valid to describe the phonon attenuation at room temperature. In particular, we find that ultrasound or hypersound measurements yield the same attenuation rate as measurements that sample the thermal population of phonons.

Deviations in the determined scattering rates that cannot be explained by the excitation amplitude, for example the low damping rates obtained by x-ray diffraction measurements on a multilayered sample (black crosses in the figure [Sha13]) and the results given for two different samples by Nava *et al.*, most likely originate in a systematic deviation of the evaluation procedure or reflect the uncertainty of the measurements. Defect scattering should not dominate at these high temperatures, since the thermal conductivity continually decreases in this temperature region

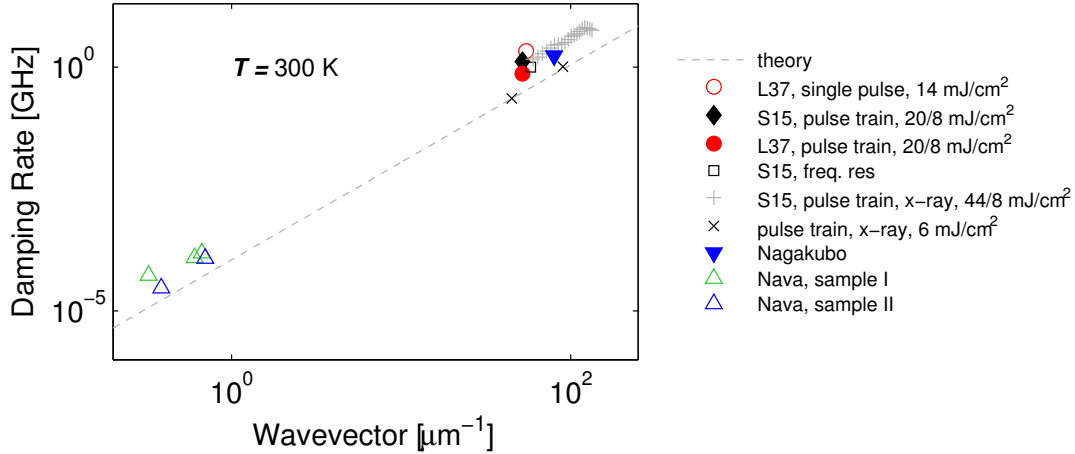


Figure 6.7: Comparison of the observed damping rates at room temperature for various samples and with different measurement techniques with theoretical and literature values. X-ray data according to Herzog *et al.*, using pulse train excitation [Her12b], and Shayduk *et al.*, exciting a superlattice of 5 double layers (sample (c) from chapter 4, the profile is displayed in figure 2.12) [Sha13]. Literature data taken from Nava *et al.* [Nav69] and Nagakubo *et al.* [Nag12]. The theoretical estimation was performed according to the Akhiezer model and literature data as explained in the text.

[Sue65], such that phonon phonon scattering can be expected to dominate the scattering processes of thermal phonons. Since defect scattering increases proportionally to ω_q^4 [Hun07],² it is not likely that the GHz phonons with much lower frequency than the average thermal phonon with frequency of approximately 6 THz, given by the thermal energy $k_B T$ at room temperature, should be affected by defects at room temperature.

6.3.2 Damping at the Phase Transition

The observed damping of phonons in STO as a function of temperature behaves similarly for all measurements: the increase of the damping rate at the high temperature side of the transition is steeper than at the low temperature side. This is in agreement with observations by Rehwald [Reh71] but in contrast to observations by Fossheim and Berre [Fos72]. In particular, there is no systematic difference in the attenuation rate measured for high excitation fluence in comparison to low excitation fluence and the effect of the lattice anharmonicity on the phonon attenuation can be neglected.

In order to quantify the increase of the phonon attenuation at T_a for our measurements and give a better comparison with the results from the literature, we have evaluated the critical exponent η for our measured curves.

²This proportionality holds for scattering centres much smaller than the phonon wavelength [Hun07] and is analogous to Rayleigh scattering of light.

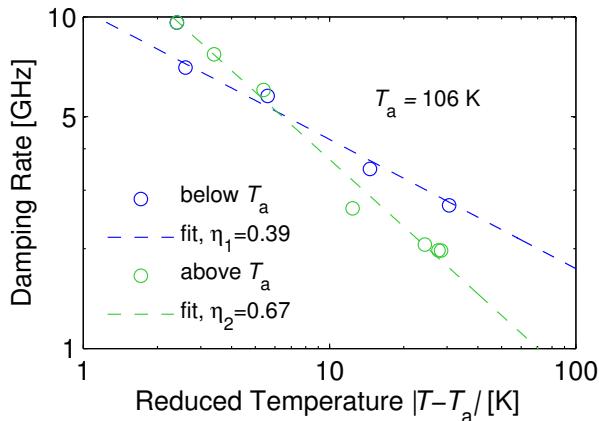


Figure 6.8: Doubly-logarithmic plot of the determined damping rates in the single pulse measurement evaluated at $q = 54.6 \mu\text{m}^{-1}$ as a function of reduced temperature $|T - T_a|$. Above as well as below the phase transition the data points are well described by a linear relation within about ± 30 K of the transition.

Table 6.2: Critical exponent and phase transition temperatures obtained by fitting function 6.3 to the data. For the pulse train excitation the integral fluence is again given by $20 \text{ mJ}/\text{cm}^2$, yielding a per pulse fluence of $10/8 \text{ mJ}/\text{cm}^2 = 1.25 \text{ mJ}/\text{cm}^2$.

technique	sample	T_a [K]	η'	η
single pulse, $15 \text{ mJ}/\text{cm}^2$	L37	106 ± 2	0.4 ± 0.2	0.7 ± 0.25
pulse train, $20/8 \text{ mJ}/\text{cm}^2$	L37	108	0.2 ± 0.1	
	S15	103.5 ± 0.7	0.3 ± 0.2	0.7 ± 0.4
frequency resolved	S15	101 ± 0.1	0.25 ± 0.05	0.75 ± 0.05
	bare STO	101.5 ± 0.5	0.4 ± 0.2	0.7 ± 0.3

We have fitted a function of the form

$$f_{A,B,\eta',\eta,T_a}(T) = A \cdot H(T_a - T)|T - T_a|^{-\eta'} + B \cdot H(T - T_a)|T - T_a|^{-\eta} \quad (6.3)$$

with $H(T)$ the Heaviside step function, amplitudes A and B and critical exponents η' and η below and above the phase transition, respectively, to the data. In figure 6.8 we show a doubly-logarithmic plot of the damping rate for the single pulse measurement on L37 from figure 6.1, as a function of the reduced temperature $|T - T_a|$, together with the fit of the critical exponents. In table 6.2 we summarise the results found for the different measurements presented.

The results agree within the accuracy of the fits. Above the phase transition, they are in agreement with the results found for MHz phonons in the literature, where a critical exponent between 0.9 and 1.2 was reported [Nav69] within 30 K of the transition. However, the values of the critical exponents obtained from our measurements disagree with the previously reported values below the phase transition, where experimental values not lower than 0.8 [Reh71] have been allocated within 0.1 K of the transition. For this measurement, the temperature resolution was much higher than than in our experiments. In the theoretical treatment, values as low as 0.5 [Pyt70] and $1/3$ in the tetragonal phase [Reh71] have been predicted, depending on the dispersion model applied [Reh71] or on the attenuation properties of the soft mode [Pyt70]. The attenuation of the soft mode does not depend on the frequency of

the ultrasound phonon. Since we present the first evaluation of the critical exponent at the antiferroelastic phase transition of STO for GHz phonons, we conclude that the critical exponent of the attenuation is lower for GHz than for MHz phonons. Our evaluation assigns the same critical exponents in the bulk as at surface and we conclude that the character of the transition is the same at the surface and in the bulk.

We do not interpret the variation in T_a determined by the fits. The phase transition temperature is known to depend on the defect density due to the growth technique [Fos85], to differ from surface to bulk [Sal11b] and was found to show a hysteresis [Lyt64]. Furthermore, the determination of the sample temperature may not be exact and varies for the different techniques. Particularly for the time resolved measurements, we expect a temperature gradient between irradiated sample surface and thermometer [Nag12]. This might differ from day to day operation, depending on the coupling of the sample and thermometer to the heat bath and their relative localisation on the sample holder. The difference in the maximum measured attenuation rate may be explained by the finite temperature spacing ΔT for the various measurements and the high sensitivity of the damping rate on temperature at the phase transition. For the pulse train excitation data presented in figure 6.2, measurements on S15 were performed with temperature steps of $\Delta T = 1$ K close to the phase transition. For the measurement on L37, temperature steps of $\Delta T = 2$ K were performed above the transition point but the spacing was $\Delta T = 1$ K below the transition. Since the damping rate diverges at the phase transition, the difference of the maximum value of approximately 5 GHz is most likely due to this effect.

However, a dependence of the maximum attenuation rate at the phase transition on the sample quality has been observed in the literature: Fossheim and Berre [Fos72] found for ultrasound measurements in the 1970s a pressure dependence not only of the transition temperature but also of the maximum attenuation at the phase transition. The authors attribute the higher attenuation and concomitant increase of T_a with increasing pressure to an improved quality of the samples due to the reduction of domain walls. The same group found a dependence of the maximum attenuation on the growth mechanism when comparing measurements on Verneuil-grown and flux-grown samples [Fos85]. A detailed explanation of this effect has not been given. The high attenuation rate found for sample S15 in the pulse train measurements at the phase transition might thus be explained by the partial alignment of the elongated c -axis along the transducer-substrate interface that was discussed in the previous chapter. This alignment reduces the formation of domains along the direction of sound propagation and thus leads to an improved quality of the crystal along this direction in the low temperature phase. For further interpretation of this feature, the damping rate at the phase transition should be measured with smaller temperature steps.

The inelastic coupling of the strain waves to domain walls in STO, as discussed in chapter 5, cannot account for the variation in damping at the phase transition, since it dominates only in the case of high excitation level.

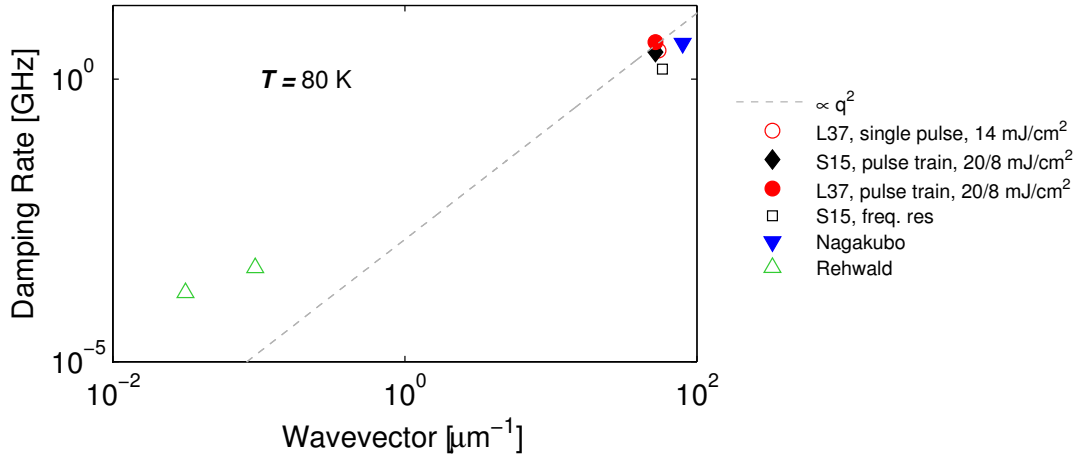


Figure 6.9: Comparison of the obtained damping rates at $T = 80$ K with literature values obtained by Rehwald [Reh70b].

6.3.3 Damping at Low Temperatures

For the lowest temperatures investigated, several new features appear: in the time resolved measurements on the sample with LSMO transducer, the attenuation at low temperatures does not decrease as much as found in all other measurements but stays at a level considerably higher than at room temperature. For this sample a scattering of the evaluated damping rates for temperatures around $T = 40$ K is also observed. In the same temperature region, the frequency resolved measurements in figure 6.4 display a splitting in the observed sound velocity and damping rates. We will first discuss the plateau-like behaviour of the damping observed in sample L37 and then comment on the anomalies at low temperatures.

Plateau Behaviour for Sample L37 below $T = 60$ K

Presuming that the domain structure is different for the samples with different transducer layers, as discussed in chapter 5, this suggests that the effect, which is only observed for sample L37, is associated with domains. Although we exclude the inelastic scattering from domain walls that has been discussed in chapter 5, since it only appears for very high excitation level, the elastic scattering of phonons from differently oriented domains may lead to an attenuation of the coherent phonons. In the literature, scattering from domain walls was found to contribute to the ultrasound attenuation below the phase transition temperature [Fos72].

In figure 6.9 we display a comparison of our hypersound measurements performed at $T = 80$ K in comparison to literature values for phonons in the MHz regime from Rehwald [Reh70b]. For temperature lower than $T = 80$ K no values are found in the literature for phonons in the MHz regime. In contrast to the attenuation rates at room temperature, the literature data in the MHz range cannot be extrapolated according to a q^2 dependence to yield the damping rates for the GHz phonons.

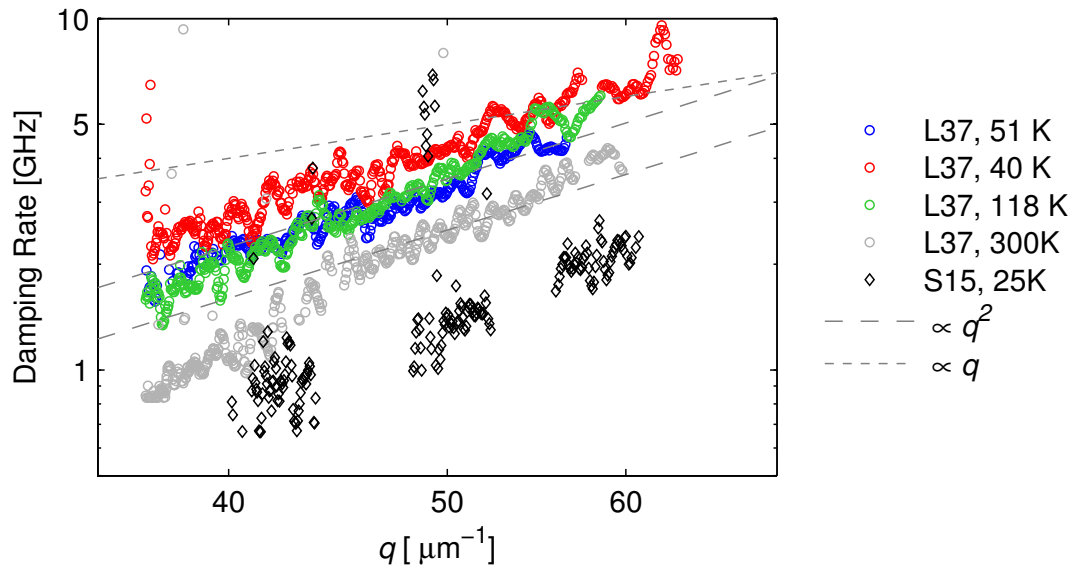


Figure 6.10: Wavevector dependent damping rate. Extracted for sample L37 for different temperatures and for S15 at 25 K. This time an average over approximately 8 nm has been performed in order to obtain a stable fit.

In figure 6.10 we display the results of wavevector dependent fits for the single pulse excitation measurements from figure 6.1 for various temperatures. For $T = 50$ K and $T = 40$ K we find a q^2 dependence of the attenuation rate. For a comparison, we have also displayed the wavevector dependent damping rates for higher temperatures at which the the attenuation displays a wavevector dependence slightly higher than given by an exponent of 2. At these temperatures the damping rates are lowest and the attenuation due to the anharmonic phonon phonon coupling dominates, leading to a wavevector dependence that deviates from the prediction by the Akhiezer model and is not subject of our discussion.

For a scattering of ultrasound phonons from platelets and grain boundaries, a q^2 -dependence of the attenuation rate was predicted for large platelet size in comparison to the phonon wavelength [Tur74, Kle94], which was experimentally supported [Ma13]. Thus, the experimentally detected wavevector dependence is in agreement with the proposed elastic domain wall scattering for domains with a lateral dimension larger than the wavelength of the ultrasound phonons, which amounts to approximately 100 to 200 nanometers. Also shown is the evaluation for sample S15 for measurements at $T = 25$ K. The data scatter more due to a lower signal to noise level but a q^2 dependence is found as well. Unfortunately, from the wavevector dependence of the attenuation, we cannot distinguish the regimes – the phonon phonon scattering regime according to the Akhiezer model and the domain wall scattering regime, since both are characterised by a damping rate following a q^2 dependence. Only the observed magnitude and the assumed domain configuration in the samples gives evidence for the dominant scattering process. In the frequency resolved measurements, this plateau-like scattering contribution is not found. The domain size is

known to be coarser in the bulk than close to the surface [Chr98, Buc99]. Therefore, in the frequency resolved measurements, the density of domain walls, from which the hypersound phonons scatter, can be expected to be smaller, leading to a larger free path of the GHz phonons. From the damping rates at $T = 50$ K in figure 6.4, we estimate a free path of GHz phonons at the surface of approximately $2 \mu\text{m}$ and in the bulk of approximately $8 \mu\text{m}$.

For a transverse acoustic phonon mode along (110) in STO, the q -dependence was found to be linear instead of quadratic [Kor14a]. This means that the Akhiezer model is no longer dominant for transverse modes in this frequency and temperature region.

Anomalies below $T \approx 40$ K

Anomalies at this phase transition have been observed extensively and the origin is highly debated. The transition to an orthorhombic state [Lyt64], the appearance of a novel coherent quantum state [Mül91], the appearance of second sound [Heh95, Kor07] possible increased scattering due to the crossing of the ferroelastic soft mode with the ferroelectric soft mode [Sco95], the formation of polar clusters [Kit00], a ferroelectric phase within ferroelastic twin walls [Sco12, Sal13a] or the appearance of antiphase domain walls [Arz00] and a possible ferroelectric polarisation within these [Tag01] are held responsible for the various anomalies observed in experiments around this temperature. The anomalies were found to be related to a high density of dislocations [Arz03].

From our measurements we conclude that the anomalous increase of the damping rate at low temperatures is related to domains since it appears for the measurements on L37 while it is not present in S15, where we do not expect domain boundaries in the direction of sound propagation. In some measurements, an anomaly in the elastic compliance is observed around this temperature region [Sor69, Nes92, Kit00]. Our measurements of the linear sound velocity presented in figure 5.2 do not support this finding. However, for the high amplitude strain waves, presented in figure 5.5, a scattering of the observed sound velocity at low temperatures was also observed.

This interpretation is supported by the frequency resolved measurements displaying a splitting in the sound velocity, which might be explained by the presence of domains in the sample with differing acoustic behaviour. This parallels an observed energy splitting for transverse acoustic modes observed via Brillouin scattering in the 300 GHz regime by Courtens *et al.* [Cou93].

7. Dynamics in Magnetic Multilayers

In this chapter we show preliminary measurements on magnetic multilayers. They represent an outlook for a future focus of the research group on magnetic samples and magnetisation dynamics, employing magnetic scanning near field microscopy and time resolved magneto-optical Kerr measurements.

The samples discussed in the chapter are superlattices that mimic multiferroic behaviour: ferromagnetic, metallic LSMO is alternately grown with ferroelectric, insulating PZT or BST layers. The samples are listed in table 7.1. Sample II in this chapter is identical to sample (b) in chapter 4. There is a wide research field exploring the coupling of ferroelectric and ferromagnetic properties in composite systems, see Ma *et al.* for an overview [Ma11]. Of particular interest for applications are their switching behaviour and the ultrafast dynamics of the ferroic properties. First we investigate the fluence dependent demagnetisation behaviour in an LSMO-PZT superlattice, sample I. In these measurements we focus on thermalisation effects on the hundred picosecond timescale. In the second part we discuss the appearance of slow oscillations in the optical reflectivity of magnetic superlattices and their possible origin in magneto-elastic coupling. The effect is illustrated with data recorded on the LSMO-BST superlattice, sample II. In the third part of this chapter, we observe fast phonon oscillations and investigate the acoustic properties of sample II across a wide temperature range.

7.1 Fluence Dependent Demagnetisation in Manganites

In this section, we discuss how the excitation with high fluences may influence the temperature dependence of the properties under investigation. The measurements are performed on the LSMO-PZT superlattice, sample I. When an absorbing material is heated by a pump pulse with a fluence of several mJ/cm^2 , first the electrons are heated to a temperature of several tenthousand Kelvins [Lin08]. After fast electron-electron and subsequent electron-phonon equilibration, the electron-phonon system is heated by several hundred Kelvins. This transient change in sample temperature has to be taken into account when thermodynamic quantities, which are normally

Table 7.1: Details of the superlattices selected for this chapter. Each superlattice is grown on an STO(100) substrate. The bulk Curie temperatures for the ferromagnetic (LSMO) and ferroelectric (PZT, BST) phase transitions (compare collection of material properties in table 2.1) are listed.

Nr.	metal	T_C bulk	dielectric IL	T_C bulk	# DL
I	LSMO, 5.4 nm	370 K	PZT, 5.3 nm	750 K	15
II ¹	LSMO, 7.3 nm	370 K	BST, 13.7 nm	300 K	15

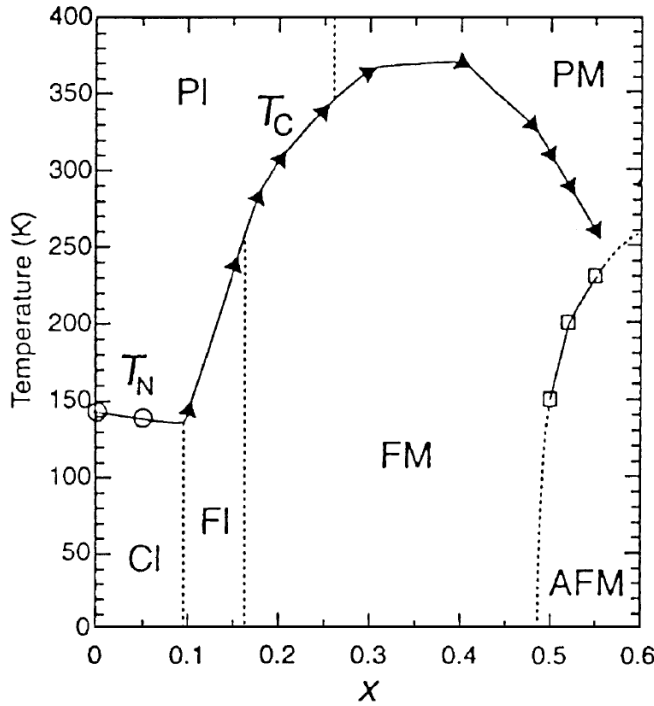


Figure 7.1: Phase diagram of lanthanum manganite doped with strontium, $(\text{La}_{1-x}\text{Sr}_x)\text{MnO}_3$ [Dag01]. There are several magnetic and electronic phases. PM: paramagnetic metal, AFM: antiferromagnetic metal, FM: ferromagnetic metal, PI: paramagnetic insulator, FI: ferromagnetic insulator, CI: spin canted insulator. T_C : Curie temperature, T_N : Néel Temperature.

defined in thermal equilibrium, are evaluated. Particularly at phase transitions many parameters have a very sensitive dependence on temperature. Equilibrium properties are thus better studied using non-amplified pulses with smaller excitation energy but higher repetition rate, yielding a comparable signal to noise ratio. However, for certain pump or probe techniques, e.g. if an optical parametric amplifier is employed for tuning the wavelength for excitation and/or for probing, or when x-ray pulses are used as probe, high excitation fluences are necessary even if equilibrium properties are studied.

The measurements presented here were inspired by the results on ultrafast magnetostriction in strontium ruthenate [Kor08], where the change in optical reflectivity as well as the observed striction on the subpicosecond timescale were found to show a temperature dependence proportional to the magnetisation squared $M(T)^2$. In a manganite, however, the reflectivity changes accompanying the magnetic phase transition are reported to resemble the derivative of the magnetisation with respect to temperature, dM/dT [Hir05]. In the following, we therefore discuss the changes in optical reflectivity and their fluence dependence in a manganite sample.

7.1.1 Introduction to Manganites

Manganites crystallise in the perovskite structure (see introduction of perovskites in section 2.1) and have the composition $(A_xA'_{1-x})\text{MnO}_3$, with the transition metal site occupied by manganese. These materials show very rich phase diagrams and an interesting interplay of the different degrees of freedom: the effect of colossal magnetoresistance found in manganites [Cha93, Jin94] shows the interplay of charge and spin systems while the formation of polarons [Ter97] reveals an intimate relation

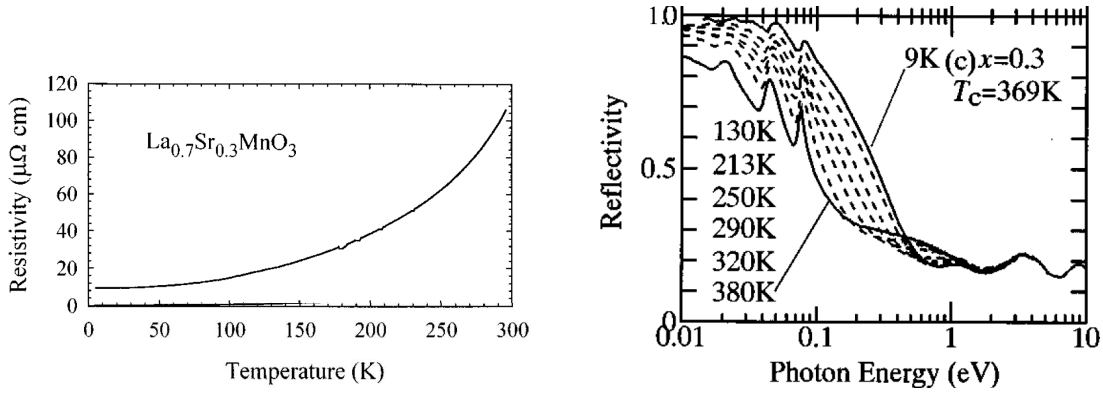


Figure 7.2: Left: electric resistivity of bulk LSMO [Qui98]. Right: static reflectivity of bulk LSMO [Oki97]. While for photon energies around ≈ 0.1 eV the reflectivity decreases with increasing temperature, for higher energies around ≈ 1 eV the effect is reversed: the reflectivity increases with increasing temperature. In the visible, this effect is most pronounced at the red end of the spectrum.

between charge and lattice degrees of freedom. Depending on doping elements and level, a large variety of electronic and magnetic phases are found. In figure 7.1 we display the phase diagram of Sr-doped lanthanum manganites. Depending on doping level and temperature, the material may be insulating or metallic and display a paramagnetic, ferromagnetic, antiferromagnetic or canted spin state.

We concentrate on Sr-doped lanthanum manganites $(\text{La}_{1-x}\text{Sr}_x)\text{MnO}_3$ with doping level $x = 0.3$, showing a ferromagnetic to paramagnetic phase transition and metallic but strongly temperature dependent conductivity. Since the spectral weight over the entire frequency spectrum is conserved, the decrease in conductivity with increasing temperature is accompanied by a spectral weight transfer [Lob00b] from low energies and intraband transitions at $E < 1$ eV, to interband transitions above $E = 1$ eV. The lowest of these interband transitions are the orbital transitions from O $2p$ to Mn $3d$ [Oki97].

In figure 7.2 we display measured temperature dependent resistivity (left panel) and static reflectivity (right panel) from the literature [Qui98, Oki97] for a bulk LSMO sample with Sr-doping of $x = 0.3$. While the temperature is decreased, the resistivity decreases. The decrease in resistivity is accompanied by a decrease of the plasma frequency. The plasma frequency specifies at which frequency the metallic reflectivity drops and the material becomes transparent. A high conductivity is accompanied with high reflectivity up to high frequencies, low conductivity leads to a decrease of reflectivity already at lower frequencies. While the intraband conductivity decreases with decreasing conductivity, the interband conductivity is gaining importance and the reflectivity for intermediate photon energies ($E > 0.5$ eV) increases. In the visible region the induced change in reflectivity is most pronounced at the red end of the spectrum. Information about the magnetic state of manganites can thus be obtained optically by either performing experiments that are directly sensitive to the magnetisation of the sample, exploiting for example the magneto-

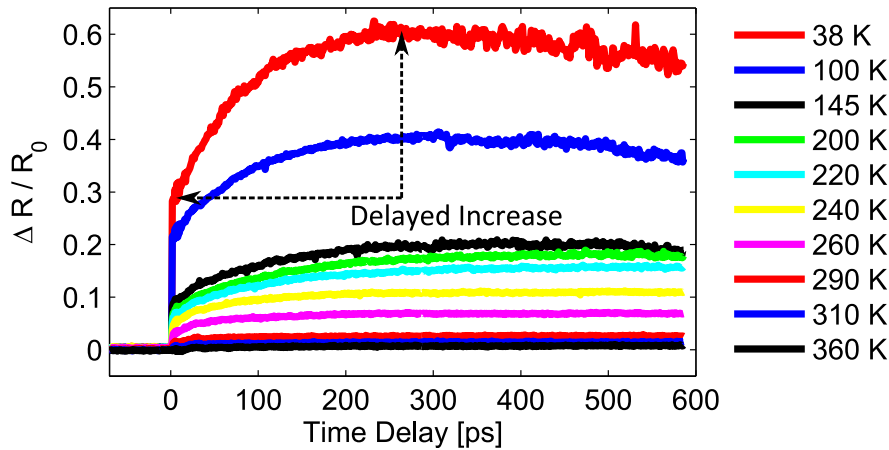


Figure 7.3: Time resolved change in optical reflectivity for $\lambda = 814$ nm, measured at different base temperatures. The delayed reflectivity increase that will further be evaluated is indicated with black dashed arrows.

optical Kerr effect for time resolved measurements in the visible region [Oga05], or else by optical spectroscopy, thus learning about the electronic states of the material, as has been done by several groups [Lob00a, Hir05]. These experiments reveal a comparatively slow demagnetisation of manganites on the order of several hundreds of picoseconds. For comparison: ultrafast demagnetisation in the sub-ps range has been found in an experiment on nickel by Beaupaire *et al.* [Bea96] and has later been observed in many other metals, see [Kir10] for an overview.

7.1.2 Time Resolved Reflectivity Changes

In this section we show measurements on sample I, which consists of 15 double layers of PZT (5.4 nm) and LSMO (5.3 nm) on an STO substrate [Vre08b]. PZT is a tetragonal, displacement-type ferroelectric below 750 K [Izy07]. The ferromagnetic Curie temperature of the LSMO layers was measured to amount to $T_C = 320$ K [Vre08b].

In figure 7.3 we display the time resolved change in optical reflectivity recorded for different starting temperatures of the sample evaluated for the probe wavelength $\lambda = 814$ nm. We notice a delayed increase in reflectivity that only appears in the low temperature ferromagnetic phase. Since the demagnetisation in manganites is known to take several hundreds of picoseconds [Oga05], we assign this signature to the demagnetisation in our sample.

Figure 7.4 displays the time dependent relative change in optical reflectivity after electron-phonon equilibration for different probe wavelengths measured at two temperatures. The delayed increase in reflectivity is most pronounced in the near infrared, as expected from static measurements shown in the right panel of figure 7.2. In the following, we therefore concentrate on reflectivity changes for probe light with $\lambda = 814$ nm, since the effect seems to be most notable in the near infrared.

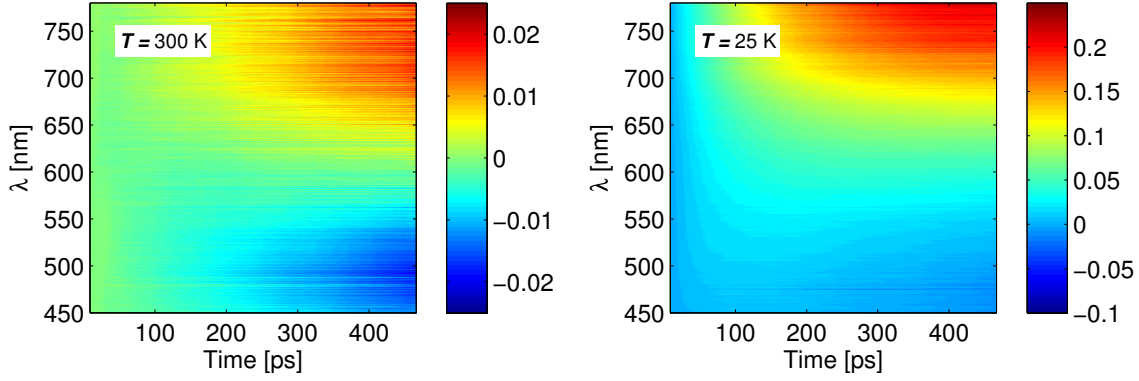


Figure 7.4: Measured change in optical reflectivity in the visible part of the spectrum after electron-phonon equilibration. Left: $T=300$ K, the sample shows only a gradual, very small change in reflectivity. Right: $T=25$ K there is a delayed increase in reflectivity that is most pronounced at the red end of the spectrum.

7.1.3 Temperature Dependent Signatures in the Measurements

In the left panel of figure 7.5 we show the evaluated relative change in reflectivity between the minimum after the electronic peak and the delayed maximum, i.e. the increase in reflectivity after phonon equilibration for $\lambda = 814$ nm and different starting temperatures. The high fluence data display a gradual decrease of reflectivity change with increasing temperature, whereas the low fluence data exhibit a peak in change of reflectivity just below the phase transition temperature of $T_C = 320$ K.

We have fitted an exponential rise of the form

$$f_{A,\tau_{\text{rise}},C}(t) = -Ae^{-t/\tau_{\text{rise}}} + C \quad (7.1)$$

with amplitude A , rise time τ_{rise} and offset C to the data. The right panel of figure 7.5 displays the result of the fits to the delayed rise of the reflectivity. For low excitation

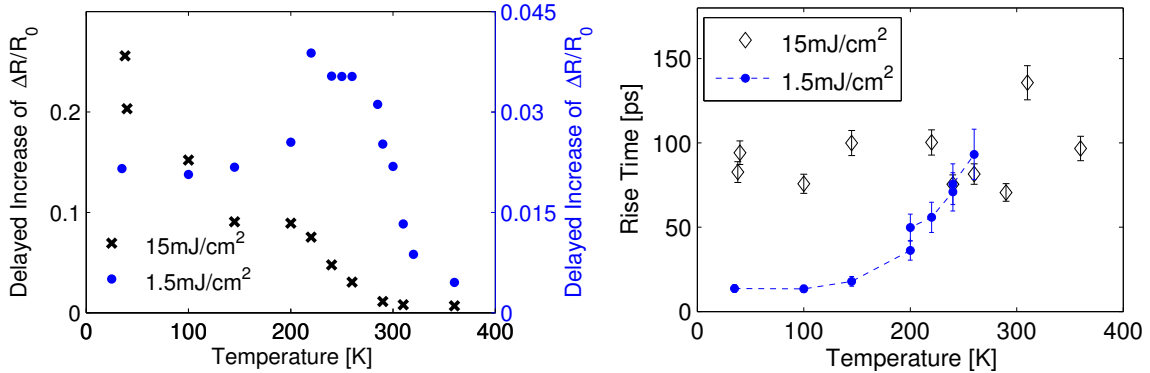


Figure 7.5: Left: evaluated increase of reflectivity after electron-phonon equilibration, evaluated at $\lambda = 814$ nm for different temperatures. Right: equilibration time obtained by fitting an exponential to the delayed rise of figure 7.4 for $\lambda = 814$ nm.

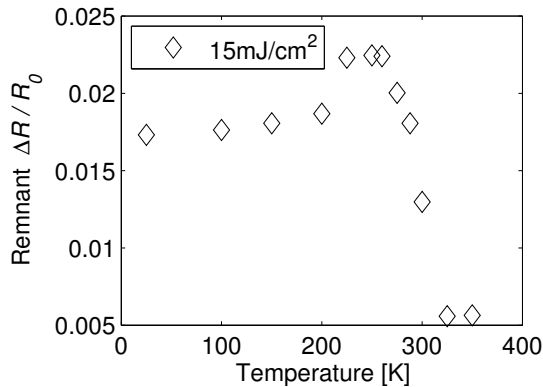


Figure 7.6: Remnant reflectivity increase before zero time delay i.e. 200 μs after excitation. The presented data have been evaluated at $\lambda = 770$ nm.

fluence the equilibration time peaks at the phase transition. For the data measured at high excitation fluence, there is no trend in the temperature dependence of the rise time. For the low excitation fluence, the observed feature becomes very small above the phase transition and no stable fit could be obtained.

This slowing down of the equilibration time at the phase transition observed for low excitation fluence, is also manifested in the following observation: evaluating the remnant change in optical reflectivity before zero time delay [Lob00b], which is $t = 200$ μs after excitation for our 5 kHz laser system, we observe an increase of the reflectivity compared to the unpumped value. The temperature dependence of this effect yields a maximum below the phase transition, as shown in figure 7.6, meaning that the flow of heat into the heat bath is delayed close to T_C . This is only seen for high excitation level, as shown in the figure. For low excitation fluence, this remnant increase was too small for an evaluation.

7.1.4 Estimated Changes of the Magnetisation

Let us now estimate the temperature dependent changes of the sample magnetisation. With given absorption length [Qui98, Oki95] and heat capacity [Khl00], the instantaneous temperature increase for different starting temperatures can be estimated for different excitation fluences, as shown in the left panel of figure 7.7. For this estimation we assume that the energy is instantaneously deposited in the bath of electrons, phonons and spins, as if they were in thermal equilibrium. We neglect that while the magnetic system slowly equilibrates with the electron-phonon system, some energy is already lost due to heat diffusion. With constant excitation fluence, the estimated temperature increase decreases, since the overall heat capacity continually increases with increasing temperature. At the phase transition there is a small ripple in each curve. It appears, where the heat capacity of the magnetic system has its maximum.

In the right panel of figure 7.7 we display the temperature dependent magnetisation as measured for the sample [Vre08b] as black dash-dotted line. We also display the estimated temperature changes according to the left panel for a starting temperature of about 20 K as arrows for high (black dash-dotted arrow) and low (blue arrow) excitation level. For low excitation level, we also display the estimated tem-

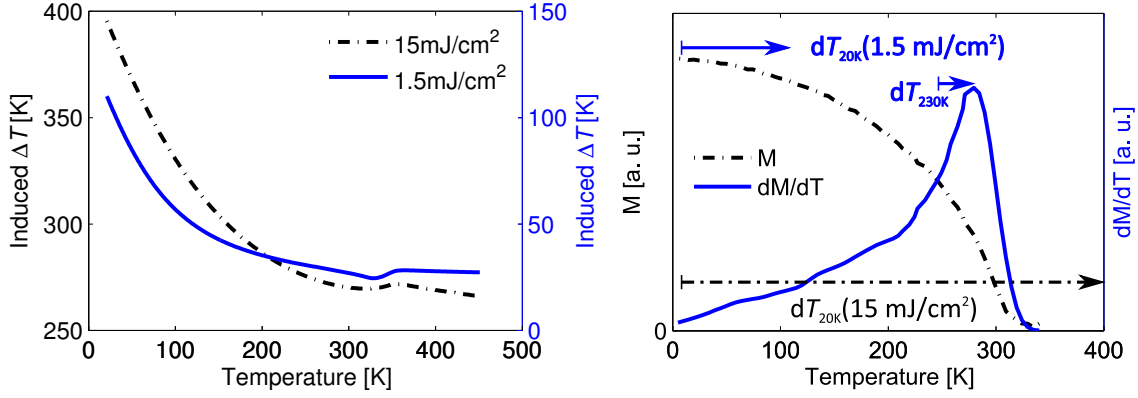


Figure 7.7: Left: calculated average temperature increase of the LSMO layers after excitation with different pump fluences, using the heat capacity measured by Khlopkin *et al.* [Khl00]. Blue curve: $F=1.5 \text{ mJ/cm}^2$, left temperature axis, black dash-dotted curve: $F=15 \text{ mJ/cm}^2$, right temperature axis. Right: measured temperature dependence of the magnetisation according to [Vre08b] as black dash-dotted line. The derivative of the magnetisation with respect to temperature, dM/dT is shown as blue curve. This curve displays a similar Temperature dependence as the heat capacity of the magnetic system.

perature increase just below the phase transition temperature. We find that for the high excitation fluence of 15 mJ/cm^2 , the film is always excited into the paramagnetic phase. For the lower excitation fluence of 1.5 mJ/cm^2 , however, the estimated induced temperature increase is smaller, particularly at the phase transition. For low excitation fluence, only at starting temperatures close to the phase transition we expect to induce a complete demagnetisation. With the known temperature dependence of the magnetisation, the induced change in magnetisation can be estimated: we integrate the calculated derivative of the magnetisation from the right panel of figure 7.7 (shown as blue line) over the calculated induced temperature change for two different excitation fluences according to the left panel, $\Delta M = \int_T^{T+\Delta T} (dM/dT)dT$. The results are shown in figure 7.8 for the two excitation fluences.

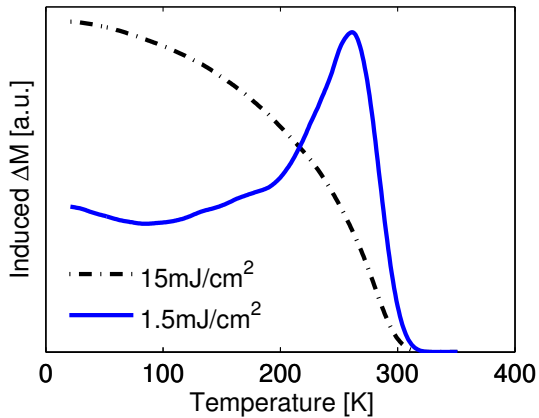


Figure 7.8: Estimated change in magnetisation following the temperature increase according to figure 7.7 for two different pump fluences using the magnetisation curve measured for the sample by Vrejiou *et al.* [Vre08b], displayed in the right panel of figure 7.7.

For high excitation fluences the induced change in magnetisation is equal to the static magnetisation at the starting temperature and the curve therefore resembles

the temperature dependent magnetisation curve, similar to the $M(T)^2$ dependence observed by Korff *et al.* [Kor08]. For low excitation fluence and thus smaller temperature changes, the induced change in magnetisation resembles the derivative of the magnetisation curve. For infinitively small temperature changes measured e.g. with unamplified laser pulses at high repetition rates, the change in magnetisation equals the derivative of the magnetisation curve, see for example the measurements of Hirobe *et al.* [Hir05].

Using the two temperature model, which has been introduced in section 2.3.3, the equilibration time of two interacting heat baths is given by the relation

$$\tau_{12} = \frac{C_1 C_2}{G_{12}(C_1 + C_2)} \approx \frac{C_1}{G_{12}}, \quad (7.2)$$

where the approximation holds when the heat capacity C_1 of one system is small compared to the other C_2 . In LSMO, the heat capacity of the spin system maximally amounts to about 20 % of the total heat capacity [Khl00]. The coupling constant G_{12} usually does not change much with temperature. Therefore, in equilibrium, the equilibration time should scale with the heat capacity of the spin system and should peak at the phase transition temperature. This slowing down of the dynamics at the phase transition is known as the critical slowing down effect [Kis00], appearing at second order phase transitions according to Landau theory of phase transitions [Fli10].

With the above observations, we have found an explanation, why the evaluated features observed in transient optical reflectivity show qualitatively different temperature dependence depending on excitation fluence. For high excitation fluence, the sample is always pumped into the paramagnetic state and the feature related to the magnetisation decreases with increasing starting temperature following the curve of the magnetisation. For low excitation, the induced change in magnetisation is maximum just below the phase transition, since the dependence of the magnetisation on temperature is largest here (compare left panel of figure 7.5 with figure 7.8). The phonon-magnon equilibration time is largest just below the phase transition temperature because at this point the magnon heat capacity is largest, compare formula 7.2. Therefore, for low fluence excitation, the observed rise of the reflectivity is slowest just below the phase transition, as shown in the right panel of figure 7.5. For high excitation, this 'bottleneck' of the equilibration at the phase transition is always passed, slowing down the equilibration for all temperatures. Similarly, the heat flow out of the magnetic system into the phononic heat bath after excitation is delayed maximally just below the phase transition, which leads to a maximum increase of remnant reflectivity change before the arrival of the next pulse, i.e. 200 μs after excitation, that peaks below T_C .

Summarising, we have measured the temperature dependent change in optical reflectivity of an LSMO sample. We have performed measurements at different temperatures and two different excitation fluences. We focused on the slow increase of the reflectivity that we attribute to the change in magnetic and electronic properties of the material. We found that the temperature dependence of the discussed features

resembles the temperature dependence of the magnetisation for high excitation fluences whereas for low excitation fluences, it resembles its derivative. These measurements emphasise that the level of excitation and the induced transient temperature increase of a material have to be considered when the temperature dependence of material properties are evaluated and interpreted.

7.2 Slow Reflectivity Oscillations in Magnetic Multilayers

7.2.1 Spectroscopic Evidence for Ferromagnetic Phase in (La,Sr)MnO₃-(Ba,Sr)TiO₃ Multilayer

The slow change in infrared reflectivity attributed to the demagnetisation of LSMO, as discussed in the last section, was observed for several thin film or multilayered samples comprising LSMO layers. However, the LSMO-BST multilayer, sample II, does not show the reported slow dynamics on the several hundred ps timescale. As shown in figure 7.9, the time resolved reflectivity signal for this sample relaxes very slowly back to zero after the electron phonon equilibration. An evaluation as presented in the previous section cannot be performed for this sample. In contrast,

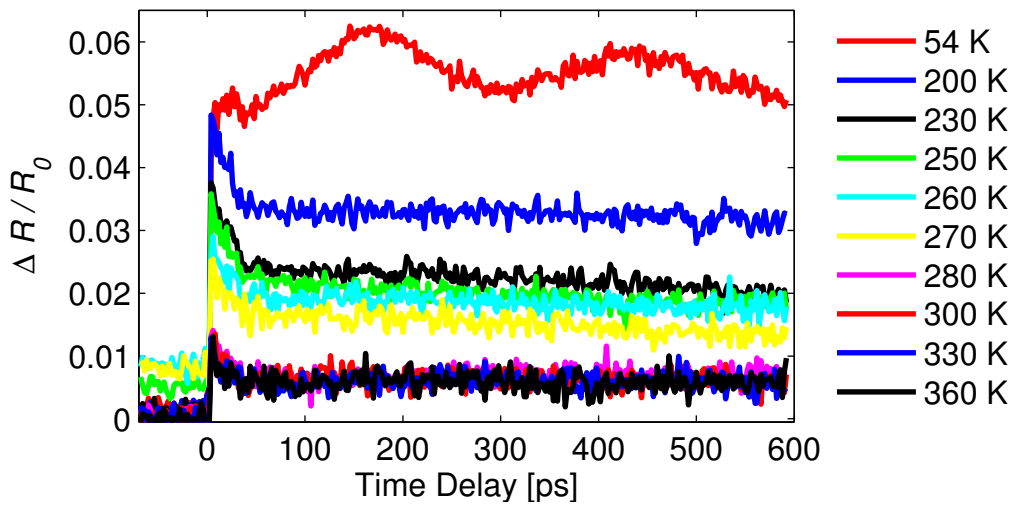


Figure 7.9: Time resolved transient reflectivity signal for sample II, evaluated at $\lambda = 770$ nm. The excitation fluences was $F \approx 40$ mJ/cm².

at low temperatures an oscillation sets in, which was not observed in other LSMO samples. We do not know the origin of this oscillation but we speculate that it appears due to the coupling of the induced strain to the magnetisation in the sample. The effect will be discussed in the next section.

Although the spectroscopic response is different to other manganite samples, a magnetisation should be present also in this sample: the ferromagnetic Curie temperature of LSMO samples was found to decrease with decreasing layer thickness, but the ferromagnetic order was found to be stable down to a layer thickness of 2 unit

cells [Zie12]. In particular, the LSMO layers in sample II are thicker than in sample I above, for which a ferromagnetic phase below $T_C = 320$ K was found. However, if the Sr-doping does not exactly amount to $x = 0.3$, or if it varies locally in the layers, an antiferromagnetic phase or a ferromagnetic insulating phase might arise, as can be inferred from the phase diagram in figure 7.1. This might lead to a different reflectivity response upon changes in the temperature of the magnetic system. It is furthermore possible that the coupling to the ferroelectric BST layers alters the magnetic dynamics in the LSMO layers. To clarify the magnetic properties of the sample, magnetic characterisation needs to be performed.

7.2.2 Slow Reflectivity Oscillations Observed in Magnetic Multilayers

In contrast to the measurements on sample I presented above, a slow oscillation on the several hundred ps time scale was found for low temperatures in the time resolved reflectivity measurements on sample II, as shown in figure 7.9 for $T = 54$ K. We believe that the oscillations are associated with processes in the ferromagnetic phase, because they never appeared above T_C and we are not aware of other dynamics in the sample with a period on this timescale. Slow oscillations with a comparable period were found for a superlattice with 30 double layers of STO (9 nm) and SRO (5 nm) below the Curie Temperature of $T_C = 160$ K. The oscillation period was independent of the probe wavelength and excitation fluence.² The feature was independent of temperature but it was not reproducible for subsequent cooling cycles.

We suggest the following origin of the observed oscillation: the induced strain may alter the magnetic anisotropy of the sample. This will transiently alter the orientation of the sample magnetisation. When the strain has passed the sample, the resulting magnetisation will start precessing around the original orientation of the magnetic anisotropy, which can be observed via the transverse magneto-optical Kerr effect.

In thin films, there is a preferential orientation of the magnetisation due to the competition between shape anisotropy and magnetocrystalline anisotropy [Stö06]: for very thin films, the magnetocrystalline anisotropy, which strongly depends on stress or epitaxial growth, dominates and the magnetisation is oriented out-of-plane. For layers of intermediate thickness, the shape anisotropy dominates and the magnetisation is oriented in-plane. For Ca-doped lanthanum manganite films of 25 nm thickness, the magnetisation was found to point out-of-plane for a growth on LaAlO_3 substrates and in-plane for a growth on STO substrates [Nat99] and we conclude that for manganite films with a thickness of about 10 nm, both orientations are possible depending on the strain conditions. The thickness dependence of the magnetic anisotropy in LSMO films was studied in [Per11].

Inducing a strain pulse, the magnetocrystalline anisotropy may change size and the resulting anisotropy and thus the preferred orientation of the magnetisation may change direction. Whenever the magnetisation does not point into the direction of the effective magnetic field, which is in this case dominated by the anisotropy field, a

²The fluence dependence was only measured for the SRO-STO sample.

precessional motion around the field direction sets in [Stö06] and the magnetisation changes its orientation. The motion is damped, dragging the magnetisation slowly into the direction of the field. After the strain pulse has passed the magnetic layers, there will be a remnant change of the magnetisation orientation compared to the former equilibrium value, if the mechanism explained above has been effective. The magnetisation precesses around the resulting anisotropy field that is determined by the current temperature in the layers and may differ slightly from the orientation before excitation. The effect has been studied on (GaMn)As films with and without the influence of an external magnetic field [Sch10, The10, Lin11, Bom12].

Although we are not directly sensitive to magnetisation changes in our measurements, we propose that we detect in-plane changes of the sample magnetisation via the transverse magneto-optical Kerr effect. Hereby, the in-plane magnetisation leads to a change in intensity of the reflected in-plane polarised light of the probe pulse [Hub98], which is thus detected as an intensity modulation in our experiments.

The proposed effect only occurs, when the anisotropy field changes direction due to the induced strain. This can be found when the magnetisation is initially pointing neither in-plane nor out-of-plane but is tilted with respect to the surface plane. In this case, the strain pulse transiently alters the delicate balance between shape anisotropy and magnetocrystalline anisotropy. The effect can also occur when the anisotropy field points in-plane or out-of-plane and the strain pulse is sufficient to alter the direction of the anisotropy field. In any case, very specific conditions regarding the magnetic anisotropy and its strain dependence need to be fulfilled for this effect to occur. We suggest that these conditions were accidentally fulfilled for those samples, for which the oscillations were observed, while they were not fulfilled for most other samples studied.

For the measurements on sample II shown in figure 7.9, the oscillations do not appear for a start temperature of 200 K, although the Curie temperature can be expected to lie close to room temperature for this sample [Zie12]. However, the stated start temperature is not accurate, as discussed in section 3.1.1, and the transient heating of the magnetic system probably destroys the magnetisation before the oscillation sets in: the excitation fluence of $F \approx 40 \text{ mJ/cm}^2$ was very high in this measurement, leading to a large temperature gradient between the sample surface and the temperature sensor and a possibly large discrepancy between stated temperature in the figure and actual temperature in the sample. Since the overall induced temperature change for this excitation fluence most likely exceeds 600 K (compare estimations in figure 7.7) for all starting temperatures, the magnetic order is probably destroyed before the oscillation sets in for starting temperatures of 200 K or higher, even though the demagnetisation is slow in manganites. Thus we concluded that the slow oscillation is related to the ferromagnetic phase, although it is not visible at 200 K for this excitation fluence.

Since we did not apply an external magnetic field, we have no control over the domain configuration. For repeated cooling cycles the domain configuration probably varies and it will be different for different spots on the sample. In the measurements an average over the probed volume is obtained and we propose that the domain

configuration changes for each cooling cycle. Therefore, the observed feature is not reproducible for different cooling cycles.

For a more solid interpretation of the observed oscillation, the magnitude of the oscillation feature should be studied dependent on the polarisation of the probe light. Alternatively, but more difficult to achieve, the dependence of this effect on the direction of an externally applied field and its magnitude can be studied.

7.3 Temperature Dependent Sound Velocity of a Ferroic Heterostructure

In comparison to the sample discussed above, where the dielectric interlayer shows the ferroelectric phase transition for bulk at around 750 K, the Curie temperature for BST is close to room temperature and is therefore more easily accessible in experiments. For LSMO-BST heterostructures a large magnetoelectric coupling was found [Mar12] making them attractive for applications.

7.3.1 Temperature dependent sound velocity

In this section, we focus on the dynamics in the LSMO-BST superlattice in the first approximately 35 picoseconds after excitation, in which the coherent excitation is still present in the superlattice. The dependence of the observed spectrum on the length of the observational window has already been discussed in section 4.5. In

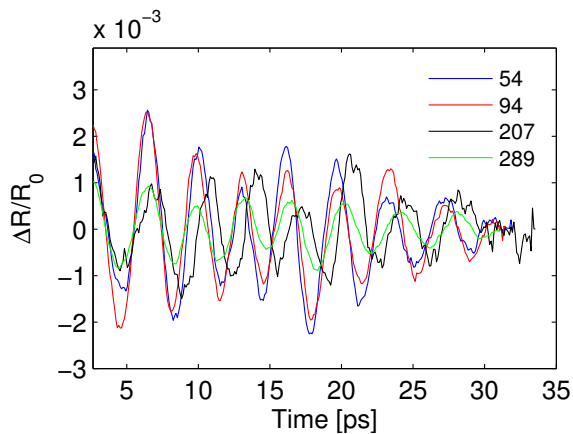


Figure 7.10: Transient reflectivity change for $\lambda = 575$ nm and different temperatures, measured for an excitation fluence of $F = 30$ mJ/cm². The data have been shifted on the time axis to ensure a comparable phase at zero time delay.

figure 7.10 we display the time resolved reflectivity signal (background subtracted), obtained at $\lambda = 575$ nm for different temperatures. The curves were shifted in time to ensure approximately equal phases for early times. For each temperature, the temporal behaviour of the signal is different. Taking the Fourier transform for each temperature, we obtain two dominant peaks in the spectrum, as shown in figure 7.11 for four different temperatures. The temporal windows from which the transforms are generated are each approximately 35 ps wide. We fitted gaussian curves of the

form

$$f_{A_1, A_2, \sigma_1, \sigma_2, \nu_{q1}, \nu_{q2}}(t) = \frac{A_1}{2\pi\sigma_1} \exp\left(-\frac{(\nu - \nu_{q1})^2}{2\sigma_1^2}\right) + \frac{A_2}{2\pi\sigma_2} \exp\left(-\frac{(\nu - \nu_{q2})^2}{2\sigma_2^2}\right) \quad (7.3)$$

to the spectral peaks, where $A_{1,2}$ are the Fourier amplitudes, $\sigma_{1,2}$ the widths and $\nu_{q1, q2}$ the frequencies of the peaks. The fits yield a good agreement with the data. The fit results are overlaid in the contourplots of figure 7.11 as black lines. We average

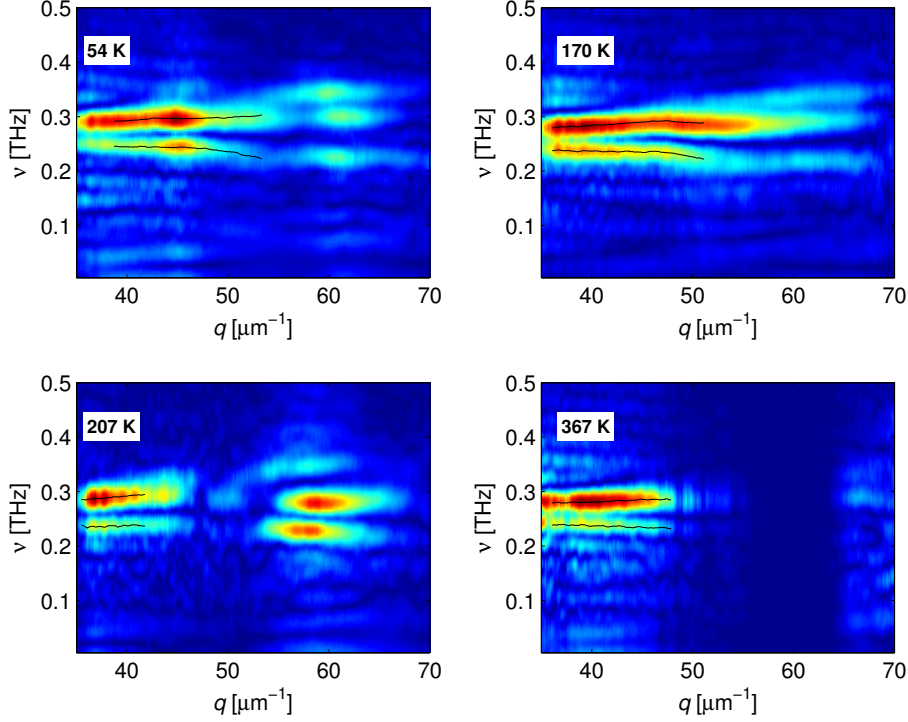


Figure 7.11: Fourier transform of the time resolved reflectivity signal at different temperatures. The peaks in the Fourier transforms are fitted with Gaussian functions and the results are shown in the figures as black lines.

the obtained fits for each temperature over those wavelengths, for which reliable fits were obtained for all measured temperatures. The wavelengths, for which the averages were obtained, correspond³ to q ranging from 39 to 44 μm^{-1} . The results are displayed in the left panel of figure 7.12. The errorbars represent the standard deviation obtained by the averaging over several wavelengths. We note a gradual decrease of the oscillation frequency with increasing temperature and a maximum around 210 K.

In order to determine the sound velocity in the sample, we first need to assign the observed peaks to the expected peaks according to the dispersion relation.

³In this presentation, the wavevector displayed is only valid for backscattering phonons, as discussed above. The averaging has been performed over those probe wavelengths that correspond to q ranging from 39 to 44 μm^{-1} in backscattering.

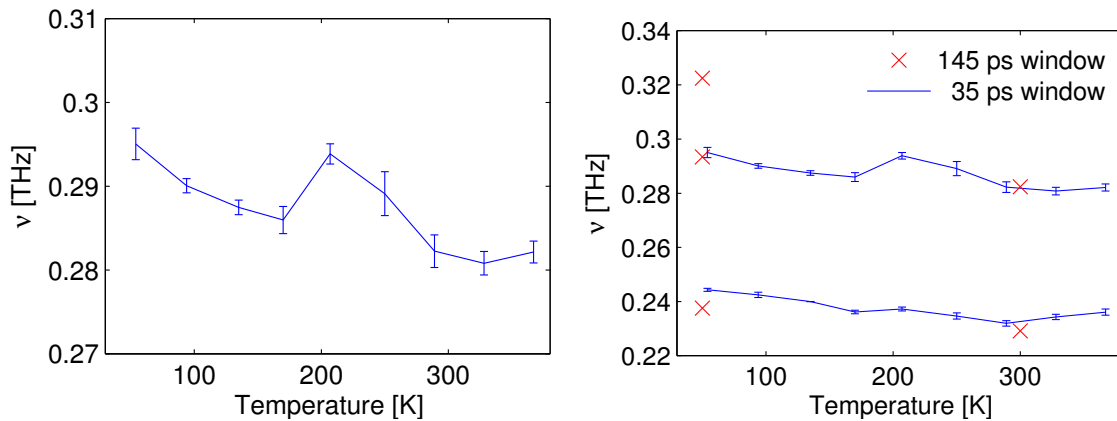


Figure 7.12: Left: frequency of the most intense peak evaluated for different temperatures, q averaged from 39 to 44 μm^{-1} . Right: comparison of fits obtained at various temperatures for short temporal windows with two data sets with large temporal windows.

From the oscillation period observed in forward scattering, the sound velocity can unambiguously be determined under the assumption of a temperature independent layer thickness: $v = d_{\text{SL}}\nu$, as derived in section 2.4.1 on phonons in multilayers. For the backscattering branches the wavelength dependent refractive index has to be estimated for each temperature in order to extract the correct sound velocity. Therefore, it is not possible to accurately compute the sound velocity from the peaks observed in backscattering. Surprisingly, all branches display a dependence of oscillation frequency on wavelength or wavevector, so it is not straightforward to assign the peaks to points in the dispersion relation. Because of the temporal changes in the spectrum discussed above, we cannot be sure that the most intense peak, for which the temperature dependent average was calculated, always corresponds to the forward scattering branch that we are most interested in. The right panel of figure 7.12 displays the obtained frequencies for all temperatures in comparison to longer measurements obtained at 50 and 300 K, where the time window was long enough to cover all the coherent dynamics in the superlattice (for the data of the measurement at room temperature see figures 4.1 and 4.3 in chapter 4). For these two measurements, the branches could unambiguously be assigned. For the measurement taken at 50 K, a good fit was obtained even for the third peak corresponding to the upper backfolded branch.

The results for the longer measurements excellently agree with the ones obtained for shorter times for the forward scattering branch. This supports the conclusion that the most intense peak evaluated corresponds for all temperatures to the peak observed in forward scattering for those wavevectors, for which the average was obtained.

Since the amplitude in the optical experiments sensitively depends on the probe wavelength and the optical constants at the given temperature, we do not discuss this fit result for the optical data.

7.3.2 Time Resolved X-ray Diffraction Data

In addition to the data presented above, time resolved x-ray diffraction measurements have been performed on the sample at different temperatures by Schick [Sch13b]. The layers in the superlattice periodically expand and contract. Therefore, the envelope functions of the superlattice Bragg reflections originating from the layer thicknesses, periodically shift towards and away from each other. Peaks that originate from the superlattice periodicity periodically change intensity [Her12c].

The time dependent relative intensity of the Bragg peak labelled as 'SL-1' [Sch13b] was evaluated fitting a damped cosine to the data. The results of the fits are dis-

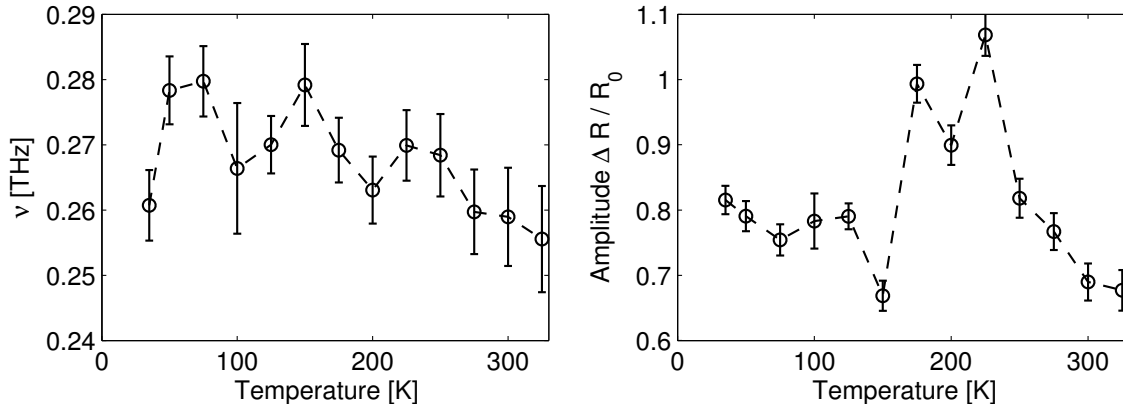


Figure 7.13: Left: temperature dependent frequency of the superlattice oscillation. Right: temperature dependent amplitude of the oscillation.

played in figure 7.13. The period gradually increases with increasing temperature. Interestingly, the amplitude of the lattice oscillations increases as the temperature is decreased and displays a peak around $T = 200$ K.

7.3.3 Comparison of Results

In figure 7.14 we compare the extracted frequencies from the all-optical and x-ray experiments. The oscillation determined in the x-ray measurements should be identical to the one observed all-optically in forward scattering. However, for all measurements on this sample, the frequency of the superlattice oscillation determined in the optical experiments is higher than theoretically expected, shown as green diamond in the figure, and is asymmetrically shifted towards the upper backfolded branch, as has already been seen in figures 4.3, 4.7, 4.9 and 4.10. In chapter 4, this asymmetry was explained by a possible interference between the forward scattered and the backscattered light. The presented optical measurements were taken at lower excitation fluence. However, a possible fluence dependence of the sound velocity can be excluded, since no fluence dependence of the oscillation frequency was found in the optical measurements. Another possible explanation for different oscillation frequencies in both experiments could be a slightly different layer thickness. This is a possible explanation since the x-ray measurements were performed on a different part

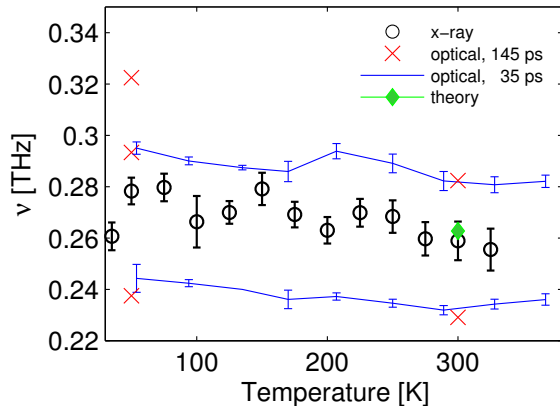


Figure 7.14: Comparison of the oscillation frequencies obtained from x-ray diffraction and optical reflectivity. Also shown is the frequency of the oscillation as calculated from the sample parameters at room temperature displayed in figure 4.2 in the discussion of the multilayers in chapter 4.

of the sample and a gradient of layer thicknesses across the sample is possible. However, because the peak observed in forward scattering in the optical measurements is not located centrally between the two backfolded branches, the proposed interference effect or another unknown measurement artifact in the optical experiment, are the most plausible explanation for the difference in frequencies detected optically and via x-ray diffraction. Both techniques find a gradual hardening of the superlattice towards lower temperatures and an anomaly around 200 K – observed in the frequency for the optical experiments and in the amplitude for the x-ray diffraction measurements.

7.3.4 Interpretation of Results – Phase Transition in $(\text{Ba,Sr})\text{TiO}_3$

We do at the moment not know the origin of the observed anomalies, but there are several arguments that suggest a structural transition in BST, which may account for the observed effects. In the literature, a change in sound velocity of about 8% in BTO between 300 K and 600 K, across the ferroelectric phase transition around 400 K [Ko08] was found. This is fairly large compared to e.g. a maximum change in sound velocity of STO at the phase transition of less than 4%. In the measurement presented here, we observe a change in superlattice sound velocity of about 5% across the whole temperature range. If we assume that the changes only take place in BST, which constitutes about 65% of the superlattice, the changes in BST sound velocity amount to 7-8% and thus agrees with the sound velocity change found in BTO. We do not expect any sound velocity changes in LSMO since we have performed similar measurements with sample I, the LSMO/PZT superlattice, and observed no temperature dependence of the superlattice oscillation frequency. Furthermore, we are not aware of reports on changes of the acoustic properties in LSMO in the literature. A change in sound velocity has only been found for Ca-doped lanthanum manganite, $(\text{La,Ca})\text{MnO}_3$, at the transition to a charge ordered phase [Ram96].

The change of oscillation amplitude observed in the x-ray experiments and the small peak of the oscillation frequency from the optical measurements might originate from a phase transition in the strained BST layers. Calculations imply that the ferroelectric phase transition with a structural transition from cubic to tetragonal

for bulk BST is observed at around 300 K [Shi06]. Due to the epitaxial strain in the layers, the transition temperature for the ferroelectric transition is expected to shift towards higher values [Shi09]. There are, however additional structural phase transitions in BST at lower temperatures [Shi06], where the transition temperature also shows a strong dependence on the epitaxial strain. A hardening of the material would be accompanied by an increase of the oscillation amplitude. However, at the structural transition rather a softening of the material is expected.⁴

In order to interpret the observed effects, additional measurements should be performed. For a better interpretation of the results obtained so far, further structural information on the static structure at different temperatures is needed. A better signal to noise level, obtained by increasing the number of averages, and a longer measurement window for the x-ray measurements can improve the results. More reliable results could also be obtained by using a longer superlattice with equal periodicity but thinner metallic layers. This would increase the lifetime of the superlattice oscillation and decrease the widths of the forward and backscattering Fourier peaks, possibly overcoming the interference effect in the optical data.

Summarising, we have observed a gradual hardening of the LSMO-BST superlattice on cooling from 300 K to about 50 K. Additionally, we have found an anomaly in the results at around 200 K, which is an indication for a structural phase transition in the BST layers.

⁴At displacive, second order structural phase transitions, a soft mode is observed [Sco74, Fle76], which leads to a softening of the acoustic properties of the material.

8. Summary and Outlook

In this work, I have presented a thorough investigation of ultrafast dynamics in perovskite oxides using femtosecond optical spectroscopy. I focused on the observation of coherent phonon dynamics in various nanolayered samples observed by time resolved Brillouin scattering. The investigations were performed at and below ferroic phase transitions and revealed fundamental insight into the coupling of the involved collective excitations.

Coherent phonons were generated using optically excited metal layers as transducers. As an illustration of the technique, I explained specific periodic features in the time resolved data measured on various thin film and multilayered samples.

The central topic of the thesis is the investigation of phonon dynamics in SrTiO_3 in the vicinity of and below the ferroelastic phase transition at $T_a = 105$ K. I evaluated the acoustic sound velocity for various strain amplitudes. Approaching the phase transition from above, a sudden drop in the sound velocity at the phase transition was found for small strain amplitudes. This result is in agreement with observations in the literature and can be attributed to the coupling of phonons to the ferroelastic soft mode describing the transition. For very high excitation fluences, when the unit cells are compressed beyond their tetragonal distortion, an even larger softening was observed and attributed to the coupling of phonons to ferroelastic domain walls. I proposed a new mechanism that enables the coupling of the high amplitude GHz strain waves to the ferroelastic domain walls. This conclusion was strongly supported by experiments on samples with two different transducer materials. These lead to different domain configurations in SrTiO_3 in the vicinity of the interface.

Phonon attenuation in SrTiO_3 was investigated across a wide temperature range and a steep increase of the attenuation was found at the phase transition. A comparison to the results obtained for frequency resolved measurements conducted by a collaborating research group show that highly excited coherent phonons display the same attenuation increase as thermal phonons at the phase transition. The two different transducer materials also influence the damping rate observed at low temperatures. Time resolved Brillouin scattering gives access to the damping rate of phonons close to the interface, where the domain configuration is determined by the transducer layers. In these measurements, elastic domain wall scattering was found to be dominant. The frequency resolved technique is sensitive to the bulk of the material, where the scattering of phonons from domain walls does not yield a significant contribution.

In preliminary experiments on magnetic multilayers, I have studied the fluence dependent demagnetisation in a $(\text{La,Sr})\text{MnO}_3/(\text{Pb,Zi})\text{TiO}_3$ sample. I found that observed temperature dependent signatures of the phase transition strongly depend on the excitation fluence. Features that suggest a magneto-elastic coupling were observed in some of the investigated multilayered samples. The measured sound

velocity in a (La,Sr)MnO₃-(Ba,Sr)TiO₃ heterostructure displays a pronounced temperature dependence, displaying a hardening towards low temperatures. A structural phase transition in (Ba,Sr)TiO₃ is held responsible for an observed anomaly at $T \approx 200$ K.

On the basis of the presented results, I propose several directions for future experiments. For a better understanding of the complex domain dynamics in SrTiO₃, time resolved high resolution x-ray diffraction measurements at low temperatures might give further insight into the microscopic mechanism of the domain wall motion in SrTiO₃ and the temporal evolution of the strain pulse. Simulations, e.g. molecular dynamics calculations based on our results may yield a better understanding of the microscopic mechanism.

Exploiting the high flexibility of time resolved Brillouin scattering, the damping mechanisms dominant at various temperature regimes in SrTiO₃ could be studied over a wider frequency range. Phonon modes closer to the Brillouin zone edge that are subject to Umklapp scattering can thus be studied. An extension of the observable range can be achieved by the application of suitable films for the generation and detection processes: the frequency of the generated or detected phonons can be appropriately selected and thin metal detector films can be applied to study the spectral evolution of the strain pulse after a certain propagation distance. Shaping the excitation light pulse, a strain pulse pattern can be formed.

Detailed studies on the anharmonic coupling of phonons and the possible generation of higher harmonics are currently being performed. Other media with high lattice anharmonicity such as sapphire or DyScO₃ are suitable for the study of non-linear sound propagation and the formation of solitons [Mus02].

For an in-depth understanding of the demagnetisation process in manganites, simultaneous time resolved measurements of the reflectivity and transmission can be performed in the mid-infrared in order to obtain the time dependent complex optical conductivity. This way, the temporal evolution of the polaron peak in the spectrum can be studied, yielding information about the interplay between charge, lattice and magnetisation dynamics in the material. This may elucidate the origin of the slow demagnetisation in manganites. The measurements on the ferroic multilayers can be the starting point for studying the selective coupling of ferroic order in more detail. The possibility of the magneto-elastic coupling in superlattices can be further exploited. Measurements with an externally applied magnetic field, currently being established in our group, can give a more reliable interpretation of the observed oscillations. Measuring the magneto-optical Kerr rotation angle will give further understanding about the coherent magnon oscillations.

Bibliography

- [Akh39] A. Akhieser, On the absorption of sound in solids, *J. Phys. (USSR)*, **1**, 277, 1939.
- [Ani74] S. I. Anisimov, Electron emission from metal surfaces exposed to ultrashort laser pulses, *Sov. Phys. JETP*, **39**, 375–377, 1974.
- [Arz00] L. Arzel, B. Hehlen, R. Currat, B. Hennion, and E. Courtens, The effect of domains on spectral anomalies of SrTiO₃ below the structural transition, *Ferroelectrics*, **236**, 81–92, 2000.
- [Arz03] L. Arzel, B. Hehlen, F. Dénoyer, R. Currat, K.-D. Liss, and E. Courtens, Observation of a sample-dependent 37 K anomaly on the lattice parameters of strontium titanate, *Europhysics Letters (EPL)*, **61**(5), 653–659, 2003.
- [Ave02] R. D. Averitt and A. J. Taylor, Ultrafast optical and far-infrared quasi-particle dynamics in correlated electron materials, *Journal of Physics: Condensed Matter*, **14**, R1357, 2002.
- [Böm60] H. E. Bömmel and K. Dransfeld, Excitation and attenuation of hypersonic waves in quartz, *Physical Review*, **226**(5), 1960.
- [Bar98] A. Bartels, T. Dekorsy, H. Kurz, and K. Köhler, Coherent control of acoustic phonons in semiconductor superlattices, *Applied Physics Letters*, **72**(22), 2844, 1998.
- [Bar99] A. Bartels, T. Dekorsy, H. Kurz, and K. Köhler, Coherent Zone-Folded Longitudinal Acoustic Phonons in Semiconductor Superlattices: Excitation and Detection, *Physical Review Letters*, **82**(5), 1044–1047, 1999.
- [Bar04] M. Bargheer, N. Zhavoronkov, Y. Gritsai, J. C. Woo, D. S. Kim, M. Woerner, and T. Elsaesser, Coherent Atomic Motions in a Nanostructure Studied by Femtosecond X-ray Diffraction, *Science*, **306**(5702), 1771–1773, 2004.
- [Bea96] E. Beaupaire, J. C. Merle, A. Daunois, and J. Y. Bigot, Ultrafast Spin Dynamics in Ferromagnetic Nickel, *Phys. Rev. Lett.*, **76**(22), 4250–4253, 1996.
- [Bea02] M. C. Beard, G. M. Turner, and C. A. Schmuttenmaer, Terahertz Spectroscopy, *The Journal of Physical Chemistry B*, **106**(29), 7146–7159, 2002.
- [Bel63] R. O. Bell and G. Rupprecht, Elastic Constants of Strontium Titanate, *Phys. Rev.*, **129**(1), 90–94, 1963.

-
- [Ber69] B. Berre, K. Fossheim, and K. A. Müller, Critical Attenuation of Sound by Soft Modes in SrTiO₃, *Physical Review Letters*, **23**(11), 589–591, 1969.
- [Ber05] G. P. Berman and F. M. Izrailev, The Fermi-Pasta-Ulam problem: fifty years of progress., *Chaos (Woodbury, N.Y.)*, **15**(1), 15104, 2005.
- [Boj12a] A. Bojahr, M. Herzog, D. Schick, I. Vrejoiu, and M. Bargheer, Calibrated real-time detection of nonlinearly propagating strain waves, *Phys. Rev. B*, **86**(14), 144306, 2012.
- [Boj12b] A. Bojahr, D. Schick, L. Maerten, M. Herzog, I. Vrejoiu, C. von Korff Schmising, C. J. Milne, S. L. Johnson, and M. Bargheer, Comparing the oscillation phase in optical pump-probe spectra to ultrafast x-ray diffraction in the metal-dielectric SrRuO₃/SrTiO₃ superlattice, *Physical Review B*, **85**(22), 224302, 2012.
- [Boj13] A. Bojahr, M. Herzog, S. Mitzscherling, L. Maerten, D. Schick, J. Goldshteyn, W. Leitenberger, R. Shayduk, P. Gaal, and M. Bargheer, Brillouin scattering of visible and hard X-ray photons from optically synthesized phonon wavepackets, *Opt. Express*, **21**(18), 21188–21197, 2013.
- [Bom12] M. Bombeck, a. S. Salasyuk, B. a. Glavin, a. V. Scherbakov, C. Brüggemann, D. R. Yakovlev, V. F. Sapega, X. Liu, J. K. Furdyna, a. V. Akimov, and M. Bayer, Excitation of spin waves in ferromagnetic (Ga,Mn)As layers by picosecond strain pulses, *Physical Review B*, **85**(19), 195324, 2012.
- [Bra09] M. Bradler, P. Baum, and E. Riedle, Femtosecond continuum generation in bulk laser host materials with sub- μ J pump pulses, *Applied Physics B*, **97**(3), 561, 2009.
- [Bro99] A. Brodeur and S. L. Chin, Ultrafast white-light continuum generation and self-focusing in transparent condensed media, *JOSA B*, **16**(4), 637, 1999.
- [Buc99] A. Buckley, J. P. Rivera, and E. K. H. Salje, Twin structures in tetragonal SrTiO₃: The ferroelastic phase transition and the formation of needle domains, *Journal of Applied Physics*, **86**(3), 1653, 1999.
- [Cao11] J. Cao and J. Wu, Strain effects in low-dimensional transition metal oxides, *Materials Science and Engineering: R: Reports*, **71**(2-4), 35–52, 2011.
- [Car61] P. Carruthers, Theory of Thermal Conductivity of Solids at Low Temperatures, *Reviews of Modern Physics*, **33**(1), 92–138, 1961.
- [Car07] M. A. Carpenter, Elastic anomalies accompanying phase transitions in (Ca,Sr)TiO₃ perovskites: Part I. Landau theory and a calibration for SrTiO₃, *American Mineralogist*, **92**(2-3), 309, 2007.

-
- [Cha70] T. S. Chang, J. F. Holzrichter, G. F. Imbusch, and A. L. Schawlow, Direct Observation of Single-Domain SrTiO₃, *Applied Physics Letters*, **17**(6), 254, 1970.
- [Cha93] K. Chahara, T. Ohno, M. Kasai, and Y. Kozono, Magnetoresistance in magnetic manganese oxide with intrinsic antiferromagnetic spin structure, *Applied Physics Letters*, **63**(14), 1990–1992, 1993.
- [Che06] J. Chen, D. Tzou, and J. Beraun, A semiclassical two-temperature model for ultrafast laser heating, *International Journal of Heat and Mass Transfer*, **49**(1-2), 307–316, 2006.
- [Chr98] J. Chrosch and E. K. H. Salje, Near-surface domain structures in uniaxially stressed SrTiO₃, *Journal of Condensed Matter*, **10**(13), 2817, 1998.
- [Col80] C. Colvard, R. Merlin, M. V. Klein, and A. C. Gossard, Observation of folded acoustic phonons in a semiconductor superlattice, *Physical Review Letters*, **45**(4), 298–301, 1980.
- [Cou93] E. Courtens, G. Coddens, B. Hennion, B. Hehlen, J. Pelous, and R. Vacher, Phonon anomalies in SrTiO₃ in the quantum paraelectric regime, *Physica Scripta*, **T49B**, 430–435, 1993.
- [Dag01] E. Dagotto, T. Hotta, and A. Moreo, Colossal magnetoresistant materials: the key role of phase separation, *Physics Reports*, **344**, 1–153, 2001.
- [Dag08] E. Dagotto and Y. Tokura, Strongly correlated electronic materials: present and future, *MRS bulletin*, **33**(November), 1037–1045, 2008.
- [Dal09] B. C. Daly, Picosecond ultrasonic measurements of attenuation of longitudinal acoustic phonons in silicon, *Physical Review B*, **80**(17), 174112, 2009.
- [deL96] de Ligny D. and P. Richet, High-temperature heat capacity and thermal expansion of SrTiO₃ and SrZrO₃ perovskites, *Physical review. B, Condensed matter*, **53**(6), 3013–3022, 1996.
- [Dem10] W. Demtröder, *Experimentalphysik 3*, Springer-Lehrbuch, Springer Berlin Heidelberg, Berlin, Heidelberg, 2010.
- [Dur08] A. Durán, F. Morales, L. Fuentes, and J. M. Siqueiros, Specific heat anomalies at 37, 105 and 455 K in SrTiO₃:Pr, *Journal of Physics: Condensed Matter*, **20**(8), 085219, 2008.
- [Eom92] C. B. Eom, R. J. Cava, R. M. Fleming, J. M. Phillips, R. B. VanDover, J. H. Marshall, J. W. P. Hsu, J. J. Krajewski, and J. Peck, W. F., Single-Crystal Epitaxial Thin Films of the Isotropic Metallic Oxides Sr_{1-x}Ca_xRuO₃ ($0 \leq x \leq 1$), *Science*, **258**(5089), 1766–1769, 1992.

-
- [För11] M. Först, C. Manzoni, S. Kaiser, Y. Tomioka, Y. Tokura, R. Merlin, and A. Cavalleri, Nonlinear phononics as an ultrafast route to lattice control, *Nature Physics*, **7**(11), 854–856, 2011.
- [Fan61] U. Fano, Effects of Configuration Interaction on Intensities and Phase Shifts, *Physical Review*, **124**(6), 1866–1878, 1961.
- [Fis93] G. J. Fischer, Z. Wang, and S.-i. Karato, Elasticity of CaTiO_3 , SrTiO_3 and BaTiO_3 perovskites up to 3.0 GPa: the effect of crystallographic structure, *Physics and Chemistry of Minerals*, **20**(2), 97–103, 1993.
- [Fle71] P. A. Fleury, Phonon Instabilities and Interactions near Solid-State Phase Transitions, *The Journal of the Acoustical Society of America*, **49**(3C), 1041, 1971.
- [Fle76] P. A. Fleury, The effects of soft modes on the structure and properties of materials, *Annual Review of Materials Science*, **6**, 157, 1976.
- [Fli10] T. Fliessbach, *Statistische Physik*, Spektrum Akademischer Verlag, Heidelberg, 2010.
- [Fos72] K. Fossheim and B. Berre, Ultrasonic Propagation, Stress Effects, and Interaction Parameters at the Displacive Transition in SrTiO_3 , *Physical Review B*, **5**(8), 3292–3308, 1972.
- [Fos85] J. O. Fossum and K. Fossheim, Measurements of ultrasonic attenuation and velocity in Verneuil-grown and flux-grown SrTiO_3 , *Journal of Physics C: Solid State*, **18**, 5549, 1985.
- [Gol26] V. M. Goldschmidt, Die Gesetze der Krystallochemie, *Naturwissenschaften*, **14**(21), 477, 1926.
- [Gol14a] J. Goldshteyn, A. Bojahr, P. Gaal, D. Schick, and M. Bargheer, Selective preparation and detection of phonon polariton wavepackets by stimulated Raman scattering, *physica status solidi (b)*, **251**(4), 821–828, 2014.
- [Gol14b] J. Goldshteyn, *Frequency-Resolved Ultrafast Dynamics of Phonon Polariton Wavepackets in the Ferroelectric Crystals LiNbO_3 and LiTaO_3* , Dissertation, University of Potsdam, 2014.
- [Gue10] M. Guennou, P. Bouvier, J. Kreisel, and D. Machon, Pressure-temperature phase diagram of SrTiO_3 up to 53 GPa, *Physical Review B*, **81**(5), 054115, 2010.
- [Hac10] A. Hachemi, H. Hachemi, A. Ferhat-Hamida, and L. Louail, Elasticity of SrTiO_3 perovskite under high pressure in cubic, tetragonal and orthorhombic phases, *Physica Scripta*, **82**(2), 25602, 2010.

-
- [Har04] R. J. Harrison, S. A. T. Redfern, and E. K. H. Salje, Dynamical excitation and anelastic relaxation of ferroelastic domain walls in LaAlO_3 , *Phys. Rev. B*, **69**(14), 144101, 2004.
- [Heh95] B. Hehlen, A.-L. Pérou, E. Courtens, and R. Vacher, Observation of a Doublet in the Quasielastic Central Peak of Quantum-Paraelectric SrTiO_3 , *Physical Review Letters*, **75**(12), 2416–2419, 1995.
- [Heh96] B. Hehlen, Z. Kallassy, and E. Courtens, The high-frequency elastic constants of SrTiO_3 in the quantum paraelectric regime, *Ferroelectrics*, **183**, 265–272, 1996.
- [Her10] M. Herzog, W. Leitenberger, R. Shayduk, R. M. van der Veen, C. J. Milne, S. L. Johnson, I. Vrejoiu, M. Alexe, D. Hesse, and M. Bargheer, Ultrafast manipulation of hard x-rays by efficient Bragg switches, *Applied Physics Letters*, **96**(16), 161906, 2010.
- [Her11] M. Herzog, D. Schick, P. Gaal, R. Shayduk, C. K. Schmising, M. Bargheer, and C. Korff Schmising, Analysis of ultrafast X-ray diffraction data in a linear-chain model of the lattice dynamics, *Applied Physics A*, **106**(3), 489–499, 2011.
- [Her12a] M. Herzog, A. Bojahr, J. Goldshteyn, W. Leitenberger, I. Vrejoiu, D. Khakhulin, M. Wulff, R. Shayduk, P. Gaal, and M. Bargheer, Detecting optically synthesized quasi-monochromatic sub-terahertz phonon wavepackets by ultrafast x-ray diffraction, *Applied Physics Letters*, **100**(9), 094101, 2012.
- [Her12b] M. Herzog, *Structural Dynamics of Photoexcited Nanolayered Perovskites Studied by Ultrafast X-ray Diffraction*, Dissertation, 2012.
- [Her12c] M. Herzog, D. Schick, W. Leitenberger, R. Shayduk, R. M. V. D. Veen, C. J. Milne, S. L. Johnson, I. Vrejoiu, and M. Bargheer, Tailoring interference and nonlinear manipulation of femtosecond x-rays, *New Journal of Physics*, **14**(1), 013004, 2012.
- [Hir05] Y. Hirobe, Y. Kubo, K. Kouyama, H. Kunugita, K. Ema, and H. Kuwahara, Transient differential reflectivity of ferromagnetic and paramagnetic phases in the bilayered manganite $\text{La}_{1.24}\text{Sr}_{1.76}\text{Mn}_2\text{O}_7$, *Solid State Communications*, **133**(7), 449–453, 2005.
- [Hon13] M. Honig, J. A. Sulpizio, J. Drori, A. Joshua, E. Zeldov, and S. Ilani, Local electrostatic imaging of striped domain order in $\text{LaAlO}_3/\text{SrTiO}_3$, *Nature materials*, **12**(12), 1112–8, 2013.
- [Hub98] A. Hubert and R. Schäfer, *Magnetic Domains: The Analysis of Magnetic Microstructures*, Springer, 1998.

- [Hun07] S. Hunklinger, *Festkörperphysik*, Oldenbourg, 2007.
- [Huy06] A. Huynh, N. Lanzillotti-Kimura, B. Jusserand, B. Perrin, A. Fainstein, M. Pascual-Winter, E. Peronne, and A. Lemaître, Subterahertz Phonon Dynamics in Acoustic Nanocavities, *Physical Review Letters*, **97**(11), 115502, 2006.
- [Huy08] A. Huynh, B. Perrin, N. Lanzillotti-Kimura, B. Jusserand, A. Fainstein, and A. Lemaître, Subterahertz monochromatic acoustic wave propagation using semiconductor superlattices as transducers, *Physical Review B*, **78**(23), 233302, 2008.
- [Izy07] N. Izyumskaya, Y. I. Alivov, S. J. Cho, H. Morkoç, H. Lee, and Y. S. Kang, Processing, Structure, Properties, and Applications of PZT Thin Films, *Critical Reviews in Solid State and Materials Sciences*, **32**(3), 111–202, 2007.
- [Jin94] S. Jin, T. H. Tiefel, M. McCormack, R. A. Fastnacht, R. Ramesh, and L. H. Chen, Thousandfold Change in Resistivity in Magnetoresistive La-Ca-Mn-O Films, *Science*, **264**(5157), 413–415, 1994.
- [Jus86] B. Jusserand, F. Alexandre, J. Dubard, and D. Paquet, Raman scattering study of acoustical zone-center gaps in GaAs/AlAs superlattices, *Physical Review B*, **33**(4), 2897–2899, 1986.
- [Jus87] B. Jusserand, D. Paquet, F. Molloy, F. Alexandre, and G. Le Roux, Influence of the supercell structure on the folded acoustical Raman line intensities in superlattices, *Physical Review B*, **35**(6), 2808–2817, 1987.
- [Kai66] W. Kaiser and R. Zurek, Brillouin- and critical light scattering in SrTiO₃-crystals, *Physics Letters*, **23**(11), 668, 1966.
- [Kal13] B. Kalisky, E. M. Spanton, H. Noad, J. R. Kirtley, K. C. Nowack, C. Bell, H. K. Sato, M. Hosoda, Y. Xie, Y. Hikita, C. Woltmann, G. Pfanzelt, R. Jany, C. Richter, H. Y. Hwang, J. Mannhart, and K. A. Moler, Locally enhanced conductivity due to the tetragonal domain structure in LaAlO₃/SrTiO₃ heterointerfaces., *Nature materials*, **12**(12), 1091–5, 2013.
- [Kap99] T. A. Kaplan and S. D. Mahanti, *Physics of Manganites*, 1999.
- [Kel67] K. R. Keller, Ultrasonic Attenuation in Ge-Si Alloys, *Journal of Applied Physics*, **38**(9), 3777, 1967.
- [Khl00] M. N. Khlopkin, G. K. Panova, A. A. Shikov, V. F. Sinyavskii, and D. A. Shulyatev, Heat capacity of La_{1-x}Sr_xMnO₃ single crystals in different magnetic states, *Physics of the Solid State*, **42**(1), 114–119, 2000.

-
- [Kia96] J. M. Kiat and T. Roisnel, Rietveld analysis of strontium titanate in the Müller state, *Journal of Physics: Condensed Matter*, **3471**, 1996.
- [Kir10] A. Kirilyuk, A. V. Kimel, and T. Rasing, Ultrafast optical manipulation of magnetic order, *Rev. Mod. Phys.*, **82**(3), 2731–2784, 2010.
- [Kis00] T. Kise, T. Ogasawara, M. Ashida, Y. Tomioka, Y. Tokura, and M. Kuwata-Gonokami, Ultrafast Spin Dynamics and Critical Behavior in Half-Metallic Ferromagnet: Sr₂FeMoO₆, *Phys. Rev. Lett.*, **85**(9), 1986–1989, 2000.
- [Kit00] A. V. Kityk, W. Schranz, P. Sondergeld, D. Havlik, E. K. H. Salje, and J. F. Scott, Low-frequency superelasticity and nonlinear elastic behavior of SrTiO₃ crystals, *Physical Review B*, **61**(2), 946–956, 2000.
- [Kiy96] T. Kiyama, K. Yoshimura, K. Kosuge, Y. Ikeda, and Y. Bando, Invar effect of SrRuO₃: Itinerant electron magnetism of Ru 4d electrons., *Physical Review B, Condensed matter*, **54**(2), R756–R759, 1996.
- [Kle94] P. G. Klemens, Phonon scattering and thermal resistance due to grain boundaries, *International Journal of Thermophysics*, **15**(6), 1345–1351, 1994.
- [Kle02] R. Kleiner and D. Kölle, Vorlesungsskript Festkörperphysik, Kapitel V - Magnetismus, in *Vorlesungsskript Physikalisches Institut Universität Tübingen*, 2002.
- [Ko08] J.-H. Ko, S. Kojima, T.-Y. Koo, J. H. Jung, C. J. Won, and N. J. Hur, Elastic softening and central peaks in BaTiO₃ single crystals above the cubic-tetragonal phase-transition temperature, *Applied Physics Letters*, **93**(10), 102905, 2008.
- [Koh06] T. Kohmoto, K. Tada, T. Moriyasu, and Y. Fukuda, Observation of coherent phonons in strontium titanate: Structural phase transition and ultrafast dynamics of the soft modes, *Phys. Rev. B*, **74**(6), 64303, 2006.
- [Kor06] A. Koreeda, T. Nagano, S. Ohno, and S. Saikan, Quasielastic light scattering in rutile, ZnSe, silicon, and SrTiO₃, *Physical Review B*, **73**(2), 024303, 2006.
- [Kor07] A. Koreeda, R. Takano, and S. Saikan, Second sound in SrTiO₃, *Physical Review Letters*, **99**(26), 265502, 2007.
- [Kor08] C. V. Korff Schmising, A. Harpoeth, N. Zhavoronkov, Z. Ansari, C. Akuleh, M. Woerner, T. Elsaesser, M. Bargheer, M. Schmidbauer, I. Vrejoiu, D. Hesse, and M. Alexe, Ultrafast magnetostriction and phonon-mediated stress in a photoexcited ferromagnet, *Physical Review B*, **78**(6), 60404, 2008.

- [Kor11] A. Koreeda and S. Saikan, Note: Higher resolution Brillouin spectroscopy by offset stabilization of a tandem Fabry-Pérot interferometer., *The Review of scientific instruments*, **82**(12), 126103, 2011.
- [Kor14a] A. Koreeda, Private Communication, 2014.
- [Kor14b] C. Korff Schmising, B. Pfau, M. Schneider, C. M. Günther, M. Giovannella, J. Perron, B. Vodungbo, L. Müller, F. Capotondi, E. Pedersoli, N. Mahne, J. Lüning, and S. Eisebitt, Imaging Ultrafast Demagnetization Dynamics after a Spatially Localized Optical Excitation, *Physical Review Letters*, **112**(21), 217203, 2014.
- [Kre71] E. Kretschmann, Die bestimmung optischer konstanten von metallen durch anregung von oberflächenplasmaschwingungen, *Zeitschrift für Physik*, **24**(17), 1639–41, 1971.
- [Lan37] L. D. Landau and G. Rumer, On the absorption of sound in solids, *Phys. Z. Sowjetunion*, **11**, 18, 1937.
- [Lem96] V. V. Lemanov, E. P. Smirnova, P. P. Syrnikov, and E. A. Tarakanov, Phase transitions and glasslike behavior in $\text{Sr}_{1-x}\text{Ba}_x\text{TiO}_3$, *Physical Review B*, **54**(5), 3151, 1996.
- [Lin08] Z. Lin, L. Zhigilei, and V. Celli, Electron-phonon coupling and electron heat capacity of metals under conditions of strong electron-phonon nonequilibrium, *Physical Review B*, **77**(7), 075133, 2008.
- [Lin11] T. L. Linnik, A. V. Scherbakov, D. R. Yakovlev, X. Liu, J. K. Furdyna, and M. Bayer, Theory of magnetization precession induced by a picosecond strain pulse in ferromagnetic semiconductor (Ga,Mn)As, *Physical Review B*, **84**(21), 214432, 2011.
- [Lis09] S. Lisenkov, I. Ponomareva, and L. Bellaiche, Unusual static and dynamical characteristics of domain evolution in ferroelectric superlattices, *Phys. Rev. B*, **79**(2), 24101, 2009.
- [LK07] N. Lanzillotti-Kimura, A. Fainstein, A. Huynh, B. Perrin, B. Jusserand, A. Miard, and A. Lemaître, Coherent Generation of Acoustic Phonons in an Optical Microcavity, *Physical Review Letters*, **99**(21), 217405, 2007.
- [LK11] N. D. Lanzillotti-Kimura, A. Fainstein, B. Perrin, and B. Jusserand, Theory of coherent generation and detection of THz acoustic phonons using optical microcavities, *Physical Review B*, **84**(6), 064307, 2011.
- [Lob00a] A. I. Lobad, R. D. Averitt, C. Kwon, and A. J. Taylor, Spin-lattice interaction in colossal magnetoresistance manganites, *Applied Physics Letters*, **77**(24), 4025–4027, 2000.

-
- [Lob00b] A. I. Lobad, A. J. Taylor, C. Kwon, S. A. Trugman, and T. R. Gosnell, Laser induced dynamic spectral weight transfer in $\text{La}_{0.7}\text{Ca}_{0.3}\text{MnO}_3$, *Chemical Physics*, **251**(1–3), 227–236, 2000.
- [Loe10] R. Loetzsch, A. Lübcke, I. Uschmann, E. Foerster, V. Grosse, M. Thuerk, T. Koettig, F. Schmidl, and P. Seidel, The cubic to tetragonal phase transition in SrTiO_3 single crystals near its surface under internal and external strains, *Applied Physics Letters*, **96**(7), 71901, 2010.
- [Lyt64] F. W. Lytle, X-Ray Diffractometry of Low-Temperature Phase Transformations in Strontium Titanate, *Journal of Applied Physics*, **35**(7), 2212, 1964.
- [Mül68] K. A. Müller, W. Berlinger, and F. Waldner, Characteristic structural phase transition in perovskite-type compounds, *Physical Review Letters*, **21**(12), 1968.
- [Mül74] K. A. Müller, Critical phenomena near structural phase transitions studied by EPR, *Ferroelectrics*, **7**(1), 17–21, 1974.
- [Mül79] K. A. Müller and H. Burkard, SrTiO_3 : An intrinsic quantum paraelectric below 4 K, *Physical Review B*, **19**(7), 3593–3602, 1979.
- [Mül91] K. A. Müller, W. Berlinger, and E. Tosatti, Indication for a novel phase in the quantum paraelectric regime of SrTiO_3 , *Zeitschrift für Physik B*, **84**, 277–283, 1991.
- [Ma11] J. Ma, J. Hu, Z. Li, and C.-W. Nan, Recent progress in multiferroic magnetoelectric composites: from bulk to thin films, *Advanced materials*, **23**(9), 1062–87, 2011.
- [Ma13] J. Ma, B. R. Parajuli, M. G. Ghossoub, A. Mihi, J. Sadhu, P. V. Braun, and S. Sinha, Coherent phonon-grain boundary scattering in silicon inverse opals., *Nano letters*, **13**(2), 618–24, 2013.
- [Mal13] M. Maldovan, Sound and heat revolutions in phononics, *Nature*, **503**(7475), 209–17, 2013.
- [Mar68] H. J. Maris, Ultrasonic attenuation in dirty dielectric crystals, *Physical Review*, **175**(3), 1077, 1968.
- [Mar71] H. J. Maris, *Interaction of Sound Waves with Thermal Phonons in Dielectric Crystals*, volume 8 of *Physical Acoustics*, Academic Press, 1971.
- [Mar96] M. C. Martin, G. Shirane, Y. Endoh, K. Hirota, Y. Moritomo, and Y. Tokura, Magnetism and structural distortion in the $\text{La}_{0.7}\text{Sr}_{0.3}\text{MnO}_3$ metallic ferromagnet, *Phys. Rev. B*, **53**(21), 14285–14290, 1996.

-
- [Mar12] R. Martínez, A. Kumar, R. Palai, G. Srinivasan, and R. S. Katiyar, Observation of strong magnetoelectric effects in $\text{Ba}_{0.7}\text{Sr}_{0.3}\text{TiO}_3/\text{La}_{0.7}\text{Sr}_{0.3}\text{MnO}_3$ thin film heterostructures, *Journal of Applied Physics*, **111**(10), 104104, 2012.
- [Mat02] O. Matsuda and O. B. Wright, Reflection and transmission of light in multilayers perturbed by picosecond strain pulse propagation, *Journal of the Optical Society of America B*, **19**(12), 3028, 2002.
- [Maz13] A. A. Maznev, F. Hofmann, A. Jandl, K. Esfarjani, M. T. Bulsara, E. A. Fitzgerald, G. Chen, and K. A. Nelson, Lifetime of sub-THz coherent acoustic phonons in a GaAs-AlAs superlattice, *Applied Physics Letters*, **102**(4), 041901, 2013.
- [Miz99] K. Mizoguchi, M. Hase, S. Nakashima, and M. Nakayama, Observation of coherent folded acoustic phonons propagating in a GaAs/AlAs superlattice by two-color pump-probe spectroscopy, *Physical Review B*, **60**(11), 8262–8266, 1999.
- [Mou86] P. F. Moulton, Spectroscopic and laser characteristics of $\text{Ti}:\text{Al}_2\text{O}_3$, *Journal of the Optical Society of America B*, **3**(1), 125, 1986.
- [Mus02] O. L. Muskens and J. I. Dijkhuis, High Amplitude, Ultrashort, Longitudinal Strain Solitons in Sapphire, *Physical Review Letters*, **89**(28), 285504, 2002.
- [Nag12] A. Nagakubo, A. Yamamoto, K. Tanigaki, H. Ogi, N. Nakamura, and M. Hirao, Monitoring of Longitudinal-Wave Velocity and Attenuation of SrTiO_3 at Low Temperatures Using Picosecond Ultrasound Spectroscopy, *Japanese Journal of Applied Physics*, **51**, 07GA09, 2012.
- [Nat99] T. K. Nath, R. a. Rao, D. Lavric, C. B. Eom, L. Wu, and F. Tsui, Effect of three-dimensional strain states on magnetic anisotropy of $\text{La}_{0.8}\text{Ca}_{0.2}\text{MnO}_3$ epitaxial thin films, *Applied Physics Letters*, **74**(11), 1615, 1999.
- [Nav69] R. Nava, R. Callarotti, H. Ceva, and A. Martinet, Hypersonic Attenuation by Low-Frequency Optical Phonons in SrTiO_3 Crystals, *Phys. Rev.*, **188**(3), 1456–1464, 1969.
- [Nes92] O. M. Nes and K. A. Müller, Elastic anomalies in the quantum paraelectric regime of SrTiO_3 , *Europhysics Letters*, **397**, 1992.
- [Nov10] L. Novotny, Strong coupling, energy splitting, and level crossings: A classical perspective, *American Journal of Physics*, **78**(11), 1199, 2010.
- [Oga05] T. Ogasawara, K. Ohgushi, Y. Tomioka, K. S. Takahashi, H. Okamoto, M. Kawasaki, and Y. Tokura, General Features of Photoinduced Spin

- Dynamics in Ferromagnetic and Ferrimagnetic Compounds, *Phys. Rev. Lett.*, **94**(8), 87202, 2005.
- [Oki95] Y. Okimoto, T. Katsufuji, T. Ishikawa, A. Urushibara, T. Arima, and Y. Tokura, Anomalous Variation of Optical Spectra with Spin Polarization in Double-Exchange Ferromagnet: $\text{La}_{1-x}\text{Sr}_x\text{MnO}_3$, *Phys. Rev. Lett.*, **75**(1), 109–112, 1995.
- [Oki97] Y. Okimoto, T. Katsufuji, T. Ishikawa, T. Arima, and Y. Tokura, Variation of electronic structure in $\text{La}_{1-x}\text{Sr}_x\text{MnO}_3$ ($0 \leq x \leq 0.3$) as investigated by optical conductivity spectra, *Phys. Rev. B*, **55**(7), 4206–4214, 1997.
- [Par08] S. S. P. Parkin, M. Hayashi, and L. Thomas, Magnetic domain-wall race-track memory, *Science (New York, N.Y.)*, **320**(5873), 190–4, 2008.
- [Pau01] P. M. Paul, E. S. Toma, P. Breger, G. Mullot, F. Auge, P. Balcou, H. G. Muller, and P. Agostini, Observation of a train of attosecond pulses from high harmonic generation, *Science (New York, N.Y.)*, **292**(5522), 1689–92, 2001.
- [Per11] P. Perna, C. Rodrigo, E. Jiménez, F. J. Teran, N. Mikuszeit, L. Méchin, J. Camarero, and R. Miranda, Tailoring magnetic anisotropy in epitaxial half metallic $\text{La}_{0.7}\text{Sr}_{0.3}\text{MnO}_3$ thin films, *Journal of Applied Physics*, **110**(1), 013919, 2011.
- [PW09] M. F. Pascual-Winter, A. Fainstein, B. Jusserand, B. Perrin, and A. Lemaître, Optimized optical generation and detection of superlattice acoustic phonons, *Applied Physics Letters*, **94**(10), 103103, 2009.
- [PW12] M. F. Pascual-Winter, A. Fainstein, B. Jusserand, B. Perrin, and A. Lemaître, Spectral responses of phonon optical generation and detection in superlattices, *Physical Review B*, **85**(23), 235443, 2012.
- [Pyt69] E. Pytte and J. Feder, Theory of a Structural Phase Transition in Perovskite-Type Crystals, *Physical Review*, **187**(3), 1077–1088, 1969.
- [Pyt70] E. Pytte, Soft-mode damping and ultrasonic attenuation at a structural phase transition, *Physical Review B*, **1**, 924, 1970.
- [Qui98] M. Quijada, J. Černe, J. R. Simpson, H. D. Drew, K. H. Ahn, A. J. Millis, R. Shreekala, R. Ramesh, M. Rajeswari, and T. Venkatesan, Optical conductivity of manganites: Crossover from Jahn-Teller small polaron to coherent transport in the ferromagnetic state, *Phys. Rev. B*, **58**(24), 16093–16102, 1998.
- [Rös13] M. Rössle, C. N. Wang, P. Marsik, M. Yazdi-Rizi, K. W. Kim, a. Dubroka, I. Marozau, C. W. Schneider, J. Humlíček, D. Baeriswyl, and C. Bernhard, Optical probe of ferroelectric order in bulk and thin-film perovskite titanates, *Physical Review B*, **88**(10), 104110, 2013.

- [Ram96] A. P. Ramirez, P. Schiffer, S. W. Cheong, C. H. Chen, W. Bao, T. T. Palstra, P. L. Gammel, D. J. Bishop, and B. Zegarski, Thermodynamic and electron diffraction signatures of charge and spin ordering in $\text{La}_{1-x}\text{Ca}_x\text{MnO}_3$, *Physical review letters*, **76**(17), 3188–3191, 1996.
- [Ran11] C. A. Randall, A. S. Bhalla, T. R. ShROUT, and L. E. Cross, Classification and consequences of complex lead perovskite ferroelectrics with regard to B-site cation order, *Journal of Materials Research*, **5**(04), 829–834, 2011.
- [Reh70a] W. Rehwald, Low temperature elastic moduli of strontium titanate, *Solid State Communications*, **8**, 1483–1485, 1970.
- [Reh70b] W. Rehwald, Anomalous ultrasonic attenuation at the 105 K transition in strontium titanate, *Solid State Communications*, **8**, 607–611, 1970.
- [Reh71] W. Rehwald, Ultrasonic properties of strontium titanate at the 105 K transition, *Physik der kondensierten Materie*, **36**, 21–36, 1971.
- [Ren07] Y. H. Ren, M. Trigo, R. Merlin, V. Adyam, and Q. Li, Generation and detection of coherent longitudinal acoustic phonons in the $\text{La}_{0.67}\text{Sr}_{0.33}\text{MnO}_3$ thin films by femtosecond light pulses, *Applied Physics Letters*, **90**(25), 251918, 2007.
- [Rin07] M. Rini, R. Tobey, N. Dean, J. Itatani, Y. Tomioka, Y. Tokura, R. W. Schoenlein, and A. Cavalleri, Control of the electronic phase of a manganite by mode-selective vibrational excitation, *Nature*, **449**(7158), 72–4, 2007.
- [Ris97] C. Rischel, A. Rousse, and I. Uschmann, Femtosecond time-resolved X-ray diffraction from laser-heated organic films, *Nature*, **390**(December), 490–492, 1997.
- [Rul05] C. Rulliere, *Femtosecond laser pulses*, 2005.
- [Ryt56] S. M. Rytov, Acoustical properties of a thinly laminated medium, *Akust. Zh.*, **2**, 71, 1956.
- [Sal11a] E. K. H. Salje, X. Ding, Z. Zhao, T. Lookman, and A. Saxena, Thermally activated avalanches: Jamming and the progression of needle domains, *Phys. Rev. B*, **83**, 104109, 2011.
- [Sal11b] Z. Salman, M. Smadella, W. A. MacFarlane, B. D. Patterson, P. R. Willmott, K. H. Chow, M. D. Hossain, H. Saadaoui, D. Wang, and R. F. Kiefl, Depth dependence of the structural phase transition of SrTiO_3 studied with β -NMR and grazing incidence x-ray diffraction, *Phys. Rev. B*, **83**(22), 224112, 2011.
- [Sal13a] E. Salje, O. Aktas, M. A. Carpenter, V. Laguta, and J. F. Scott, Domains within Domains and Walls within Walls: Evidence for Polar Domains in Cryogenic SrTiO_3 , *Physical Review Letters*, **111**(24), 247603, 2013.

-
- [Sal13b] E. K. H. Salje, Z. Zhao, X. Ding, and J. Sun, Mechanical spectroscopy in twinned minerals: Simulation of resonance patterns at high frequencies, *American Mineralogist*, **98**(8-9), 1449–1458, 2013.
- [Sch08] D. G. Schlom, L.-Q. Chen, X. Pan, A. Schmehl, and M. a. Zurbuchen, A Thin Film Approach to Engineering Functionality into Oxides, *Journal of the American Ceramic Society*, **91**(8), 2429–2454, 2008.
- [Sch10] A. V. Scherbakov, A. S. Salasyuk, A. V. Akimov, X. Liu, M. Bombeck, C. Brüggemann, D. R. Yakovlev, V. F. Sapega, J. K. Furdyna, and M. Bayer, Coherent Magnetization Precession in Ferromagnetic (Ga,Mn)As Induced by Picosecond Acoustic Pulses, *Physical Review Letters*, **105**(11), 117204, 2010.
- [Sch11] W. Schranz, Superelastic softening in perovskites, *Phys. Rev. B*, **83**(9), 094120, 2011.
- [Sch12a] D. Schick, A. Bojahr, M. Herzog, C. von Korff Schmising, R. Shayduk, W. Leitenberger, P. Gaal, and M. Bargheer, Normalization schemes for ultrafast x-ray diffraction using a table-top laser-driven plasma source, *The Review of scientific instruments*, **83**(2), 025104, 2012.
- [Sch12b] W. Schranz, H. Kabelka, and A. Tröster, Superelastic Softening of Ferroelastic Multidomain Crystals, *Ferroelectrics*, **426**(1), 242–250, 2012.
- [Sch13a] D. Schick, A. Bojahr, M. Herzog, P. Gaal, I. Vrejoiu, and M. Bargheer, Following Strain-Induced Mosaicity Changes of Ferroelectric Thin Films by Ultrafast Reciprocal Space Mapping, *Phys. Rev. Lett.*, **110**, 095502, 2013.
- [Sch13b] D. Schick, *Ultrafast Lattice Dynamics in Photoexcited Nanostructures - Femtosecond X-ray Diffraction with Optimized Evaluation Schemes*, Dissertation, University of Potsdam, 2013.
- [Sch14a] D. Schick, A. Bojahr, M. Herzog, C. von Korff Schmising, R. Shayduk, and M. Bargheer, udkm1Dsim - A Simulation Toolkit for 1D Ultrafast Dynamics in Condensed Matter, *Comput. Phys. Commun.*, **185**(2), 651–660, 2014.
- [Sch14b] D. Schick, M. Herzog, A. Bojahr, W. Leitenberger, A. Hertwig, R. Shayduk, and M. Bargheer, Ultrafast lattice response of photoexcited thin films studied by X-ray diffraction, *Structural Dynamics*, **1**(6), 064501, 2014.
- [Sco74] J. F. Scott, Soft-mode spectroscopy: Experimental studies of structural phase transitions, *Reviews of Modern Physics*, **46**(1), 83–128, 1974.
- [Sco95] J. F. Scott, Interpretation of phonon anomalies in SrTiO₃ near 37K, *Ferroelectrics Letters Section*, **20**(3-4), 89–95, 1995.

- [Sco12] J. F. Scott, E. K. H. Salje, and M. A. Carpenter, Domain Wall Damping and Elastic Softening in SrTiO₃: Evidence for Polar Twin Walls, *Physical Review Letters*, **109**(18), 187601, 2012.
- [Ser02] R. F. Service, Battle to become the next-generation x-ray source, *Science (New York, N.Y.)*, **298**(5597), 1356–8, 2002.
- [Sha13] R. Shayduk, M. Herzog, A. Bojahr, D. Schick, P. Gaal, W. Leitenberger, H. Navirian, M. Sander, J. Goldshteyn, I. Vrejoiu, and M. Bargheer, Direct time-domain sampling of subterahertz coherent acoustic phonon spectra in SrTiO₃ using ultrafast x-ray diffraction, *Physical Review B*, **87**(18), 184301, 2013.
- [Shi69] G. Shirane and Y. Yamada, Lattice-Dynamical Study of the 110°K Phase Transition in SrTiO₃, *Phys. Rev.*, **177**(2), 858–863, 1969.
- [Shi06] V. Shirokov, V. Torgashev, A. Bakirov, and V. Lemanov, Concentration phase diagram of Ba_xSr_{1-x}TiO₃ solid solutions, *Physical Review B*, **73**(10), 104116, 2006.
- [Shi09] V. Shirokov, Y. Yuzyuk, B. Dkhil, and V. Lemanov, Phenomenological theory of phase transitions in epitaxial Ba_xSr_{1-x}TiO₃ thin films, *Physical Review B*, **79**(14), 144118, 2009.
- [Slo70] J. Slonczewski and H. Thomas, Interaction of Elastic Strain with the Structural Transition of Strontium Titanate, *Physical Review B*, **1**(9), 3599–3608, 1970.
- [Sor69] G. Sorge and E. Hegenbarth, The Temperature Dependence of the Elastic Compliance s_{11}^E of SrTiO₃ Single Crystals in the Temperature Range 20 to 45°K, *physica status solidi (b)*, **33**(2), K79–K81, 1969.
- [Stö06] J. Stöhr and H. Siegmann, *Magnetism: From Fundamentals to Nanoscale Dynamics*, Springer, 2006.
- [Sti95] A. Stingl, R. Szipöcs, M. Lenzner, C. Spielmann, and F. Krausz, Sub-10-fs mirror-dispersion-controlled Ti:sapphire laser, *Opt. Lett.*, **20**(6), 602–604, 1995.
- [Sto04] A. Stolow, A. E. Bragg, and D. M. Neumark, Femtosecond time-resolved photoelectron spectroscopy, *Chemical reviews*, **104**(4), 1719–57, 2004.
- [Sue65] Y. Suemune, Thermal Conductivity of BaTiO₃ and SrTiO₃ from 4.5° to 300°K, *Journal of the Physical Society of Japan*, **20**(1), 174–175, 1965.
- [Tag01] A. Tagantsev, E. Courtens, and L. Arzel, Prediction of a low-temperature ferroelectric instability in antiphase domain boundaries of strontium titanate, *Physical Review B*, **64**(22), 224107, 2001.

-
- [Ter97] J. M. D. Teresa, M. R. Ibarra, P. A. Algarabel, C. Ritter, C. Marquina, J. Blasco, J. García, A. del Moral, Z. Arnold, and J. Garcia, Evidence for magnetic polarons in the magnetoresistive perovskites, *Nature*, **386**(6622), 256–259, 1997.
- [The10] L. Thevenard, E. Peronne, C. Gourdon, C. Testelin, M. Cubukcu, E. Charron, S. Vincent, a. Lemaître, and B. Perrin, Effect of picosecond strain pulses on thin layers of the ferromagnetic semiconductor (Ga,Mn)(As,P), *Physical Review B*, **82**(10), 104422, 2010.
- [Tho86] C. Thomsen, H. T. Grahn, H. J. Maris, and J. Tauc, Surface generation and detection of phonons by picosecond light pulses, *Physical Review B*, **34**(6), 4129–4138, 1986.
- [Tre93] R. Trebino and D. J. Kane, Using phase retrieval to measure the intensity and phase of ultrashort pulses: frequency-resolved optical gating, *JOSA A*, **10**(5), 1101, 1993.
- [Tri07] M. Trigo, T. A. Eckhause, J. K. Wahlstrand, R. Merlin, M. Reason, and R. S. Goldman, Ultrafast optical generation and remote detection of terahertz sound using semiconductor superlattices, *Applied Physics Letters*, **91**(2), 23115, 2007.
- [Tri08] M. Trigo, Y. M. Sheu, D. A. Arms, J. Chen, S. Ghimire, R. S. Goldman, E. Landahl, R. Merlin, E. Peterson, M. Reason, and D. A. Reis, Probing Unfolded Acoustic Phonons with X Rays, *Phys. Rev. Lett.*, **101**(2), 25505, 2008.
- [Tur74] L. Turk and P. Klemens, Phonon scattering by impurity platelet precipitates in diamond, *Physical Review B*, **9**(10), 4422–4428, 1974.
- [Uno67] H. Unoki and T. Sakudo, Electron Spin Resonance of Fe^{3+} in SrTiO_3 with Special Reference to the 110°K Phase Transition, *Journal of the Physical Society of Japan*, **23**(3), 546–552, 1967.
- [vBe01] K. van Benthem, C. Elsässer, and R. H. French, Bulk electronic structure of SrTiO_3 : Experiment and theory, *Journal of Applied Physics*, **90**(12), 6156, 2001.
- [vHi50] A. von Hippel, Ferroelectricity, Domain Structure, and Phase Transitions of Barium Titanate, *Reviews of Modern Physics*, **22**(3), 221—37, 1950.
- [Vis94] K. S. Viswanathan and B. Subramanyam, Elastic anomalies in strontium titanate, *Pramana - journal of physics*, **42**(3), 175–185, 1994.
- [Vre08a] I. Vrejoiu, M. Alexe, D. Hesse, and U. Gösele, Functional Perovskites – From Epitaxial Films to Nanostructured Arrays, *Adv. Funct. Mater.*, **18**(24), 3892–3906, 2008.

- [Vre08b] I. Vrejoiu, M. Ziese, A. Setzer, P. D. Esquinazi, B. I. Birajdar, A. Lotnyk, M. Alexe, and D. Hesse, Interfacial strain effects in epitaxial multiferroic heterostructures of $\text{PbZr}_x\text{Ti}_{1-x}\text{O}_3/\text{La}_{0.7}\text{Sr}_{0.3}\text{MnO}_3$ grown by pulsed-laser deposition, *Appl. Phys. Lett.*, **92**(15), 152506, 2008.
- [Woo61] T. O. Woodruff and H. Ehrenreich, Absorption of sound in insulators, *Physical Review*, **123**(5), 1553, 1961.
- [Yam94] A. Yamamoto, T. Mishina, Y. Masumoto, and M. Nakayama, Coherent Oscillation of Zone-Folded Phonon Modes in GaAs-AlAs Superlattices, *Phys. Rev. Lett.*, **73**(5), 740–743, 1994.
- [Yam02] M. Yamaguchi, T. Yagi, Y. Tsujimi, H. Hasebe, R. Wang, and M. Itoh, Brillouin-scattering study of the broad doublet in isotopically exchanged SrTiO_3 , *Physical Review B*, **65**(17), 172102, 2002.
- [Zei92] H. Zeiger, J. Vidal, T. Cheng, E. Ippen, G. Dresselhaus, and M. Dresselhaus, Theory for dispersive excitation of coherent phonons, *Physical Review B*, **45**(2), 768–778, 1992.
- [Zie12] M. Ziese, F. Bern, E. Pippel, D. Hesse, and I. Vrejoiu, Stabilization of ferromagnetic order in $\text{La}_{0.7}\text{Sr}_{0.3}\text{MnO}_3\text{-SrRuO}_3$ Superlattices, *Nano letters*, **12**(8), 4276–81, 2012.

List of Symbols

α_{us}	ultrasound attenuation	21
α_{th}	linear thermal expansion coefficient	16
B	bulk modulus	16
C_V	heat capacity per unit volume	16
G	reciprocal lattice vector	25
Γ	damping rate of (coherent) ultrasound phonon	21
γ	mode independent Grüneisen parameter	16
d_{SL}	superlattice spatial period	24
η	critical parameter at the ferroelastic phase transition	11
θ	internal photon angle of incidence, angle between photon and coherent phonon	12
θ_{ext}	external photon angle of incidence	15
k	photon wavevector	12
κ	thermal conductivity	22
\bar{l}	average mean free path of thermal phonons	22
λ	vacuum probe wavelength	15
$n(\lambda)$	wavelength dependent refractive index	15
ν_q	phonon frequency	14
ω	photon angular frequency	12
ω_q	phonon angular frequency	12
q	phonon wavevector	12
R_0	static detected intensity reflected of the unpumped sample	29
ΔR	change of the detected intensity reflected from the sample	29
ρ	density	23
t	time	14
dt	time interval of coherent dynamics in the layered sample	17
Δt	dephasing time of observed phonon oscillation	33
T	temperature	23
T_a	ferroelastic phase transition temperature	7
T_C	Curie temperature for ferroelectric and ferromagnetic phase transitions	6
t_G	Goldschmidt tolerance factor	5
t_{SL}	period of superlattice oscillation	26
τ	decay time of ultrasound phonon amplitude	21
$\bar{\tau}$	average decay time of thermal phonons	22
v	longitudinal sound velocity	10

v_{SL}	average sound velocity in a superlattice	24
v_{D}	Debye sound velocity	22

A. Appendix: Normalisation of Measured Phonon Amplitude

A.1 Wavevector Dependence and Proportionality between detected oscillation amplitude and strain

Here we motivate the comparison of the Fourier transformed optical reflectivity measurements with the calculated occupation of phonon modes. According to Thomsen and Grahn the time dependent intensity reflected from a time dependent strain profile in a sample is proportional to the Fourier transform of the strain profile:

$$\Delta R(q, t) \propto q |\mathcal{F}_z(\epsilon(z, t))| \propto q |\mathcal{F}_z\left(\frac{\partial u(z, t)}{\partial z}\right)| \propto q^2 |\mathcal{F}_z(u(z, t))| \propto q^2 u(q, t) \quad , \quad (\text{A.1})$$

where R is the reflected intensity, q is the phonon wavevector and ϵ is the strain, given by the derivative of the atom or unit cell displacement $u(z, t)$ with respect to the phonon propagation direction z , as given in equations (35-38) in [Tho86]. We have applied laws of Fourier transformation and introduced the spectral amplitude of the spatial displacement, i.e. the phonon amplitude: $u(q, t) := |\mathcal{F}_z(u(z, t))|$. For a comparison of the optically detected signal with the calculations in the linear chain model, we write for the elastic energy per mode $E(q, t)$ [Ber05]:

$$E(q, t) = \frac{\omega_q^2 m u(q, t)^2}{2} = \frac{v^2 q^2 m u(q, t)^2}{2} \propto \frac{v^2 q^2 m \Delta R^2}{2q^4} \propto \frac{v^2 m \Delta R^2}{2q^2} \quad , \quad (\text{A.2})$$

where we have inserted the frequency of the elastic oscillation $\omega_q = \sqrt{k_q/m}$ and used the relation $\Delta R(q, t) \propto q^2 u(q, t)$ found above. For the occupation number of the phonon mode, given by $n(q) = E/(\hbar\omega_q)$ we thus deduce

$$n(q, t) \propto \frac{\Delta R(q, t)^2}{q^3} \quad . \quad (\text{A.3})$$

Thus, for a quantitative comparison between the calculated occupation number and the wavevector dependent Fourier transform of the optical reflectivity signal, the obtained data should be squared and weighted with a factor of $1/q^3$.

The proportionality factor in equation A.1 depends on the derivative of the refractive index with respect to strain $dn(\lambda)/d\epsilon$. In a simple approximation, which holds in a bulk material with slowly varying refractive index, this can be assumed to be constant [Boj12a]. However, in a multilayer it may be a complicated function of wavelength and time and thus the wavelength dependent calibration is much more complex.

A.2 Time Dependence of the Phonon Amplitude

Here we derive a normalisation scheme for the time dependent measured oscillation amplitude in order to obtain the correct phonon oscillations amplitude from the data. Following equation 3.1, we evaluate the relative change in reflectivity, given by

$$\frac{\Delta R(t)}{R_0} = \frac{R(t) - R_0}{R_0}, \quad (\text{A.4})$$

where $R(t)$ and R_0 are the time dependent detected intensity of the light reflected from the pumped sample and the static intensity reflected from the unpumped sample, respectively. These are given as

$$R(t) = |r_0 + \Delta r_e(t) + \Delta r_q(t)|^2 E_{\text{in}}^2 \quad (\text{A.5})$$

$$R_0 = |r_0|^2 E_{\text{in}}^2, \quad (\text{A.6})$$

with complex reflection coefficient of the unpumped sample r_0 , dynamic contribution of the electronic system to the reflection $\Delta r_e(t)$, dynamic contribution of the phonon system $\Delta r_q(t)$ and the incoming light field E_{in} . For the expression A.4 we can write

$$\frac{\Delta R(t)}{R_0} = \frac{|r_0 + \Delta r_e(t) + \Delta r_q(t)|^2 E_{\text{in}}^2 - |r_0|^2 E_{\text{in}}^2}{|r_0|^2 E_{\text{in}}^2} \quad (\text{A.7})$$

$$\approx \frac{|r_0 + \Delta r_e(t)|^2 + 2|\Delta r_q(t)||r_0 + \Delta r_e(t)| \cos(\omega_q t) - |r_0|^2}{|r_0|^2}, \quad (\text{A.8})$$

with a periodic constructive and destructive interference between the contribution from the phonons $|\Delta r_q(t)|$ and the contribution from the electrons $|\Delta r_e(t)|$, varying with the phonon frequency ω_q . The approximation holds, because the reflection from the phonon wavepacket is small compared to the other reflections, such that we neglect the term proportional to $|\Delta r_q(t)|^2$. We obtain an oscillating term by highpass filtering

$$\left(\frac{\Delta R(t)}{R_0} \right)_{\text{HP}} = \frac{|\Delta r_q(t)||r_0 + \Delta r_e(t)| \cos(\omega_q t)}{|r_0|^2}, \quad (\text{A.9})$$

and a slowly varying term by lowpass filtering

$$\left(\frac{\Delta R(t)}{R_0} \right)_{\text{LP}} = \frac{|r_0 + \Delta r_e(t)|^2 - |r_0|^2}{|r_0|^2} = \frac{|r_0 + \Delta r_e(t)|^2}{|r_0|^2} - 1. \quad (\text{A.10})$$

For the normalised time dependent phonon amplitude $A_q(t)$ (proportional to $u(q, t)$ from appendix A.1) we thus deduce

$$A_q(t) \propto \frac{|\Delta r_q(t)| \cos(\omega_q t)}{|r_0|} \propto \frac{\left(\frac{\Delta R(t)}{R_0} \right)_{\text{HP}}}{\sqrt{\left(\frac{\Delta R(t)}{R_0} \right)_{\text{LP}} + 1}}. \quad (\text{A.11})$$

List of Publications

- L. Maerten, A. Bojahr, M. Gohlke, M. Rössle, and M. Bargheer, Coupling of GHz-phonons to ferroelastic domain walls in SrTiO₃, *Phys. Rev. Lett.*, accepted, 2015.
- L. Maerten, A. Bojahr, and M. Bargheer, Observing backfolded and unfolded acoustic phonons by broadband optical light scattering., *Ultrasonics*, **56**, 148–152, 2015.
- A. Bojahr, M. Herzog, S. Mitzscherling, L. Maerten, D. Schick, J. Goldshteyn, W. Leitenberger, R. Shayduk, P. Gaal, and M. Bargheer, Brillouin scattering of visible and hard X-ray photons from optically synthesized phonon wavepackets, *Opt. Express*, **21**(18), 21188–21197, 2013.
- A. Bojahr, D. Schick, L. Maerten, M. Herzog, I. Vrejoiu, C. von Korff Schmising, C. J. Milne, S. L. Johnson, and M. Bargheer, Comparing the oscillation phase in optical pump-probe spectra to ultrafast x-ray diffraction in the metal-dielectric SrRuO₃/SrTiO₃ superlattice, *Physical Review B*, **85**(22), 224302, 2012.

Danksagung

Meinen herzlichen Dank an alle, die zum Entstehen dieser Arbeit beigetragen haben.

Insbesondere an Matias für die freundliche Aufnahme in die Arbeitsgruppe, die stete Bereitschaft, Ergebnisse und physikalische Prozesse zu diskutieren, für viel Freiheit und seinen unerschütterlichen Enthusiasmus. Marc und André, für die Unterstützung bei alltäglichen Fragen im Labor, zur Datenanalyse und physikalischen Interpretationen. Diskussionen mit euch waren immer sehr lehrreich und motivierend! Matthias Rössle, im letzten Jahr ein angenehmer Bürokollege, diskussionsfreudiger STO-Experte, eifriger Korrekturleser und verlässlicher, engagierter Begleiter in der Abschlussphase. Clemens, der in der "magnetischen Phase" ein wertvoller Gesprächspartner und Bürokollege war. Flavio, für sorgfältiges Korrekturlesen und viele hilfreiche, kritische Kommentare zum Manuskript. Daniel, für wertvolle Unterstützung in Sachen Software und Programmierung. Lisa und Viktor, die einige der gezeigten Messungen durchgeführt und ausgewertet haben. Allen anderen derzeitigen und ehemaligen Mitgliedern der Arbeitsgruppe vielen Dank für die nette Zusammenarbeit und die gute Stimmung in unserer Arbeitsgruppe!

Darüber hinaus gilt mein Dank meinen Eltern, die mich bei dieser Arbeit stets unterstützt haben und zusammen mit meinen Schwiegereltern, Christian und Anna bei der Babybetreuung wertvolle Hilfe geleistet haben. Jakob, der mich jeden Abgabestress schnell vergessen lassen hat und der kleine Motivator war, die Arbeit so strukturiert und effizient zum Abschluss zu bringen. Carlus für Unterstützung in jeglicher Hinsicht, insbesondere für die selbstverständliche Übernahme aller Familienaufgaben in den letzten Wochen.